Time-of-flight 3D Neutron Diffraction for Multigrain Crystallography

Cereser, Alberto

Publication date:
2016

Document Version
Publisher's PDF, also known as Version of record

Time-of-flight 3D Neutron Diffraction for Multigrain Crystallography

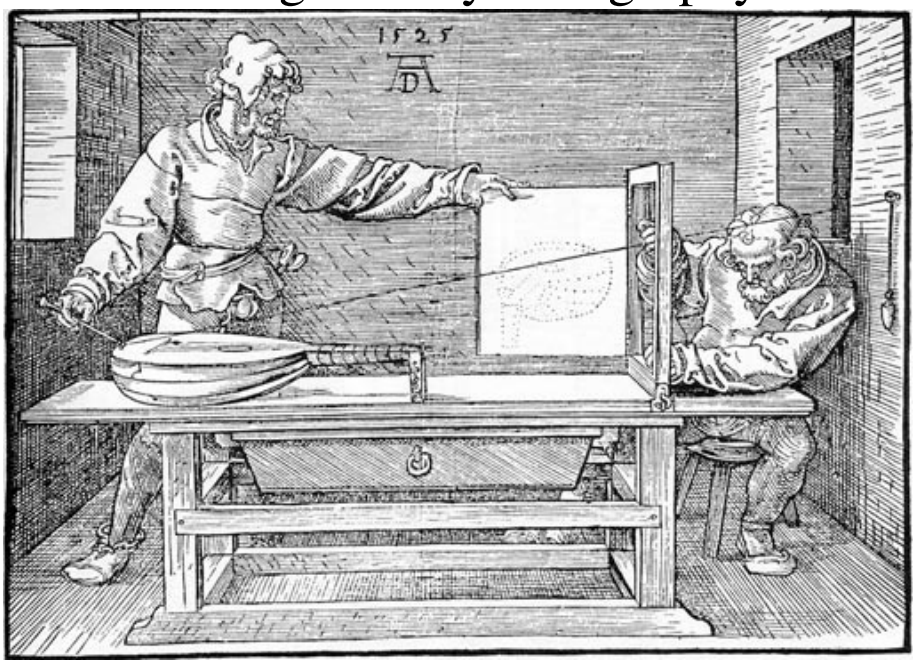

Alberto Cereser

June 6, 2016

Cover image. Man drawing a lute, by Albrecht Dürer (1525). In this drawing, Dürer illustrates a technique to draw prospective using ray-tracing. *"Place a lute or another object to your liking as far from the frame as you wish, but so that it will not move while you are using it. Have your assistant then move the pointer..."* [Dürer, 1977]. In this thesis work, a more efficient ray-tracing technique was used [Lefmann and Nielsen, 1999].

Abstract

This thesis presents a new technique for measuring spatially resolved microstructures in crystalline materials using pulsed neutron beams. The method, called Time-of-Flight Three Dimensional Neutron Diffraction (ToF 3DND), identifies the position, shape and crystallographic orientation of the individual grains within the sample. The experiments were conducted at the single crystal diffractometer SENJU at the Japanese neutron source J-PARC. The choice of this instrument was motivated by its large coverage of the reciprocal space.

The instrument had to undergo modifications to enable ToF 3DND measurements: a time resolved imaging detector, developed at University of Berkeley, California, was fitted in the interior of SENJU in order to record the extinction spots in the transmitted beam (i.e. areas with missing intensity due to Bragg diffraction of the individual grains).

The arrangement of the two detector systems facilitated two versions of ToF 3DND. The first version, restricted to imaging data, enables reconstruction of the position and shape of the individual grains without the use of crystallography. Afterwards, the orientations of the individual grains are indexed. The algorithms for both steps have been developed in this study. The work also shows that based on the transmission data alone the orientations are not uniquely determined; however, it is possible to find an unique solution by including diffraction signals from the imaging detector. The second version uses an existing method for indexing SENJU data, which then serves as prior information to restrict the extinction spots that belong to the same grain.

The ToF 3DND methods are verified through the study of two different samples: an Iron rod and a shape memory alloy (SMA) CoNiGa bi-crystal. Part of this verification involves comparison with electron backscatter diffraction (EBSD). In the Iron rod, 107 grains were indexed from the SENJU data. As a comparison, 108 grains were reconstructed from the nearfield data alone. This constitutes roughly 10 times as many grains as previously reported using a continuous neutron source.

Thanks to the penetrating properties of the neutron, ToF 3DND comple-

ments existing X-ray techniques in those cases where X-rays cannot penetrate the sample. Besides, with ToF 3DND it is also much easier to detect light elements such as those in energy materials.

With a future availability of an energy dispersive x-ray detector with high energy resolution, the methods reported here can be directly transferred to synchrotron and white beam based studies.

Resumé

I denne afhandling præsenteres en ny målemetode, der vha. pulserede neutron kilder muliggør studiet af den rummelige materialestruktur i krystallinske materialer. Metoden, som kaldes Time-of-Flight Three Dimensional Neutron Diffraction (ToF 3DND), identificerer positionen, formen og den krystallografiske orientering af de individuelle korn i prøven. Målingerne er udført pået krystaldiffraktometer kaldet SENJU ved den japanske neutronkilde J-PARC. Valget af SENJU er motiveret af instrumentets høje dækning af reciprokt rum.

For at udføre målingerne skulle instrumentet ombygges. Specielt blev en tidsopløst imaging detektor, udviklet på University of Berkeley, California, monteret således, at ekstinktion-pletter (områder med manglende intensitet i det transmitterede signal pga. Bragg diffraktion fra individuelle korn) kunne observeres.

Kombinationen af de to detektorsystemer har ledt til etablering af to versioner af ToF 3DND. Den første version benytter udelukkende imaging detektoren. Først rekonstrueres kornenes form uden brug af information om materialets krystallografiske klasse. Derefter indekseres de enkelte kornorienteringer. Begge trin bygger pånye algoritmer, som er udviklet i dette studie. Afhandlingen viser desuden, at transmissionssignalet isoleret set ikke er nok til en entydig bestemmelse af kornorienteringer. Dog kan en entydig bestemmelse opnås ved at inkludere diffraktionssignalet påimaging detektoren i analysen. Den anden version benytter først en eksisterende metode til indeksering af kornorienteringen i SENJU data, som dermed afgrænser hvilke ekstinktion-pletter, der hører til samme korn.

I afhandlingen bliver der målt påto typer materialer; en Jernprøve og en CoNiGa - shape memory alloy (SMA) bi-krystal. Gennem studiet af begge prøver verificeres ToF 3DND metoderne, herunder sammenlignes med EBSD. I jernprøven indekseres 107 korn. Til sammenligning findes 108 korn baseret udelukkende påimaging data. Dette er ca. 10 gange flere korn end tidligere rapporteret fra en kontinuerlig neutronkilde.

Grundet neutronens komplementære spredningsegenskaber, set i forhold til

fotonen, vil ToF 3DND med fordel kunne benyttes ved studiet af en række materialeklasser, der enten ikke kan gennemtrænges af røntgen eller hvor lette atomer, i f.eks. energimaterialer, er betydeligt nemmere at detektere.

Metoderne, som er udviklet i denne afhandling kan, med en fremtidig energifølsom røntgendetektor med høj energiopløsning, direkte kunne overføres til synkrotronmålinger foretaget med hvidt beam.

Acknowledgment

The work presented in this thesis was conducted at the Neutrons and X-rays for Materials Physics (NEXMAP) group of the Department of Physics at the Technical University of Denmark under the supervision of Søren Schmidt. The external supervisors were Axel Steuwer, Markus Strobl and Stephen Hall. The project was partially supported by the European Spallation Source (ESS). I would like to acknowledge the Danish Agency for Science and Technology (through Danscatt) for covering expenses in relation to experiments at neutron facilities.

I would first like to thank my supervisors for the opportunity to work on this project, for their guidance and for the support. In particular I would like to thank Søren for treating my math ignorance, for writing zillions of rotation matrices at the whiteboard and for sharing the algorithms development rollercoaster. It's been a ride. Thanks to Markus for his help at the beamline(s) and for all the feedback, to Steve for the careful editing and for Axel for the suggestions on how to get samples with large grains.

I would also like to thank all my colleagues and collaborators for making ToF 3DND possible. Starting from the sample preparation, thanks to Lars Lorentzen, Malte Vollmer and Philipp Krooß, Srinivasan Iyengar, Wolfang Pantleon and Yury Chumlyakov. Simulations were made possible by the help of the McStas gurus, Erik Knudsen (Erik, thanks also for the help with the network interface at SENJU!) and Peter Willendrup. For their help during the experiments, thanks to Joe Kelleher, Peter Mahler Larsen, Saurabh Kabra, Steven Peetermans and Winfried Kockelmann.

A special mention goes to the SENJU team, that made possible performing the first ToF 3DND experiments: thanks to Hanashima Takayasu, Ichiro Tanaka, Ryoji Kiyanagi, Taketo Moyoshi and the rest of the personnel. Thanks also to Takenao Shinohara. For his worldwide, 24/7 assistance with everythign concerning the MCP detector, thanks to Anton Tremsin. For the EBSD scans thanks to Alice Bastos da Silva Fanta, Steffen Munch and Philipp Krooß.

In Spring 2015, I spent a month at BL18 as a beamline guest. Thanks again to Ryoji and the rest of the team for the great time in Tokai-mura!

Thanks to Marta, my officemate of these 3+ years, for all the support, for introducing me to the Toronto Maple Leafs and for making the office a better place.

They say it takes a village to raise a Ph.D. Thanks to all the NEXMAP members for the interesting discussion, especially Andres, Elisa, Henning, Hugh, Jette, Niels, Miriam and Yun. For their help, thanks to Jane, Marianne and Ole.

To my friends and family: thanks for your support and for reminding me there is life away from the screen.

This thesis is dedicated to Martina, my girlfriend and best friend.

Contents

ACRONYMS

3DND Three-dimensional neutron diffraction

3DXRD Three-dimensional X-ray diffraction

DCT X-ray diffraction contrast tomography

EBSD Electron backscatter diffraction

ESS European Spallation Source. Pulsed neutron source, under construction (Sweden)

HEDM High energy X-ray diffraction

ISIS ISIS neutron source. Pulsed neutron source (UK)

J-PARC Japan Proton Accelerator Research Complex

LabDCT Diffraction contrast tomography for laboratory X-ray sources

MCP Micro-channel plate, type of detector

MLF The Materials and Life Science Experimental Facility of J-PARC. Hosts a pulsed neutron source

nDCT Neutron diffraction contrast tomography

PSI Paul Scherrer Institute (Switzerland)

SNS Spallation Neutron Source. Pulsed neutron source (US)

ToF Time-of-fligh

1

Introduction

Contents

HARD polycrystalline materials are solids composed of crystallites (also referred to as *grains*) of different size and with different crystallographic properties. Polycrystalline materials play a fundamental role in materials science and engineering; solids with a polycrystalline structure include metals, alloys, many ceramics, rocks, bones and ice.

The physical, chemical and mechanical properties of polycrystalline materials depend on their structure, which in turn is defined by how the internal components are arranged over different length scales, ranging from Ångstroms to decimetres [Poulsen, 2004, Clemens et al., 2008]. At present, there is no unique model that can describe how grains interact at the different length scales.

In the understanding of the structure of a polycrystalline material, it is very important to be able to characterise the 3D grain structure and crystallographic propeties. Among the crystallographic properties, of particular interest is the orientation, which can be intuitively defined as "how the atomic planes in a volume of crystal are positioned relative to a fixed reference" [Randle and Engler, 2000]. Knowing the shape of the grains, their arrangement and their orientation provides information on which grains are likely to interact and how [Randle and Engler, 2000].

In the last two decades a number of techniques emerged to study, nondestructively and in 3D, the shape and orientation of the grains composing polycrystalline materials at different scales. Compared with destructive techniques

such as three-dimensional electron backscatter diffraction (3D EBSD), where the sample is serially sectioned and imaged [Zaefferer et al., 2008], nondestructive solutions have the following characteristics:

- They require less sample preparation, thus limiting the introduction of new structures in the sample
- They can be used to investigate larger samples and to employ more complicated sample environments
- They enable to study how 3D grain structures evolve under different conditions
- Since the measurements does not alter the sample, different types of analysis can be made in sequence.

1.1 EXISTING TECHNIQUES

Examples of non-destructive techniques developed to obtain grain maps include three-dimensional orientation mapping in the transmission electron microscope (3D-OMiTEM), using electrons to map samples with a nanometer-size resolution; X-ray diffraction contrast tomography (DCT), high energy X-ray diffraction (HEDM) and three-dimensional X-ray diffraction (3DXRD), allowing investigation of micrometre- to millimetre-sized samples with resolution ranging from hundreds of nanometers to micrometers [Liu et al., 2011, Poulsen et al., 2001, Ludwig et al., 2008, Suter et al., 2006]. More recently, software returning three-dimensional grain maps for laboratory sources became commercially available [xno, 2016]. At the continuous neutron source of the Paul Sherrer Institute (PSI), neutron diffraction contrast tomography (nDCT) was recently used to study millimetre-sized samples [Peetermans et al., 2014]. The sample was illuminated by a continuous, polychromatic neutron beam and the diffracted signal was collected in backscattering Laue mode.

This thesis presents a new neutron technique, time-of-flight three-dimensional neutron diffraction (ToF 3DND), which uses time-of-flight neutrons to reconstruct the 3D shape, orientation and juxtaposition of the individual grains composing polycrystalline materials.

Whereas, for hard X-rays, diffraction is mostly confined in the forward direction with respect to the incoming beam, for thermal neutrons diffraction is

more isotropic in nature[1]. Consequently, the detector coverage required for grain mapping using X-rays is much less than that required when using neutrons. Time-of-flight neutron beams (as opposed to white beam or to beam emitted by a continuous spallation source) enable the use of time-resolved transmission imaging detectors, which record regions of missing intensity (*extinction spots*) each time a grain satisfies the diffraction condition. This happens at determinate wavelengths, depending on the crystallographic orientation of the grain. With this approach, in principle the shape of all diffraction spots can be observed indirectly using only detector coverage comparable to the size of the sample in question.

In contrast, in the ToF neutron community, large detector coverage for obtaining reciprocal space information is available. The aim of this thesis work has been to investigate - for the first time - the feasibility of using the transmitted and diffracted neutron ToF signals, both apart and combined, for characterization of polycrystalline materials.

Developing ToF 3DND required

- A *new hardware setup*, able to simultanously collect transmission and diffraction data. This was realised at beamline BL18 ("SENJU") at MLF, J-PARC (Japan) by collecting diffraction data using the single crystal diffractometer of the beamline, and transmission data using an imaging detector with high temporal and spatial resolution.

- *New software*, to reconstruct the shape of the grains from the extinction spots collected in transmission mode. The idea was first introduced by X-ray diffraction contrast tomography (DCT), where a monochromatic beam was used [Ludwig et al., 2008]. In this work, ad-hoc computer vision solutions were developed to isolate the extinction spots in the images collected in transmission mode.

- *New software*, to enable indexing of grains from the distribution of the relative extinction spots in the transmitted beam as a function of the wavelength and the rotation angle where they are recorded. To index grains from the transmission data, existing software was adapted.

- *New software*, to *a)* simulate transmission and diffraction from a polycrystalline sample illuminated by a time-of-flight neutron beam and *b)* compare the results with the data collected at J-PARC. Before this project,

[1] Diffraction depends on the form factor, whose value falls for large angles. For neutrons, the form factor is independent on the angle

the only way to simulate a polycrystal was to combine several single crystals, ignoring scattering between the crystallites.

- *Verification*. Comparison with electron microscopy was used to validate both the shape reconstruction procedure and the new indexing one, that calculates the orientation of the grains from the transmission data. Moreover, consistency between the new indexing procedure and the one normally used for X-rays was checked.

1.2 NEUTRON IMAGING

3DND adds to the various *neutron imaging* techniques recently introduced and now under development, such as Bragg-edge tomography, returning information on the distribution of phases, and 3D imaging of magnetic domains [Woracek et al., 2015, Strobl et al., 2008]. For a review of the state-of-the-art in neutron imaging, see the works [Strobl et al., 2009, Kardjilov et al., 2011].

3DND introduces a new way to obtain 3D grain maps using ToF neutrons. The technique complements attenuation-based tomography, widely used in neutron imaging to map the distribution of the attenuation coefficient μ within a sample. Considering a given beam with intensity I_0 illuminating a sample with thickness L, the intensity I collected by a detector mounted in transmission mode is given by the Beer-Lamber law:

$$I = I_0 e^{-\int \mu(z) dz} \tag{1.1}$$

In comparison, 3DND maps differences in crystal properties (primarily orientation), providing contrast in samples that might appear relatively homogeneous in attenuation reconstructions. Plus, 3DND provides additional, new information on the underlying inter-grain structure.

1.3 THESIS OUTLINE

After introducing the main concepts of neutron crystallography in Ch. 2, in Ch. 3 the thesis outlines the different neutron production techniques and describes the setup used at the Japan Proton Accelerator Research Complex (J-PARC) to collect data. As stated previously, this was done using two types of detector, respectively collecting transmitted and diffracted data. Ch. 4 presents the two methodologies we developed to reconstruct the shape and orientation of the grains using the transmission data only (methodology I) or combining the

transmission and the diffraction data (methodology II). In Ch. 5, we describe the simulations run before the "real" experiments, together with the new solution developed to simulate diffraction from polycrystalline samples. Ch. 6 and 7 explain the algorithms developed to reconstruct the shape and orientation of the grains. In Ch. 8 we evaluate the results of the project, draw conclusions and suggest future research directions.

2

Neutron crystallography

Contents

THE aim of 3DND is to investigate the structure of polycrystalline materials using neutrons. This chapter introduces the main properties of the neutron and of crystals, and describes how neutrons are scattered by atomic nuclei and by crystalline structures. The chapter concludes with an introduction to crystallographic orientations (Sec. 2.3).

2.1 THE NEUTRON

The existence of the neutron, postulated by Rutherford in 1920, was proven by James Chadwick in 1932. Three years later Chadwick was awarded the Nobel prize for his discovery. The neutron, consisting of three quarks, is a particle with no electrical charge, spin $\frac{1}{2}$ and mass of $1.675{\cdot}10^{-27}$ kg. These properties define the behaviour of the neutron: since it is uncharged, it interacts mainly with the nuclei and thus can penetrate deeply into samples. A typical neutron used for scattering or imaging experiments has wavelength of the order of interatomic distances and energy similar to elementary excitations in solids. It can

Parameter	Value
Charge	$0 \times e$
Magnetic moment	$1.913 \times \mu_n$
Mean lifetime	881.5 s
Rest mass	930.6 MeV/c^2
Spin	$\frac{1}{2} \times \hbar$

Table 2.1: Basic properties of the neutron.

thus return information on how structures are arranged and how particles move within them. Thanks to its spin, the neutron is sensitive to external magnetic fields. The motion of the quarks give the neutron a magnetic momentum that can interact with the magnetic moments of unpaired electrons. This happens, for example, with transition elements [Giacovazzo et al., 1998].

Since incoming neutrons interact with the nucleus via the weak nuclear force, they are only sensitive to the internal structure of the nuclei, and not to the mass or total electric charge of the atom. Hence, the neutron has similar cross sections for light and heavy atoms. This makes neutrons the probe of choice over X-rays when it comes to investigating samples containing light elements like hydrogen, carbon or oxygen, even when they are together with heavy ones [Voigt, 2012].

2.1.1 SCATTERING FROM A NUCLEI

A neutron can be scattered in two different ways: *a)* it interacts with the atomic nucleus (*nuclear scattering*) or *b)* its magnetic moment interacts with the magnetic moment of the target atom, which is due to an unpaired electron configuration (*magnetic scattering*). The nuclear scattering case is presented below (no magnetic scattering was involved in the current development of 3DND). The presentation is based on the works [Herwif, 2009, Von Dreele, 1990, Pynn, 2009]. Section 2.1.1 is based on [Pynn, 2009, Jackson, A. J., 2008]

Let us assume a beam of neutrons impinges on a single nucleus, located at the origin, and is elastically scattered by it. The interaction between the neutrons and the nucleus is regulated by the interation potential $V(\mathbf{r})$, which rapidly falls to 0 for a distance $\mathbf{r}$ of the order of 10^{-15} m. The typical neutron wavelength is much longer: 1 $\AA$, 10^{-10} m. As a consequence, the neutron scatters isotropically and can be considered as a point scatterer.

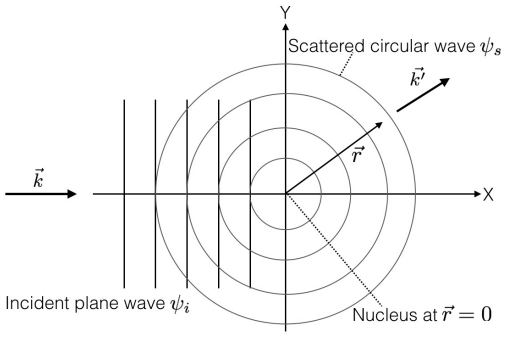

Figure 2.1: Elastic neutron scattering from a nucleus fixed in the origin.

The incident beam of neutrons can be described by the plane wavefunction

$$\psi_i = e^{ikz} \tag{2.1}$$

where z is the distance from the nucleus in the propagation direction and $k = 2\pi/\lambda$ is the wavenumber. As shown in Fig. 2.1, the scattered wave has spherical symmetry and wavefunction

$$\psi_s = -\frac{b}{r}e^{ik'z} \tag{2.2}$$

with $k \neq k'$ and b being the neutron scattering length, measuring the strength of the neutron-nucleus interaction. The scattering length of nuclei varies randomly across the periodic table, as well as among isotopes of the same element. As an example, the two isotopes hydrogen and deuterium (^{1}H and ^{2}H) have scattering length $b_{1H} = -3.79 \cdot 10^{-5}\mathring{A}$ and $b_{2H} = 6.67 \cdot 10^{-5}\mathring{A}$, respectively.

As usual in collisions, when a neutron beam is scattered by a nucleus the total energy and momentum are conserved. The momentum given up by a neutron in a collision is

$$\frac{h\mathbf{Q}}{2\pi} = \frac{h(\mathbf{k}-\mathbf{k}')}{2\pi} = \hbar(\mathbf{k}-\mathbf{k}') \tag{2.3}$$

where $\mathbf{Q} = \mathbf{k} - \mathbf{k}'$ is known as scattering vector, and the relation between $\mathbf{Q}$, $\mathbf{k}$ and $\mathbf{k}'$ (the so-called scattering triangle) is illustrated in Figure 2.2.

For an arbitrary sample illuminated by a neutron beam, the incoming flux Ψ is defined as

$$\Psi[n/(cm^2 \cdot s)] = \frac{\text{Number neutrons impinging on the surface per second}}{\text{Surface area perpendicular to the incident beam}} \tag{2.4}$$

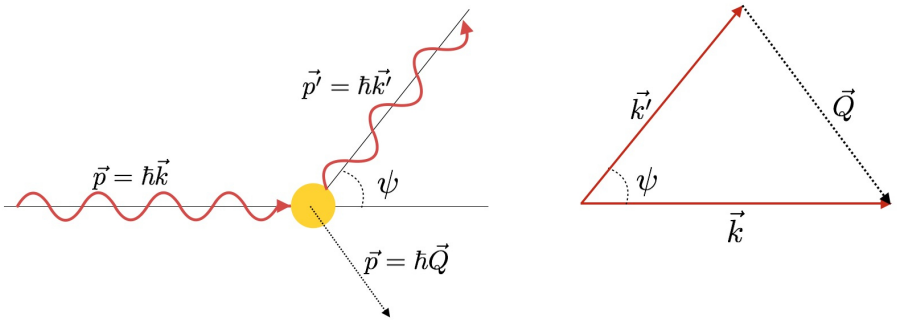

Figure 2.2: *Left:* scattering of a neutron with momentum $\vec{p} = \hbar\vec{k}$ by a nucleus. The scattered neutron has momentum $\vec{p'} = \hbar\vec{k'}$, and the momentum transferred to the nucleus is $\vec{Q} = \vec{k} - \vec{k'}$. *Right:* scattering triangle showing the relations between the wavevectors $\vec{Q}$, $\vec{k}$ and $\vec{k'}$.

The ability of a sample to scatter neutrons is given by the neutron scattering cross section σ, with area units:

$$\sigma = \frac{1}{\Psi} \cdot \text{Number of neutrons scattered per second} \tag{2.5}$$

In a neutron scattering experiment, it is crucial to measure the number of scattered neutrons as a function of the scattering angle. This distribution is described by the differential cross section

$$\frac{d\sigma}{d\Omega} = \frac{1}{\Psi} \cdot \frac{\text{Number of neutrons per second scattered in} d\Omega}{d\Omega} \tag{2.6}$$

where $d\Omega$ is the angular span of the detector.

The maximum flux provided by neutron facilities is of the order of 10^6 neutrons per second per squared millimetre, 12 orders of magnitude less than the flux from X-ray sources [Center, 2015, Pynn, 2009]. Combined with the weak nature of the sample-neutron interaction, low flux makes neutron scattering a signal-limited technique, to be used only when others fail. Neutron instruments are designed to make the best use of the limited flux.

2.2 CRYSTALLOGRAPHY

Crystallography, from the Greek *krustallos* ("ice") and *graphein* ("to write"), is the science studying the arrangement of atoms in crystalline structures and the properties of these [International Union of Crystallography, 2016]. This Section

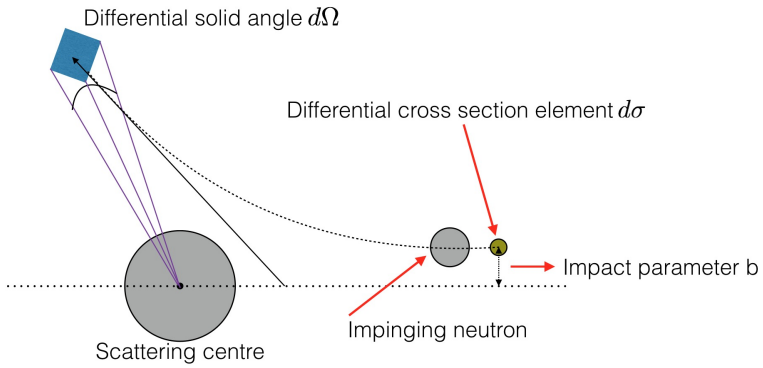

Figure 2.3: Schematic diagram of the scattering of an incident neutron by a nucleus. The impact parameter b, the differential cross section element $d\sigma$ and the solid angle element $d\Omega$ in the exit direction are marked. $d\sigma/d\Omega$ is the differential cross section.

presents the basics of crystallography, following [Als-Nielsen and McMorrow, 2011, Ashcroft and Mermin, 1976, Willis and Carlile, 2009].

2.2.1 CRYSTALLINE STRUCTURES AND THE RECIPROCAL LATTICE

In the description of crystalline solids, a fundamental concept is that of a *Bravais lattice*, which describes how the units of the crystal are periodically arranged. The Bravais lattice is a purely geometrical description, which does not depend on the nature of the crystal units, that can be single atoms, atoms or group of atoms. In 3D, a Bravais lattice consists of all points defined by the position vector $\mathbf{R}$, defined as

$$\mathbf{R} = n_1\mathbf{a_1} + n_2\mathbf{a_2} + n_3\mathbf{a_3} \tag{2.7}$$

where $\{n_i\}_{i=1,2,3} \in \mathbb{Z}$ and $\{\mathbf{a_i}\}_{i=1,2,3}$ are the *primitive vectors* that generate the lattice.

The *unit cell* is the volume that, translated through selected vectors $\mathbf{R}$ of the Bravais lattice, fills the space without any overlapping. A physical crystal can be described as a Bravais lattice that at each point has identical copies of the same arrangements of particles, known as *basis*, contained in the unit cell.

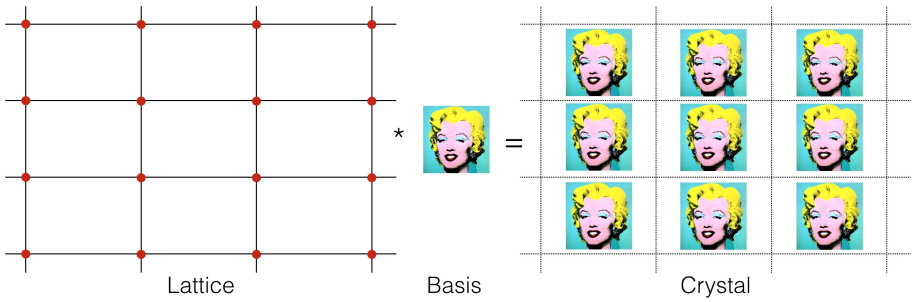

Figure 2.4: A crystal can be described as a ordered set of points (the lattice), each centre of a given arrangement of particles (the basis). The operation denoted with $\star$ is convolution. Artwork by [Warhol, 1962].

2.2.1.1 The reciprocal lattice

The Fourier transform of the crystal lattice is the *reciprocal lattice*, with translational vectors $(\mathbf{a}_1^*, \mathbf{a}_2^*, \mathbf{a}_3^*)$ defined by the equations

$$\mathbf{a}_1^* = 2\pi \cdot \frac{\mathbf{a}_2 \times \mathbf{a}_3}{\mathbf{a}_1 \cdot (\mathbf{a}_2 \mathbf{a}_3)}, \; \mathbf{a}_2^* = 2\pi \cdot \frac{\mathbf{a}_3 \times \mathbf{a}_1}{\mathbf{a}_1 \cdot (\mathbf{a}_2 \mathbf{a}_3)}, \; \mathbf{a}_3^* = 2\pi \cdot \frac{\mathbf{a}_1 \times \mathbf{a}_2}{\mathbf{a}_1 \cdot (\mathbf{a}_2 \mathbf{a}_3)} \tag{2.8}$$

The points of the reciprocal lattice are located by $\mathbf{G}$, defined as

$$\mathbf{G} = h\mathbf{a}_1^* + k\mathbf{a}_2^* + l\mathbf{a}_3^* \tag{2.9}$$

where h, k and l are the *Miller indices*, with $(h,k,l) \in \mathbb{Z}$. For a set of Miller indices, the corresponding *lattice spacing* d_{hkl} is defined as the distance between the lattice planes perpendicular to $\mathbf{G}$:

$$d_{hkl} = \frac{2\pi}{|\mathbf{G}|} \tag{2.10}$$

2.2.2 Scattering from a crystal

Let us consider a crystalline structure illuminated by a neutron beam with wavevector $\mathbf{k}$ and wavelength $\lambda = 2\pi/|\mathbf{k}|$. The crystal can be considered to be made out of parallel planes of particles, spaced by a distance $d = d_{hkl}$, which corresponds to a given hkl set. When the neutrons scattered from successive planes interfere constructively, sharp peaks (known as *Bragg peaks*) of scattered radiation are observed. As shown in Fig. 2.5, the path difference for two neutrons scattered by successive planes is $2d_{hkl}\sin\theta$, with θ being the incident angle. The condition for neutron waves to interfere constructively, resulting in Bragg peaks, is

that the path difference is equal to an integral number of wavelengths, as described by *Bragg's law*:

$$\boxed{n\lambda = 2d_{hkl}\sin\theta} \tag{2.11}$$

where n is a positive integer.

In reciprocal space, the diffraction condition is given by the three *Laue equations*:

$$\mathbf{Q}\cdot\mathbf{a}_1^* = h\lambda \tag{2.12}$$
$$\mathbf{Q}\cdot\mathbf{a}_2^* = k\lambda \tag{2.13}$$
$$\mathbf{Q}\cdot\mathbf{a}_3^* = l\lambda \tag{2.14}$$

It can be shown that Bragg's law and the Laue equation are equivalent formulations, and thus

$$\boxed{\mathbf{G} = \mathbf{Q} = \mathbf{k} - \mathbf{k}'} \tag{2.15}$$

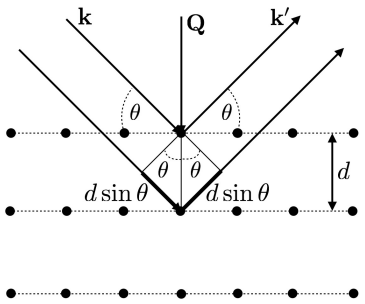

Figure 2.5: Diffraction in Bragg geometry. $\mathbf{k}$ and $\mathbf{k}'$ are the incoming and outgoing wavevectors, with identical incident angle θ, $\mathbf{Q}$ is the scattering vector and d is the distance between the lattive planes perpendicular to $\mathbf{Q}$.

2.2.2.1 The structure factor

For a crystalline structure illuminated by neutrons, the scattering amplitude or *structure factor*, F, can be calculated as a sum of the scattering from all the atoms involved:

$$F(\mathbf{Q}) = \sum_{R_n, r_j} f_j^{atom}(\mathbf{Q}) e^{i\mathbf{Q}\cdot(\mathbf{r_j}+\mathbf{R_n})} \tag{2.16}$$

$$= \overbrace{\sum_{r_j} f_j^{atom}(\mathbf{Q}) e^{i\mathbf{Q}\cdot\mathbf{r_j}}}^{\text{unit cell structure factor}} \cdot \overbrace{\sum_{R_n} f_j^{atom}(\mathbf{Q}) e^{i\mathbf{Q}\cdot\mathbf{R_n}}}^{\text{lattice sum}} \tag{2.17}$$

$$= \overbrace{\sum_{r_j} f_j^{atom}(\mathbf{Q}) e^{i\mathbf{Q}\cdot\mathbf{r_j}}}^{\text{unit cell structure factor}} \cdot S_N(\mathbf{Q}) \tag{2.18}$$

where the position of the atoms is defined by $\mathbf{r_j} + \mathbf{R_n}$, sum of a lattice and a basis vector.

As shown in Eq. 2.18, the structure factor is the product of the unit cell structure factor and of the lattice sum, $S_N(\mathbf{Q})$, calculated considering all the $N = N_1 \cdot N_2 \cdot N_3$ scattering atoms illuminated by the beam in the X, Y and Z direction. To show the relationship between the intensity of a diffraction spot, or the corresponding missing intensity of an extinction spot, and the structure factor F, let us consider a crystal illuminated by a time-of-flight neutron beam, resulting in a diffraction spot for wavelengths between λ_1 and λ_2. In that wavelength interval, the integrated intensity of the diffraction spot is [Buras and Gerward, 1975]

$$I = i_0(\lambda) V N^2 |F|^2 \lambda^4 \frac{1}{2\sin^2\theta} \tag{2.19}$$

where $i_0(\lambda)$ [n/cm^2/Å] is the spectrum of the incident beam, V is the volume of the illuminated crystal, N is the number of crystal unit cells per unit volume, λ is the incident wavelength ($\lambda \in [\lambda_1, \lambda_2]$) and θ is the Bragg angle.

Using Braggs's law and denoting the detector efficiency with $e(\lambda)$, Eq. 2.19 can be rewritten as

$$I = i_0(\lambda) e(\lambda) V N^2 |F|^2 2\lambda^2 d^2 \tag{2.20}$$

When a neutron beam illuminates a crystalline structure, the diffracted beam is attenuated as a result of thermal motion. The process is described by the Debye-Waller factor (DWF), defined as [Kittel, 2005, Attfield et al., 2016]

$$DWF = \exp\left(-B(T)\frac{\sin^2\theta}{\lambda^2}\right) = \exp\left(\frac{-B(T)}{4d^2}\right) \tag{2.21}$$

where T is the temperature, θ is the Bragg angle and λ is the incident wavelength. For iron, at room temperature the value of B is $\sim$0.35 $Å^2$ [Mohanlal, 1979]. For a diffraction spot, the integrated intensity is thus

$$\boxed{I = i_0(\lambda)e(\lambda)VN^2|F|^2 2\lambda^2 d^2 e^{\frac{-B(T)}{4d^2}}} \tag{2.22}$$

2.3 CRYSTALLOGRAPHIC ORIENTATIONS

The *crystallographic orientation*, or simply orientation, of a grain is the rotation U that brings the coordinate system of the grain into the coordinate system of the sample [Randle and Engler, 2000, Lauridsen, 2001]:

$$C_s = UC_g \tag{2.23}$$

where C_g is the reference system of the grain and C_s is the reference system of the sample. The procedure of calculating the orientation of a grain is commonly referred to as *indexing*. In Ch. 7, we will study an ensemble of grains, each with its own orientation (see Eq. 7.4).

Rodrigues vectors are elements of the *Rodrigues space*, introduced to the materials science community[1] by [Frank, 1988]. In the Rodrigues space, $\mathbf{r}$ is a three-dimensional vector

$$\mathbf{r} = \tan(\varphi/2)\mathbf{n} \tag{2.24}$$

where $\mathbf{n}$ is the rotation axis and φ the rotation angle around it [Morawiec and Field, 1996].

Compared to other representations, describing orientations using Rodrigues vectors offers the following advantages:

1. They are intuitively defined;
2. Using them, calculations are simpler than with most other representations;
3. They can be represented as vectors in the sample coordinate system.

[1] The original idea is by Olinde Rodrigues (1795-1851), a French banker and mathematician.

3

Experimental setups and data acquisition

Contents

THE 3DND reconstruction algorithms were developed analyzing datasets collected at the single crystal diffractometer SENJU, installed at beamline BL18 of the Material and Life Science Experimental Facility (MLF) at J-PARC in Japan. Test experiments were also performed at ISIS in the UK (beamline ENGIN-X) and at PSI in Switzerland (beamline ICON). Compared to the other considered instruments, SENJU offers a greater detector coverage and benefits from the higher flux of J-PARC, which results in a higher signal-to-noise ratio in the transmission data.

The first part of this chapter (Sec. 3.1) briefly presents how neutrons are produced for scattering and imaging experiments. The overview is followed by an introduction to J-PARC (Sec. 3.2) and SENJU (Sec. 3.3).

3.1 NEUTRON SOURCES

Two kinds of sources are used to produce neutrons for neutron scattering and high-resolution imaging experiments: reactors and spallation sources. Both produce neutrons with energy in the MeV range, which need to be slowed down before being used in scattering or imaging experiments, which require neutron energies in the meV range. The slowing down process takes place in the moderator, that will be presented in Sec. 3.1.2.4.

While reactors deliver a stable and continuous beam, spallation sources provide a pulsed beam[1] with high peak flux. Having a pulsed beam enables time-of-flight measurements. as the ones presented in this thesis work, where the energy of the neutrons can be calculated from their source-to-detector travel times.

3.1.1 NUCLEAR REACTORS

In a typical research reactor, neutrons (n) are produced by the fission process

$$^{235}U + n = \text{fission fragments} + 2.5\ n + 180\ \text{MeV} \tag{3.1}$$

Of the 2.5 neutrons emitted per process, one is used to sustain the chain reaction, ~ 0.5 is lost and one is available for external use. In this way, about 180 MeV of heat is produced per neutron [Arai and Crawford, 2009].

When each nuclear reaction causes one or more subsequent reactions, the process is called *chain reaction* and it may become uncontrollable. To sustain a nuclear reaction for a long time, it is necessary to control the neutron flux, so that the number of neutrons driving the chain reaction remains constant. This is done using rods of absorbing material (usually Boron), which can be inserted in the reactor core [Voigt, 2012].

At present the best reactor source for neutron scattering applications, especially considering the integrated flux, is the High-Flux Reactor (HFR) built in 1972 at the Institute Laue-Langevin (ILL) in Grenoble, France [Carlile, 2006]. Other noteworthy reactors include JRR-3 in Japan, built in 1962 and heavily modified in 1990 [Sakurai et al., 2002], HANARO in Korea (1997) [Lim et al., 2009], FRM-II in Germany (2004) [Neuhaus and Petry, 2007], OPAL in Australia (2007) [Bennett, 2008] and the China Advanced Research Reactor (2008) [Chen et al., 2006]. Except for HFR, all reactor sources are medium-sized research reactors with a typical power of 10-20 MW.

[1] With the notable exception of SINQ at PSI, see below.

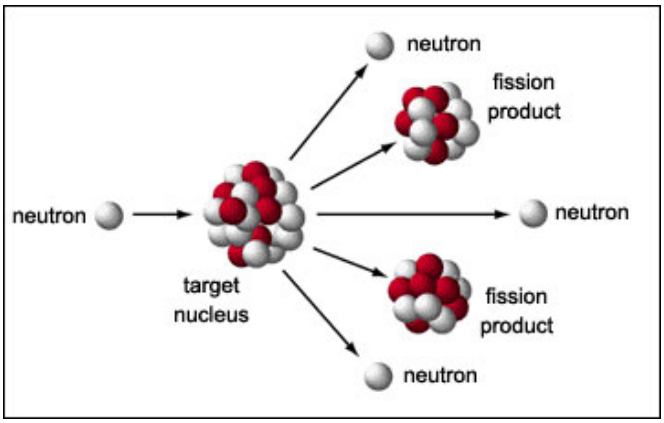

Figure 3.1: Schematic representation of the fission process of ^{235}U, used to produce neutrons in reactors [Atomic Archive, National Science Digital Library, 2015].

3.1.2 SPALLATION SOURCES

In spallation processes, neutrons are produced by high-energy protons striking a target made of neutron-rich material, such as mercury or tungsten [Anderson, 2011]. Spallation reactions consist of an initial series of inter-nuclear reactions, caused by spallation products (high energy neutrons, pions and spalled nuclei), followed by the evaporation of low-energy particles from the nucleus. To optimize the neutron production process, most protons should collide heavily with the target nuclei, rather than gradually lose energy. For this reason, the desired energy of the incoming protons is 1 GeV or higher [Arai and Crawford, 2009].

For typical target materials, 20 to 50 neutrons are released per spallation event, with the exact number depending on the specific material and on the energy of the incident particles. As a neutron production technique, spallation is about one order of magnitude more efficient than fission, if we consider the same amount of thermal energy deposited on the target/fuel element [Schober et al., 2008, Voigt, 2012]. The reactions happening in spallation sources exclude chain reactions. As a result, spallation sources are both more efficient and safer than reactor sources [Voigt, 2012].

Most spallation sources provide a pulsed time-of-flight neutron beam. For each pulse, the energy of the composing neutrons can be calculated from the time they take to travel from the source to the detector. Pulsed spallation sources include the Spallation Neutron Source (SNS) in the US [Gabriel et al., 2003, Mason et al., 2006], the Japanese Spallation Neutron Source (JSNS) at J-PARC [Nagamiya, 2012], and the ISIS source in the UK [Wilson, 1995]. Two more facilities are now under construction: the European Spallation Source (ESS) and

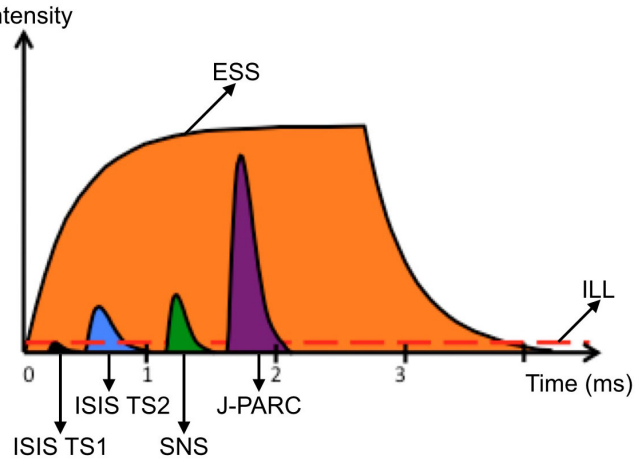

Figure 3.2: Expected pulse of the ESS compared to that of the major spallation sources worldwide and of the ILL. TS1 and TS2 are respectively the first and the second target station of ISIS [Thomason, 2008]. All data are relative to neutrons with a wavelength of 4÷5 Å. Modified from [Strobl, 2016].

the China Spallation Neutron Source (CSNS) [Fu et al., 2011]. The Swiss Spallation Neutron Source SINQ at the Paul Sherrer Institute (PSI) in Switzerland is an example of continuous spallation source [Wagner et al., 2006, Fischer, 1997].

Parameter	JSNS	SNS	ISIS (T1)
Proton energy (GeV)	3.0	1.0	0.8
Repetition (Hz)	25	60	50
Power (MW)	0.4[2]	1.4	0.16
Time integrated intensity ($\cdot 10^{14} n/cm^2/sr/s/eV$)	2.8	1.6	~ 0.1
Pulse peak intensity ($\cdot 10^{16} n/cm^2/sr/s/eV$)	6.0	1.3	< 0.1

Table 3.1: Features of the main neutron spallation sources available worldwide: the Japanese Spallation Source (JSNS) at J-PARC; the Spallation Neutron Source (SNS) at Oak Ridge (US); ISIS (target station 1) at Didcot (UK) [Ikeda, 2009].

At spallation sources, different configurations are used to produce high-energy protons. These involve one or more of the following accelerating devices: linear accelerators, cyclotrons and synchrotrons.

[2]The reported value is the one used for the performed experiments. The target value, expected to be reached in 2016, is 1 MW.

3.1.2.1 Linear accelerators

Linear accelerators or *linacs* are high current, high repetition rate accelerators, which can deliver proton bunches with a length of a few millisenconds. This is usually too long for "traditional" neutron scattering experimental setups and so, after being accelerated from the linac, protons are injected in a circular accelerator. Here the protons are compressed, increasing the peak flux. Spallation sources using this accelerator geometry, like the SNS in the US, are called *short pulse spallation sources* [Voigt, 2012].

The alternative approach is to feed the long pulse ($> 1ms$) from the linac directly into the target, and develop new instrumentation to exploit the high average flux. Spallation sources that use this accelerator arrangement, called *long pulse spallation sources*, include the ESS under construction in Lund, Sweden [Lindroos et al., 2011, Voigt, 2012].

3.1.2.2 Cyclotrons

Cyclotrons produce a steady proton beam, which generates a continuous current of neutrons once injected in the target. For example, a cyclotron is installed at the continuous source SINQ (PSI, Switzerland).

3.1.2.3 Synchrotrons

At ISIS (UK) and J-PARC (Japan), a synchrotron is used in combination with a H^- linac. After being accelerated in the linac, the ions pass by a thin alumina foil, which strips two electrons per ion. The resulting proton is then feeded into a synchrotron for further acceleration.

3.1.2.4 Moderators

The neutrons emitted in reactor and spallation sources have energies in the MeV range, corresponding to a wavelength $\lambda \sim 10^{-5}\mathring{A}$. This is much smaller than the length scales considered in neutron scattering experiments, usually ranging from 1 $\mathring{A}$ to 1 μm, corresponding to energies in the meV range. It is therefore necessary to slow down the neutrons, reducing their energy from the MeV to the meV range. This is achieved in the *moderator* through a series of collisions with particles of much lower energy, distributed over a large volume. The material of the moderator must absorb weakly, have high scattering cross-section and low atomic number, to maximize the energy transfer [Voigt, 2012, Willis and Carlile, 2009]. Standard moderator materials include H_2O, D_2O, H_2 and CH_4.

On average, to slow the neutron energy by 8 orders of magnitude (typical value) from the MeV to the meV range, about 25-30 collisions are necessary. The usual mean free path of neutrons in a hydrogen-rich material is in the order of a few millimetres, so the result can be achieved using tanks with side in the order of 10 cm. Moderators are kept at different temperatures, depending on the desired final energy of the neutrons. To prevent completely unmoderated neutrons from reaching the sample, the moderator geometry is designed so that there is no direct line-of-sight between the neutron production region and the ports opening to the neutron scattering instruments [Lefmann, 2014].

Moderator	Energy (meV)	Wavelength (Å)
Cold (20 K)	0.1-10	3-30
Thermal (300 K)	5-80	1-4

Table 3.2: Energy and wavelength ranges of neutron moderators [Willis and Carlile, 2009].

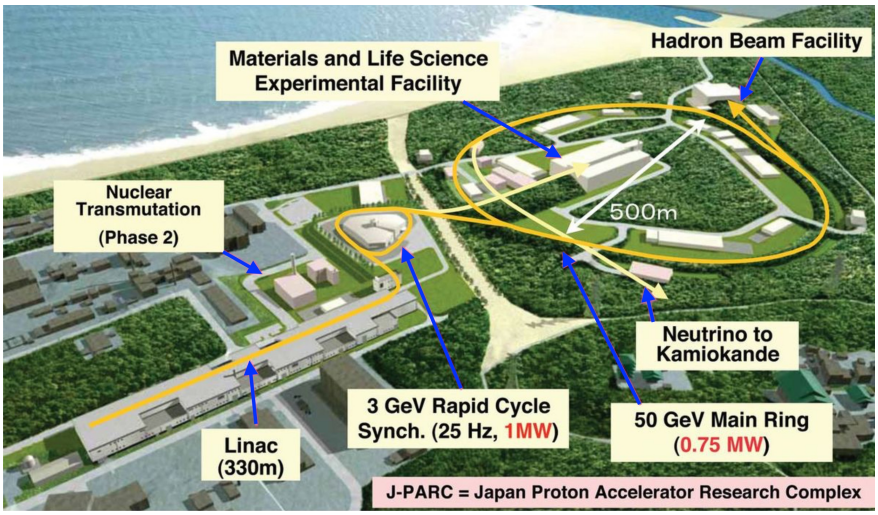

Figure 3.3: Bird's-eye view of the J-PARC research complex, with the accelerators and research facilities pointed by arrows. J-PARC consists of three proton accelerators and two research facilities (the Nuclear Transmutation Complex will be added in the future) [Nagamiya, 2012]. The accelerators are a linac, the 3 GeV Rapid-Cycling Synchrotron (RCS) and the 50 GeV Main Ring (MR). The research facilities are the Materials and Life Sciences Experimental Facility (MLF), where we performed our experiments, and the Hadron Beam Facility. Figure adapter from [J-PARC Center, 2015b].

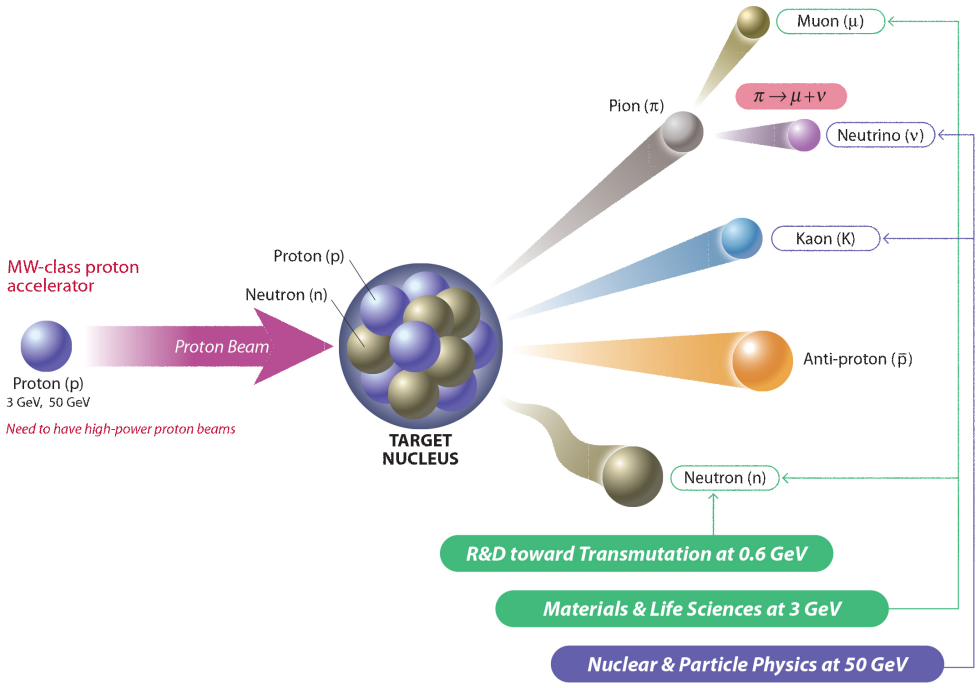

Figure 3.4: At J-PARC two proton beams, with energy of 3 GeV and 50 GeV, are used for different types of experiments. When colliding with the target nuclei, 3 GeV protons from the Rapid-Cycling Synchrotron (RCS) produce neutrons, protons and pions, which later decay in muons and neutrinos. 50 GeV protons from the Main Ring (MR) produce kaons, high-energy neutrinos, anti-protons and more [Nagamiya, 2009]. While muons and neutrons are used for materials and life sciences research, neutrinos and kaons are used for nuclear and particle physics research. Modified from [J-PARC Center, 2015b].

3.2 THE PULSED SPALLATION NEUTRON SOURCE

At J-PARC, neutrons are produced at the Japan Spallation Neutron Source (JSNS), installed at the MLF. The JSNS is designed to operate with the 3 GeV proton beam, with a power of 1 MW at a repetition rate of 25 Hz [Arai and Maekawa, 2014]. For a bird's eye view of J-PARC, see 3.3.

Three different moderators are in use at J-PARC: a *coupled moderator* for high flux experiments, a *decoupled moderator* for high resolution experiments, and a *poisoned decoupled moderator* for very high resolution experiments [Arai, 2009]. All moderators use supercritical hydrogen (H_2) at 20 K and at a pressure of 1.5 MPa [Neutron Source Section, Materials and Life Science Division, 2011]. The cryogenic hydrogen system is responsible for distributing H_2 and absorbing the heat generated in spallation reactions [Tatsumoto et al., 2010].

The coupled moderator is composed of two layers: the 20 K hydrogen moderator at the core and the so-called pre-moderator surrounding it, which is made of ambient water. The role of the pre-moderator is to get rid of most of the heat load before the neutrons enter the main moderator. This setup is designed to maximize the flux [Arai, 2009, Carpenter, 2015].

In the decoupled moderator, a neutron absorber is inserted between the reflector and the moderator. The absorber excludes low-energy neutrons from the moderator; as a consequence, the peak time width becomes sharp. In the poisoned case, the moderator contains an absorber plate, which makes the pulse profile even sharper [Arai, 2009].

3DND was developed basing on datasets collected at SENJU, a single crystal diffractometer installed at beamline BL18 of the MLF. SENJU requires pulses as bright as possible, to maximize the number of Bragg spots detected and increase their definition as a function of time-of-flight. Therefore, the BL18 beam guide departs the poisoned moderator, the one returning the sharpest pulse shape.

3.3 SENJU

This section presents the characteristics of single crystal diffractometers and gives a description of SENJU, the instrument where we collected our datasets.

3.3.1 TIME-OF-FLIGHT SINGLE CRYSTAL DIFFRACTOMETER

Single-crystal neutron diffraction is a technique for studying the atomic and magnetic structure of materials [Kawasaki et al., 2014]. In a typical single crystal neutron diffractometer, a beam of neutrons with different energies illuminates a single-crystal and the scattered neutrons are collected by position-sensitive detectors. Each collected neutron is labelled with its position (X and Y) and time-of-flight, which is the time the neutron takes to fly from the spallation target to the detector passing by the sample. In this way, different orders of a given reflection are collected by the same pixel at different time-of-flight [Keen et al., 2006].

For a given scattering angle 2θ, there is a direct proportionality between a neutron time-of-flight t, its wavelength λ and the crystal spacing d: being L the distance from the moderator to the detector, the momentum p of the neutron is

$$p = mv = m\frac{L}{t} = \frac{h}{\lambda} = \frac{\hbar}{k} \tag{3.2}$$

where as usual h is the Plank constant and $\hbar = \frac{h}{2\pi}$.

Using Bragg's law, $\lambda = 2d\sin\theta$, Eq. 3.2 can be rearranged as

$$t = 252.78 \cdot L\lambda = 252.78 \cdot L \cdot 2d\sin\theta \tag{3.3}$$

where t is in μs, L in m and λ and d in Å.

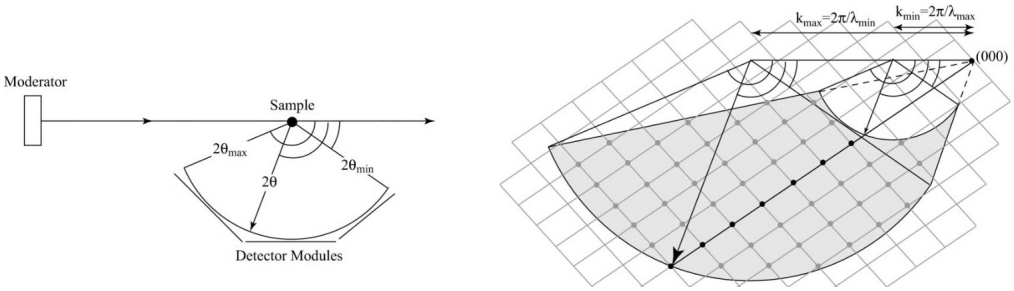

Figure 3.5: Sketch of the relationship between detector coverage and size of the considered reciprocal space region. The detectors cover scattering angles between $2\theta_{min}$ and $2\theta_{max}$ and collect data between the neutron time-of-flight ToF_{min} and ToF_{max}. For a fixed 2θ, the reciprocal space covered is enclosed between the two Edwald spheres of radii $2\pi/\lambda_{max}$ and $2\pi/\lambda_{min}$ (grey region in the Figure). Adapted from [Keen et al., 2006].

Having a large detector coverage enables recording more Bragg reflections (see Fig. 3.5), thus improving the data collection speed and reducing the number of required projections. Moreover smaller samples, or samples with more complex structures, can be investigated [Keen et al., 2006].

MLF, at J-PARC, hosts two single crystal diffractometers: iBIX, designed for biological samples, and SENJU, designed for crystal and magnetic structures analysis under extreme conditions (low temperature, high pressure, high magnetic field and a combination of these), with the possibility to also study superlattice reflections and diffuse scatterings [Tanaka et al., 2010, Tamura et al., 2012, Oikawa et al., 2014]. Thanks to its versatility, SENJU can provide new insights on materials of interest for solid-state physics, chemistry, materials science and related fields, providing information on how atoms are arranged in different materials [Kawasaki et al., 2014]. We performed our measurements at SENJU, chosen for its large detector coverage and relatively high flux.

3.3.1.1 Beamline design

The characteristics of the incoming beam depend on the choice of the moderator. In the case of SENJU, a poisoned decoupled moderator delivers a sharp pulse with symmetrical shape and short burst time [Tamura et al., 2012]. After being

SENJU	
Beamline	BL18
Moderator	Decoupled poisoned H_2 (20 K)
Incident neutron wavelength	$0.4 \div 4.$ Å(1^{st} frame) $4.6 \div 8.8$ Å(2^{nd} frame)
Neutron flux (sample position @1MW)	0.6×106 n/s/mm^2 (standard mode) 1.3×106 n/s/mm^2 (high-intensity mode)
Distance moderator-sample	34.8 m
Maximum lattice constant	50 Å
Sample size	$> 0.5 \times 0.5 \times 0.5$ mm^3 (@ 1MW)
2θ range	Horizontal: -13°÷ -167°; +58°÷ +167° Vertical: -29°÷ +29°
Beam divergence	0.29°
Detector	WLSF-type scintillator detector 4×4 mm^2/pixel 0.8 m or 1.3 m from the sample

Table 3.3: Main features of the time-of-flight neutron diffractometer SENJU [J-PARC Center, 2015a, Tamura et al., 2012].

emitted by the moderator, neutrons travel through a straight beamline, which delivers neutrons with a wavelength down to 0.4 Å [Tamura et al., 2012, Oikawa et al., 2014].

The sample position, placed at 34.8 m from the moderator, is surrounded by a number of detector banks. A removable vacuum chamber of 0.8 m in diameter and 1.2 m in heigh is available to simplify the alignment procedure and host sample equipment such as a cryostat, a 7 T magnet and so on [Oikawa et al., 2014]. Placing the sample in a vacuum chamber greatly reduces the noise recorded by the detectors [Kiyanagi, 2015].

SENJU is designed to provide a beam with a divergence, at the sample position, of about $\pm 0.30°$ for every wavelength of the spectrum. This is obtained via an elliptic guide with foci at 9.8 m and 34.8 m (sample position) from the moderator [Tamura et al., 2012]. The guide has a fixed section starting at 15.2 m and ending at 31.8 m, followed by an interchangeable section and two slits to collimate the beam [Oikawa et al., 2014].

Before the neutron guide there are three choppers: two bandwidth choppers and a so-called T_0 chopper. The bandwidth choppers, installed at 7.2 m and 9.75 m from the moderator, can operate at 25 or 12.5 Hz, enabling to select a

bandwidth of 4.4 Å or 8.8 Å. The role of the T_0 chopper, placed at 10.2 m from the moderator, is to suppress high-energy neutrons and γ rays and it can operate at 50 or 25 Hz [Oikawa et al., 2014].

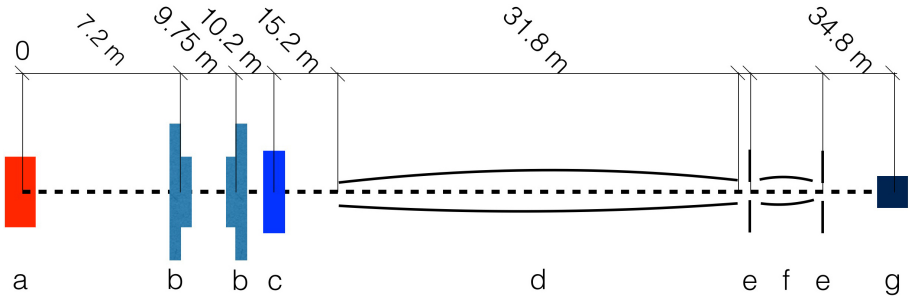

Figure 3.6: Sketch of the SENJU structure. *a* is the moderator; *b* are the two bandwidth choppers, used to select a bandwidth of 4.4 or 8.8 Å; *c* is the T_0 chopper, used to stop fast neutrons; *d* is the elliptical neutron guide; *e* are the slits used to collimate the beam; *f* is an interchangeable section and *g* is the sample.

3.3.1.2 Detectors arrangement at SENJU

At SENJU the sample position is surrounded by 37 detectors, each with an area of 256×256 mm^2, divided in 64×64 channels (pixel size: 4×4 mm^2). One detector is placed underneath the sample position and the other 36 are placed around it, arranged in detector banks of three detectors each. For each bank, the detectors are vertically aligned with a step of 22.18° between the middle of the central one and the middle of the other two (see Figure 3.7). In the standard configuration, the detectors at the center of each bank (equatorial detectors) are at 0.8 m from the sample position. The detector banks can be moved up to 1.3 m away from the sample to permit operations in the sample region. In all configurations, the angular step between the detector banks is 22.5°. All reported values are from [Oikawa et al., 2014, Kawasaki et al., 2014].

With the detector banks at 0.8 m from the sample position, SENJU offers an angular coverage of about four steradians (30% of the total), which is the maximum value for the instrument. In this configuration, the gap between the detector modules is 25 mm vertically and 12 mm horizontally [Kawasaki et al., 2014].

3.3.1.3 Structure of a detector module

The reliability and stability of each detector module is an essential factor for the success of a single crystal diffractometer. In particular, detectors need to have

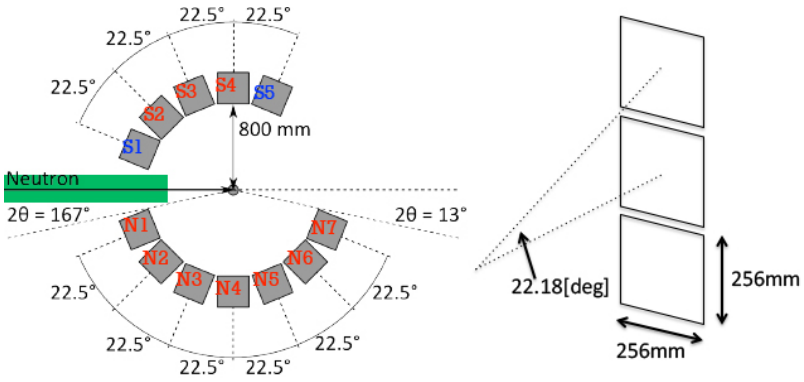

Figure 3.7: *Left*: schematic top view of the SENJU diffractometer at BL18, MLF, J-PARC. The diffractometer consists of 12 detector modules surrounding the sample position (five on the south side and seven on the north side). Each consists of three vertically aligned detector units (see *right*). The modules are normally placed at 800 mm from the sample at 22.5°steps. For each module, the units are vertically separated by 22.18°. An additional module is placed underneath the sample. Each detector module has a sensitive area of 256×256 mm^2 divided in 64×64 channels. Image courtesy of R. Kiyanagi; for additional details see [Oikawa et al., 2014, Kawasaki et al., 2014].

high efficiency for detecting thermal neutrons, good resolution, low gamma ray sensitivity and tolerance to magnetic fields [Kawasaki et al., 2014].

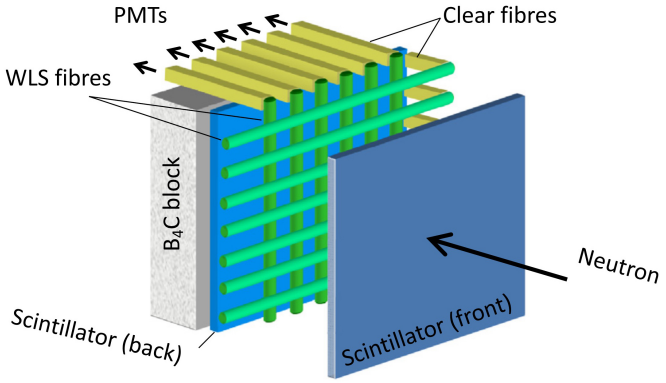

Figure 3.8: Schematic view of the head (electronics not shown) of the diffraction detectors installed at SENJU. From [Kawasaki et al., 2014].

The detector modules installed at SENJU consist of the following elements [Kawasaki et al., 2014]:

1. *Detector head*, consisting of two ^{10}B-doped ZnS scintillators with a size of 256 × 256 mm^2 and, sandwiched between the scintillator plates, an

array of wavelength shifting fibres. The light emitted in the interaction of a neutron with the scintillators is read by the fibres, placed along the X and Y direction. The coordinates of the neutron collision are determined by the intersection of the stimulated fibres. Each detector module consists of 64×64 pixels (pixel size: 4×4 mm^2);

2. *Signal processing electronics*, to exclude contributions from neutron and gamma-rays events (the detector works in photon-counting mode);

3. *Acquisition electronics*, to store data remotely in list mode (event format), so to have the maximum post-processing flexibility. The listed data are in 32-bit format and contain information on both the scattered neutrons and the T_0 signal occurring at 25 Hz. The neutron-event data consists of the x, y and time-of-flight coordinates of the neutron-detector collision. The data are read out by a module and transferred to a remote storage device via a SiTCP network [Uchida, 2012].

3.3.1.4 Data processing

Once stored, the diffraction data can be visualized using STARGazer, a software package for analysing three dimensional diffraction data (x, y and time-of-flight) [Ohhara et al., 2009]. STARGazer, originally developed for the protein crystallography diffractometer iBIX at BL03, J-PARC, has been adapted to the geometry of SENJU [Ohhara et al., 2009, Tanaka et al., 2010, Tamura et al., 2012].

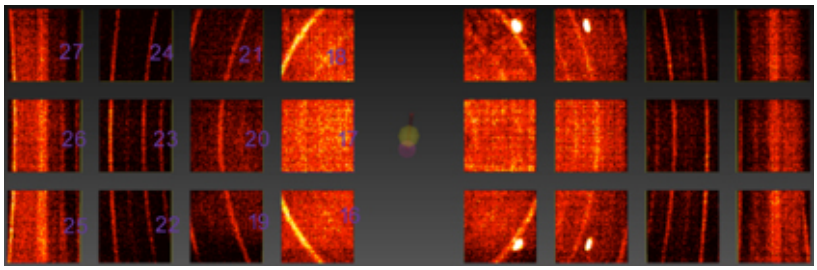

Figure 3.9: Travelling in time-of-flight using STARGazer: diffraction pattern (channel 270) for a Tungsten-based sample studied at SENJU in March 2015. The crystalline structure of the sample is unknown and shows high horizontal and vertical symmetry.

3.3.2 SETUP USED AT BL18

In the 3DND setup used at SENJU (see Fig. 3.10), data were simultaneously collected by the scintillator detectors of the beamline (*far-field detectors*) and by

an event-counting detector mounted a few centimetres downstream the sample (*near-field detectors*) [Tremsin et al., 2012]. The far- and near-field detectors were used to collect, respectively, diffraction and transmission data. A sample stage and a measurement control computer were also added to the SENJU standard setup.

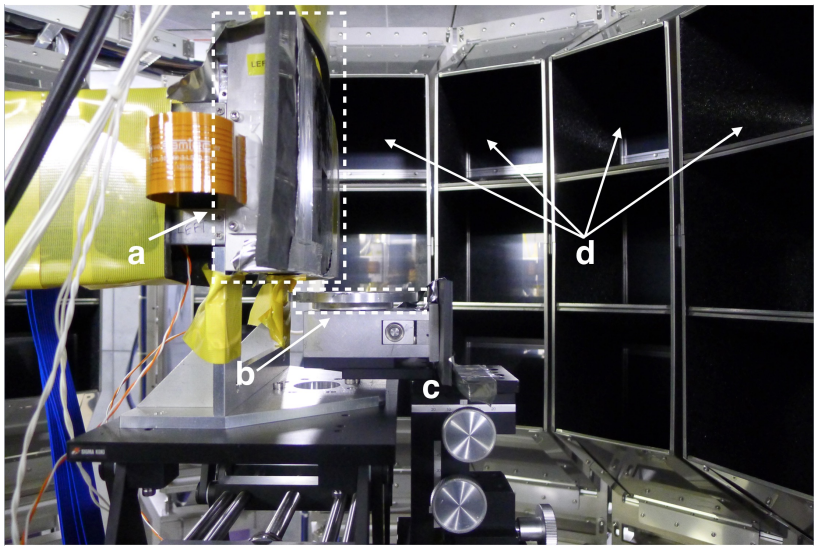

Figure 3.10: Detector setup used to collect data at SENJU, as seen from the north detector banks. In the foreground are visible the near-field detector (*a*), the rotation stage (*b*) and the sample stage (*c*). In the background, four far-field detector banks are pointed with arrows (*d*).

3.3.2.1 The MCP detector

The near-field detector we used was a microchannel plate (MCP) detector, manufactured by NOVA Scientific (Sturbridge Technology Park, MA, US), and equipped with four fast Timepix readouts [Tremsin et al., 2013].

MCP detectors are solid state array detectors, typically consisting of $10^4 \div 10^7$ electron multipliers in parallel, each 10-100 μm in diameter. They are widely used to detect both particles (electrons and ions) and radiation (UV and X-rays). To detect neutrons, ^{10}B-doped microchannels are used: when a neutron interacts with their surface, the following reaction takes place:

$$^{10}\mathrm{B} + n = ^{7}\mathrm{Li} + ^{4}\mathrm{He} + \mathrm{Q}(2.79\mathrm{MeV}) \tag{3.4}$$

where Q is the amount of energy released in the reaction. Given the energies, several electrons are emitted per neutron collision [Tremsin et al., 2005]. The

electrons are then amplified to create a cascade, to be detected by an anode at the end of the detector. For a schematic view, see Fig. 3.11.

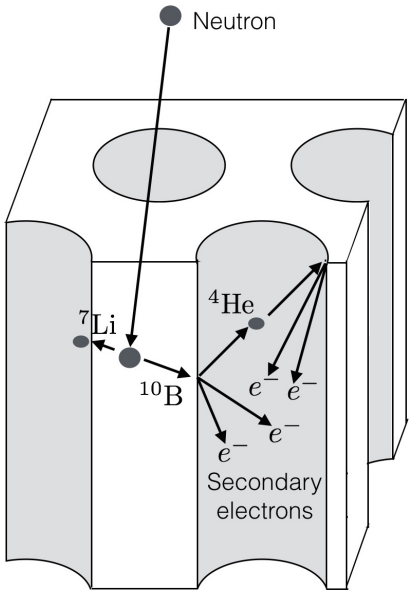

Figure 3.11: Neutron detection with a boron-doped multichannel plate detector. Adapted from [Tremsin et al., 2005].

Consisting of 512×512 pixels, each with a size of 55×55 μm^2, the near-field detector has an active area of 28×28 mm^2. With a count rate of 3 MHz at 1200 frames per second, the detector has both high spatial and temporal resolution [Tremsin et al., 2013].

3.3.3 FAR-FIELD AND NEAR-FIELD DETECTORS COMMUNICATION

The network setup used to simultaneously collect data using the far-field and the near-field detector is shown in Fig. 3.12. The desktop computer controlling the rotation stage hosting the sample was also responsible for sending the data acquisition signal (DAQ) to both the near- and far-field detectors. In the second case, the DAQ is then distributed to each module. The DAQ signal activates the detectors for data acquisition, which starts with the T_0

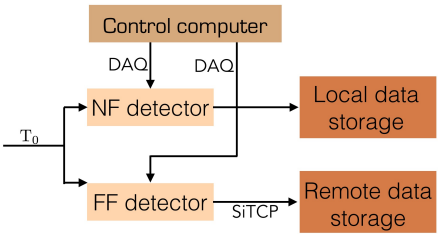

Figure 3.12: Structure of the network set-up used to collect data for the 3DND experiment at SENJU.

signal, broadcasted when the proton pulse hits the target [Kiyanagi, 2015]. The time interval between the T_0 pulses is 40 ms. The data acquisition is stopped by another DAQ signal.

3.4 ADDITIONAL EXPERIMENTS

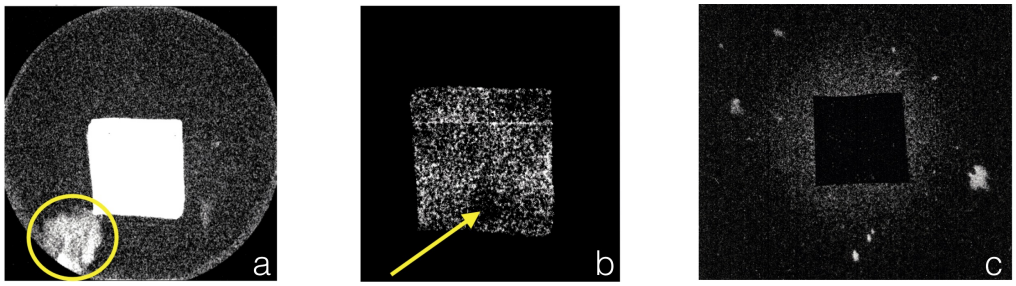

Figure 3.13: Example of the data collected at ENGIN-X (*a*, *b*) and ICON (*c*). *a* and *b* are relative to the same time-of-flight and show, respectively, a diffraction spot and the relative extinction spot as collected by the MCP detector. As a sample, an Al cube was considered. *c* shows the backscattering Laue pattern recorded, for one projection, at ICON when the Fe sample, also studied at J-PARC, was illuminated using a non-pulsed, white beam.

Preliminary tests were done at ISIS (beamline ENGIN-X) and at PSI (beamline ICON). At ENGIN-X measurements were performed both using only an MCP detector, identical to the one used at SENJU, mounted in transmission mode downstream the sample, and using both the MCP and the diffraction detectors of the beamline, in line with what done at SENJU but with a much smaller detector coverage. At ICON data were collected using the detector geometry described in [Peetermans et al., 2014], with a scintillator mounted behind the sample, in backscattering Laue mode. Example of the collected data are shown in Fig. 3.13.

To develop the data analysis algorithms, we based on the data collected at SENJU: at J-PARC the beam is brighter than at ISIS, resulting in a higher signal-to-noise ratio for a given exposure time. Moreover, working with a time-of-flight permits to investigate more grains (less spots overlap, see Ch. 6) than using a continuous one, as available at PSI.

4

Methodologies

Contents

TIME-OF-FLIGHT 3DND returns information on the 3D shape, orientation and juxtaposition of the grains composing a given polycrystalline sample. In this thesis work, two ToF 3DND methodologies have been developed, each requiring a different experimental setup. In methodology I an imaging (*near-field*) detector is mounted in transmission mode, collecting real space information. In methodology II, data are collected using both a near-field transmission detector and diffraction (*far-field*) detectors, recording Bragg spots. Both methodologies have been implemented at SENJU, J-PARC. For a description of the beamline setup, see 3.3.2.

This chapter presents the two ToF 3DND approaches, together with the relative experimental setups. The algorithms developed to reconstruct the shape of the grains (from transmission data) and their orientation (both from transmission and from diffraction data) are presented in Chapters 6 and 7, respectively. In Fig. 4.1, the two methodologies are presented as flowcharts.

Both 3DND methodologies were developed starting from the data collected at SENJU in Summer 2015 and Spring 2016, respectively imaging a Fe rod and a Co-Ni-Ga sample with a "bamboo" structure, consiting of two large cubes on top of each other. The main characteristics of the two experiments are reported in Table 4.1.

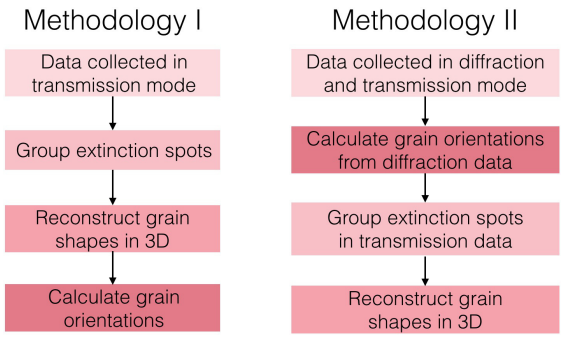

Figure 4.1: Main steps of methodologies I and II. In the two flowcharts, boxes corresponding to the same steps have the same color.

Date	Sample	Beam power (MW)	ToF intervals
Summer 2015	Fe rod	0.4	2423
Spring 2016	Co-Ni-Ga bicube	0.2	2500

Table 4.1: The 3DND algorithms were developed analysing data collected at SENJU in Summer 2015 and Spring 2016. In the table above, the main characteristics of the experiments are listed. The Fe sample is a cylinder 5 cm long and with a diameter of 1 cm; the Co-Ni-Ga sample has a "bamboo" structure, with two 4 mm-sized cubes on top of each other.

4.1 METHODOLOGY I

In its simplest form (methodology I) ToF 3DND only requires an imaging detector with high spatial and temporal resolution, mounted downstream from the sample to collect the transmitted time-of-flight beam. Thanks to the time resolution, the detector returns both the pixel coordinates and the time-of-flight of each neutron collision on the its surface. Grain shape reconstruction algorithms were developed using data collected at SENJU using a microchannel plate (MCP) detector, described in Sec. 3.3.2.1.

Each time a grain satisfies the Bragg condition, the intensity diffracted out of the direct beam results in a locally enhanced attenuation in the collected signal, visible as an "extinction" spot [Ludwig et al., 2008]. The process is sketched in Fig. 4.2.

As an output, the MCP detector returns the ToF when the collected neutrons are recorded. Time-of-flight can be converted into wavelength using (see 3.2)

$$p = m\frac{L}{t} = \frac{h}{\lambda} \tag{4.1}$$

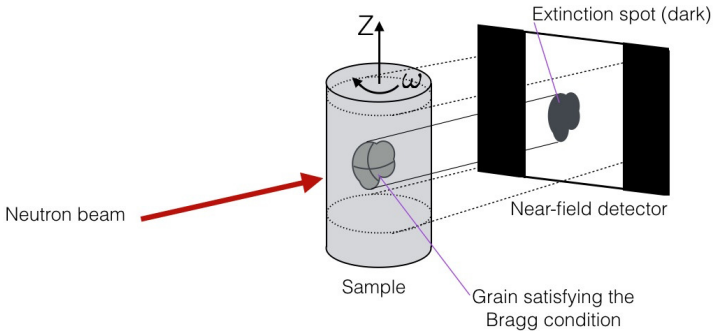

Figure 4.2: The minimal ToF 3DND setup (methodology I) consists of an imaging detector with high spatial and temporal resolution mounted in transmission mode. When a grain satisfies the Bragg condition, the contribution to the absorption coefficient is strong enough that extinction spots become visible.

which, for the data we collected, becomes

$$\lambda = (\mathrm{ToF} + \Delta t) \cdot \frac{3.956}{\text{flight path}} \cdot 1000 \tag{4.2}$$

where λ is in Å, ToF is in seconds, the flight path is in meters (at SENJU, flight path $= 34.8$ m) and the trigger shift is $\Delta t = 3.5 \cdot 10^{-6}$ sec.

For each exposure, the near-field detector returned a series of images, each relative to a given time-of-flight interval. Each interval had fixed width (12.8 μs) and is denoted as Λ_i, with $1 \leq i \leq 2423$ for the Fe sample and $1 \leq i \leq 2500$ for the Co-Ni-Ga sample.

The center point of Λ_i [Å] is given by

$$\Lambda_i = 0.4 + \frac{4}{\mathrm{MaxIm}} \cdot i + \lambda_{\mathrm{shift}} \tag{4.3}$$

where MaxIM is the total number of images considered for a certain sample (2423 for Fe and 2500 for Co-Ni-Ga) and λ_{shift} is a correcting factor due to a trigger shift in the MCP detector. In the measurements we performed, $\lambda_{\mathrm{shift}} = 0.0731$ Å.

At the j-th angular position, extinction spots relative to a given grain are collected at a set of Λ_i values, $\{\Lambda_{i,j}\}_{i,j}$. The aim of the developed algorithms is to identify among all the collected extinction spots, relative to all the grains in the sample, those relative to a given grain, thus obtaining the set $\{\Lambda_{i,j}\}_{i,j}$.

Once the extinction spots are grouped, the 3D shape of the individual grains can be reconstructed by backprojecting, from each angle, the combination of the relative extinction spots (see Fig. 6.15 for an overview). As a result, a tomographic reconstruction of the grain structure within the sample is obtained.

To index a grain, we considered the set of extinction spots collected at $\{\Lambda_{i,j}\}_{i,j}$ and we studied how the extinction spots moved as the sample rotates (see Ch. 7).

To the best of our knowledge, the approaches we used to reconstruct the shape of the grains and their orientation from time-of-flight data collected in transmission mode are both new.

4.2 METHODOLOGY II

In methodology II we acquired data using both a near-field detector, collecting transmission data as in methodology I, and a far-field detector, collecting the signal diffracted by the sample. Every time a grain satisfied the Bragg condition, a diffraction spot was recorded by the far-field detectors and, at the same time, an extinction spot was recorded by the near-field detector (see Fig. 4.3).

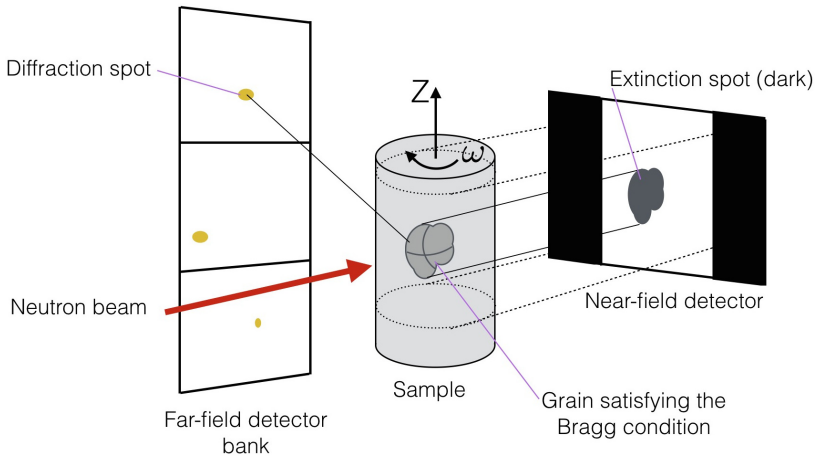

Figure 4.3: In methodology II, near- and far-field detectors are used to collect, respectively, transmission and diffraction data from a polycrystalline sample. Each time a grain within the sample satisfies the Bragg condition, a diffraction spot is recorded by the far-field detectors and the corresponding extinction spot is recorded by the near-field detector.

The diffraction patterns were analysed using GrainSpotter, a software originally developed for X-rays, which indexes the data and returns a number of unique orientations, each corresponding to a different grain [Schmidt, 2014]. Considering a given orientation, we calculated which extinction spots correspond to the relative grain. After grouping the spots, the shape of the grain was reconstructed by backprojection, as in methodology I. Method II could po-

tentially reconstruct small grains that can be difficult to observe using the MCP detector alone.

5

McStas simulations

Contents

McSTAS is a software package to simulate neutron scattering experiments via Monte Carlo ray-tracing [Lefmann and Nielsen, 1999, Willendrup et al., 2014b]. Before doing the "real" experiments at SENJU, we used McStas to test the feasibility of ToF 3DND.

This chapter presents the basics of the Monte Carlo method and of McStas, together with a review of the performed ToF 3DND simulations.

5.1 THE MONTE CARLO METHOD

After WWII, considerable efforts were made to study radiation shielding and neutron diffusion, which physicists could not calculate using conventional, analytical mathematical methods. The impasse was broken by three scientists working at the Los Alamos National Laboratory: John von Neumann, Stanislaw Ulam and Nicholas Metropolis, members of a classified project named after the famous Monte Carlo casino [Kalos and Whitlock, 2008, Thomopoulos, 2012]. Ulam had the idea of calculating integrals using random experiments, and von

Neumann developed the relative algorithm on the ENIAC computer [Eckhart, 187].

In Monte Carlo integration, integrals are calculated using random numbers. The technique is today used to simulate processes, physical systems and phenomena that are difficult or impossible to describe using other mathematical tools. A more detailed definition is given by Halton: "*the Monte Carlo (MC) method is defined as representing the solution of a problem as a parameter of a hypothetical population, and using a random sequence of numbers to reconstruct a sample of the population, from which statistical estimates of parameters can be obtained*" [Halton, 1970]. The method is widely applied in different areas including particle physics (simulation of subnuclear particle collisions), mathematics (solving complex integrals in multiple dimensions), finance (estimation of market uncertainties), computer graphics (object rendering in 3D) and search and rescue [Wikipedia, 2016, Lefmann, 2014].

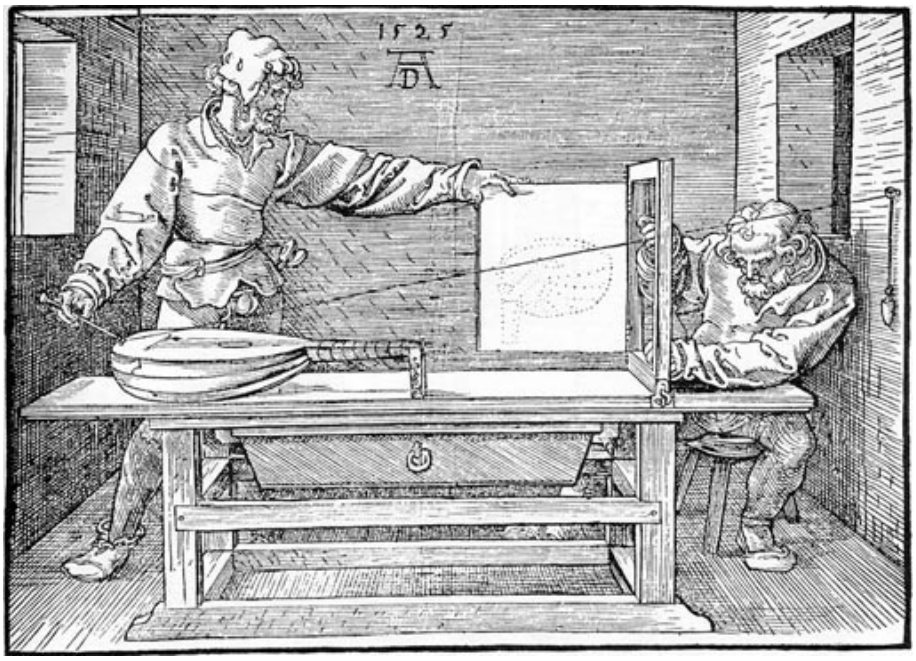

Figure 5.1: Man drawing a lute, by Albrecht Dürer (1525). In this drawing, Dürer illustrates a (very tedious) technique to draw prospective using ray-tracing. *"Place a lute or another object to your liking as far from the frame as you wish, but so that it will not move while you are using it. Have your assistant then move the pointer..."* [Dürer, 1977]

5.1.1 MONTE CARLO RAY-TRACING

The ray-tracing method is based on the laws of geometrical optics, which assumes light to propagate in linear paths, without taking into account wave-like phenomena such as diffraction and interference. The method, first introduced in the '60s to help develop new optical systems[1], can be combined with Monte Carlo techniques to generate highly realistic images [Spencer and Murty, 1962, Jarosz, 2008, NVIDIA, 2016]. In computer graphics, the three principles of Monte Carlo ray-tracing are to a) cast rays to every pixel of a scene, b) recursively cast secondary random rays from the visible points, c) send rays to light sources (see Fig. 5.2) [Gillies, D. F., 2016].

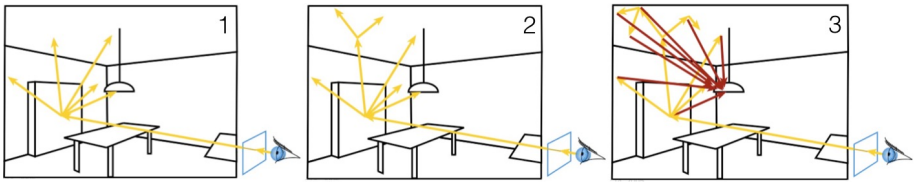

Figure 5.2: Principles of Monte Carlo ray tracing: 1. cast rays to every pixel of a scene, 2. recursively cast secondary random rays from the visible points, 3. send rays to light. Modified from [Gillies, D. F., 2016].

5.2 MCSTAS

McStas stands for **M**onte **c**arlo **S**imulation of **t**riple-**a**xis **s**pectrometers and was originally developed at Risø National Laboratory to provide a modelling software that could simulate the performance of a whole neutron scattering instrument [Baltser, 2013]. The first version of McStas was released in October 1998 [Lefmann and Nielsen, 1999]. The code is actively being developed and supported by the Danish Technical University, the European Spallation Source, the Institut Laue Langevin in France, the Paul Sherrer Instituit in Switzerland and the University of Copenhagen. A sister package, McXtrace, is available to simulate X-ray scattering experiments [Bergbäck Knudsen et al., 2013].

McStas includes a collection of predefined sources, optical components, samples and detectors [McStas website, 2016]. The position and orientation of the components can be set by the user, designing virtual experiments with the same components and geometry used in actual experiments. McStas provides

[1] For an early precursor of ray tracing, see Fig. 5.1 for the instrument used by Dürer.

the option of simulating pulsed sources, emitting neutrons with the relative flux and energy.

5.2.1 THE NEUTRON RAY

In analogy with the light rays used in computer graphics, McStas simulations use *neutron rays*, which can be thought as statistical ensembles of neutrons with identical characteristics (energy, position, polarisation). Using rays instead of particles increases the efficiency of McStas simulations: in an experiment, many neutrons are never detected because absorbed or scattered (mostly in guides).

Each ray has an initial weight factor p_0, calculated from the energy spectrum of the source. When the ray hits the j-th beamline component, its weight factor is multiplied by π_j. The weight factor for a neutron that interacted with n components is given by the product of all contributions [Willendrup et al., 2014a]:

$$p = p_n = p_0 \prod_{j=1}^{n} \pi_j \tag{5.1}$$

In general, $0 \leq \pi_j \leq 1$. To optimize the computing time, the value of the weight factor is updated during a simulation.

Another expedient used to optimize computational time is to simulate only the neutron rays that can hit the detector (directional sampling). Instead of being emitted by the neutron source over 4π, rays are limited to a solid angle Ω subtended by an arbitrary aperture, as seen from the source [Baltser, 2013]. In this approach, the weight factor p_i is

$$p_i = \frac{\Omega}{4\pi} p_0 \tag{5.2}$$

5.2.2 UNCERTAINTY OF THE SIMULATIONS

When a real measurement is performed, the relative errors depend on the number of collected neutrons. For a McStas experiment, the error depends on the number of rays employed. In the following, the characteristics of the different errors are explained, basing on the works [Lefmann et al., 2008, Vickery et al., 2014].

5.2.2.1 Intensity and variance from McStas simulations

In a typical simulation the detectors return, pixel by pixel, a count of the collected neutron rays together with the respective weights. Considering a pixel i

hit by N different rays, each with weight factor $p_{i,j}$, the collected intensity is

$$I_i = \sum_{j=1}^{N} p_{i,j} = N\overline{p_i} \tag{5.3}$$

where $\overline{p_i}$ is the average weight factor. For a discrete set of weight factors $\{p_j\}_{j=1,N}$, each corresponding to n_j rays,the variance of the simulated intensity can be calculated using the fact that the variance of a sum is the sum of its variances:

$$\sigma^2(I_i) = \sum_{j=1}^{N} n_j p_j^2 \tag{5.4}$$

Supposing that the values p_j are continuously distributed, the collected intensity I_i and the relative variance $\sigma^2(I_i)$ can be written as

$$\begin{aligned} \sigma^2(I_i) &= \sum_{j=1}^{N} p_j^2 \\ I_i &= \sum_{j=1}^{N} p_j \end{aligned} \tag{5.5}$$

For each pixel, the McStas detectors return the standard deviation $\sigma(I_i) = \sqrt{\sigma^2(I_i)}$, which is the error for the collected intensity [Willendrup et al., 2014a].

5.2.2.2 Reliability of simulations

I_i from 5.5 is also an estimate of the average number of neutrons per second hitting a detector bin in a real detector. Increasing the number of rays does not affect the mean value of I_i but it affects $\sigma(I_i)$, measuring the precision (in the sense of reproducibility) of the simulation [Vickery et al., 2014].

In a real experiment, when the number of neutrons n_i reaching a pixel i is greater than ~ 20, Poisson statistics can be applied[2], with precision increasing as the number of counts increases. Following Poisson statistics, the variance per pixel is

$$\sigma_i^2 = n_i \tag{5.6}$$

[2]The binomial distribution describes n yes/no experiments, each of which yields success with probability p. When the number of counts is at least 20, the binomial distribution is well approximated by the Poisson distribution [sta, 2016].

Considering all pixels, the total number of counts and the variance are, respectively,

$$N = \sum_i n_i \tag{5.7}$$

and

$$\sigma^2 = \sum_i \sigma_i^2 = N \tag{5.8}$$

The formula of the intensity and the relative error, both for real and for simulated data, are reported in Tab. 5.1.

Type of data	I	σ
Real	N	$\sqrt{N}$
Simulated	$\sum_{j=1}^{N} n_j p_j^2$	$\sqrt{\sum_{j=1}^{N} n_j p_j^2}$

Table 5.1: Formula of the collected intensity and relative error for real data and for data simulated using McStas. For the real data, it is assumed that more than 20 counts are registered, and thus that the Poisson statistics can be applied. N is the number of collected neutrons in the real case, and of collected rays in the simulated case. In the simulated case, p_j is the weight relative to the j-th interval, consisting of n_j rays.

A simulated experiment returnes, for each pixel i, an intensity I_i and the relative error σ_i. Considering an acquisition time t, the number of counts and the error are $n_i = tI_i$ and $err = t\sigma_i$. From these expressions, it is possible to estimate the time necessary to acquire data with a given precision. To do this, the error for the simulated experiment must be smaller than the error for the real one:

$$t\sigma_i \leq \sqrt{n_i} = \sqrt{tI_i} \tag{5.9}$$

which gives a maximum exposure time t_{max}:

$$t_{max} = \frac{I_i}{\sigma_i^2} \tag{5.10}$$

Since Eq. 5.10 must be satisfied for every pixel in the considered detector, the selected acquisition time must be smaller than the shortest of the times returned by the pixels. When condition 5.10 is satisfied for every pixel, the noise for the simulated dataset is smaller than for the real one, and the simulated dataset can be used to estimate the required count time for a real experiment.

5.3 SIMULATION OF THE EXPERIMENT AT SENJU

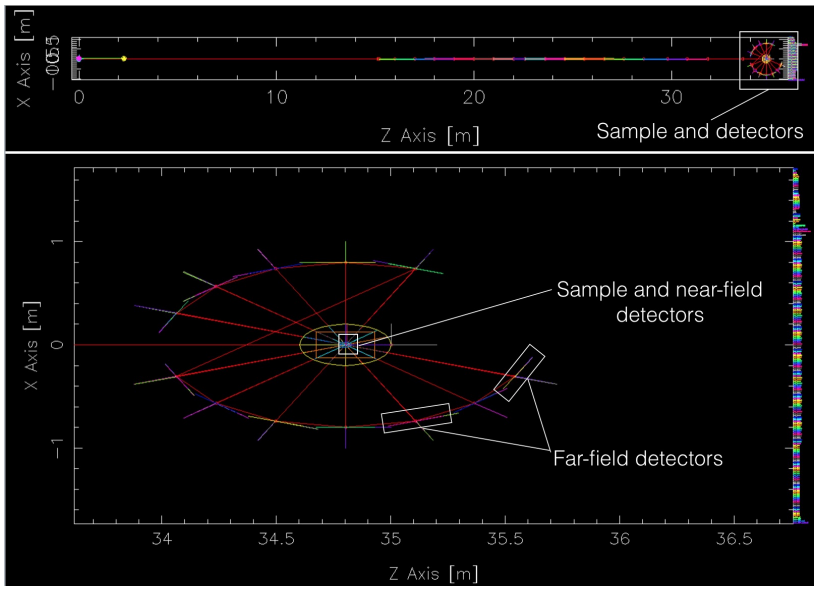

Figure 5.3: Overview of the McStas simulation of SENJU. *Top*: overview of the entire beamline. Following the convention used in McStas, the z axis is along the neutron propagation axis, the y axis is vertical up, and the x axis points left when looking along the z-axis, completing a right-handed coordinate system [Willendrup et al., 2014a]. *Bottom*: zoom on the region where the sample and detectors are. Clearly visible are the SENJU far-field detectors surrounding the sample region.

A McStas simulation of SENJU was developed basing on the code by K. Oikawa [Tamura et al., 2012] (see Fig. 5.3). The simulation code is outlined in Appendix A and was developed with the help of Erik Knudsen and Peter Willendrup, NEXMAP, DTU. E. Knudsen developed two new components, `FITS_monitor.comp` and `HDB_monitor.comp`, to output in the same format of the experiments at SENJU [3].

McStas simulations were used in different stages of the project. Initially, the feasibility of a ToF 3DND experiment at SENJU was simulated using as a sample three iron single crystals, defined using the McStas component `Single_crystal` [Willendrup et al., 2014a]. Each crystal was a cube with 2 mm side. Fig. 5.4 shows the typical output.

A more realistic sample was used to estimates of the exposure time necessary to study the Fe sample at SENJU: cylindric shaped, 1 cm tall and with a 1 cm

[3] The scripts used to simulate ToF 3DND experiments at SENJU are available at https://github.com/albusdemens/McStas_3DND

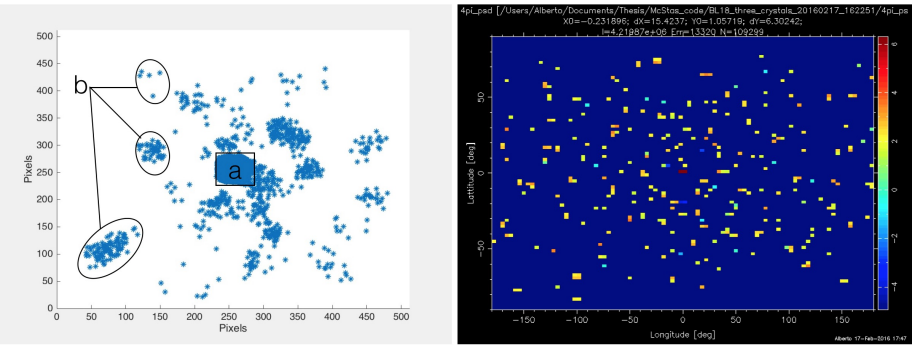

Figure 5.4: Results of the McStas simulation performed to test the feasibility of ToF 3DND. As a sample, three iron single crystals were considered. *Left*: Transmitted (a) and diffracted (b) rays collected by the near-field detector. *Right*: diffracted rays collected by a 4π monitor centered on the sample.

diameter, made of 20 iron grains (see Fig. 5.5). The procedure to build the shape of the grains was to select twenty random points inside a cube, build the corresponding 3D Delunay tessellation[4] using the software library `Voro++` [Rycroft, 2009], assign a random orientation to each region and extracted a cylinder from the cube [Okabe et al., 2009].

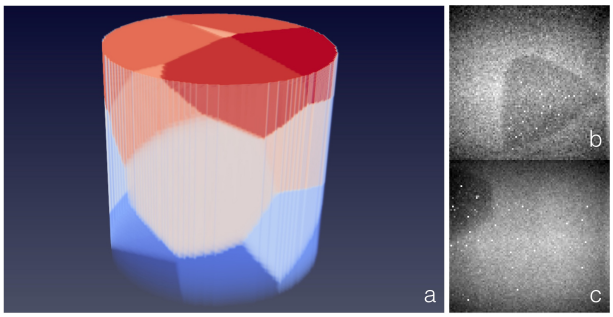

Figure 5.5: To estimate the acquisition time for the measurements performed at SENJU, McStas simulations were performed using a simulated iron sample (*a*), 1 cm long and with 1 cm diameter, made of 20 regions randomly oriented. To build the sample, a Delunay tessellation was calculated from a random points distribution. Different grains are plotted in different colors. *b* and *c*: extinction spots collected by studying the simulated sample using McStas. Simulation performed using 10^{11} rays.

The main difference between the McStas simulations used for feasibility tests and those used to estimate the exposure time is the complexity of the considered sample, which determines how to simulate internal scattering. For the

[4]For a brief introduction to Delunay tessellation, see [Salvatore, , Fortune, 1992].

three crystals sample, internal scattering was treated in the standard way, using the built-in functionalities of the `Single_crystal` component. The complexity of the iron cylinder required a new approach, to break the sequential nature of McStas. This has already been done, for example via the `JUMP` component, to make simulations more efficient (see Fig. 5.6) [Willendrup et al., 2014a]. The sample volume consisted of 100x100x100 voxels (value 0 was assigned to the voxels outside the cylinder). Each time a neutron ray n_j hit a voxel $v_i(\bar{r})$ the following procedure was applied:

1. Translate the neutron ray so that it hits the voxel $v_c(\bar{c})$ at the centre of the sample, defined as a `Single_crystal` component.

$$n_j(\bar{r}) \rightarrow n_j(\bar{c}) \tag{5.11}$$

2. Move the voxel hit by the neutron, $v_i(\bar{r})$, to the central position, preserving its characteristics.

$$v_i(\bar{r}) \rightarrow v_i(\bar{c}) \tag{5.12}$$

3. Let the incident ray interact with the translated voxel $v_i(\bar{c})$.

$$n_j(\bar{c}) \rightarrow \widetilde{n}_j(\bar{c}) \tag{5.13}$$

4. Translate the ray $\widetilde{n}_j(\bar{c})$ back to the original position $\bar{r}$.

$$\widetilde{n}_j(\bar{c}) \rightarrow \widetilde{n}_j(\bar{r}) \tag{5.14}$$

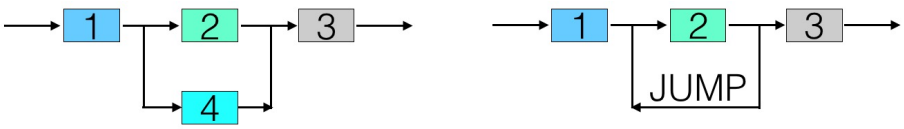

Figure 5.6: To simulate internal scattering in a realistic polycrystalline sample, we developed a new approach that breaks the sequential nature of McStas. *Left:* standard sequential nature of McStas, where a neutron beam interacts with a series of components (numbered boxes in the Figure) with no loops. *Right:* the `JUMP` component is an example of sequence breaking, introduce to improve the simulations efficiency [Willendrup et al., 2014a].

In the data collected at SENJU by the far-field detectors, both isolated diffraction spots and rings were observed. McStas was used to simulate diffraction from a powder of Fe crystallites, to confirm that the rings were due to a sample region with a powder-like structure, filling the space that is not occupied by the grains (see Fig. 5.7).

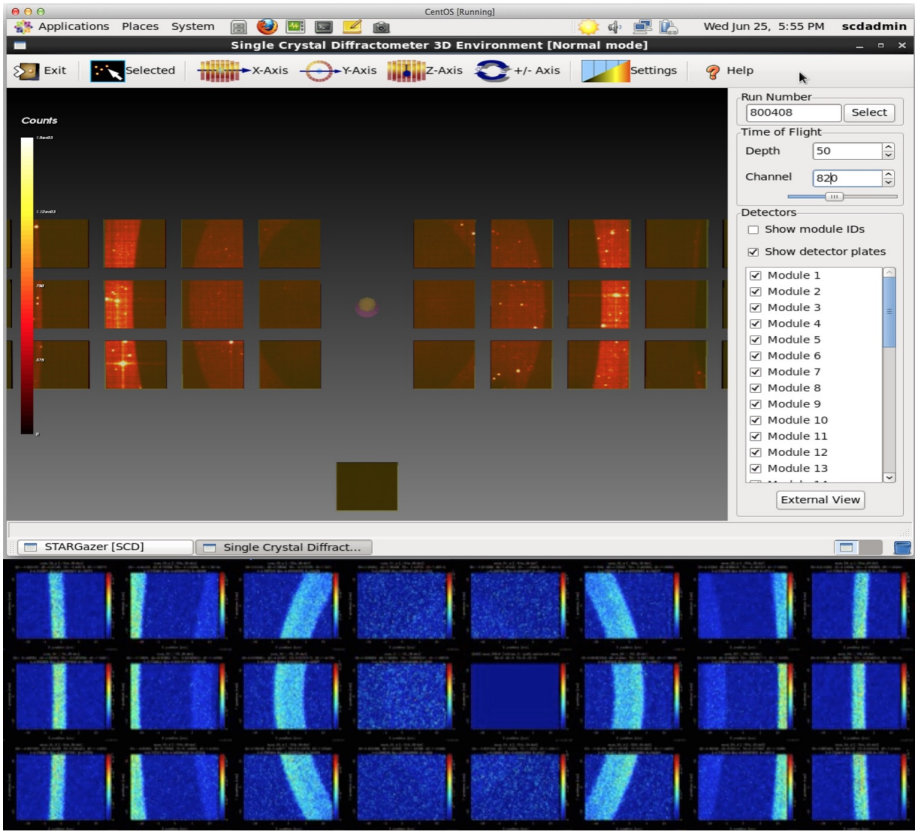

Figure 5.7: *Above:* at SENJU, both isolated diffraction spots and powder rings were recorded by the far-field detectors. *Right:* McStas simulations using a Fe powder sample confirmed that the observed rings were due to a sample region with a powder-like structure.

5.4 CHAPTER SUMMARY

The simulation software McStas was a valuable tool to explore the feasibility of *ToF 3DND* and to estimate the experimental time required to investigate a Fe sample. Test showed that the algorithms developed to analyse real data collected in transmission mode (see Ch. 6) could also be applied to data generated by the McStas simulations, returning a 3D reconstruction of the simulated sample. This opens a new realm of possibilities for simulated experiments: after being reconstructed, samples that were investigated using 3DND can be included in McStas simulations, and the generated data reconstructed using the same algorithms used to analyse real data. In this way, scientists will have the possibility to refine *a posteriori* the parameters used in an experiment.

6

Grain shape reconstruction

Contents

AT SENJU, we used an event-counting detector with high spatial and temporal resolution to collect data in transmission mode (see Ch. 4). This chapter presents how the shape and justaxposition of the grains in the sample can be reconstructed from transmission data. In Sec. 6.1 the data acquisition, pre-processing and processing steps are presented, with focus on the software solutions. As a sample, an iron rod was considered. To validate the developed algorithms, in Sec. 6.2 we *a)* compared a slice from the 3D reconstruction with the corresponding electron backscatter diffraction (EBSD) map, and *b)* applied the algorithms to reconstruct a Co-Ni-Ga sample, made of two large grains. Last, Sec. 6.3 describes how data were filtered before calculating the grain orientations from the transmission data, as will be described in 7.1.

6.1 FROM TRANSMISSION DATA TO 3D GRAIN SHAPES

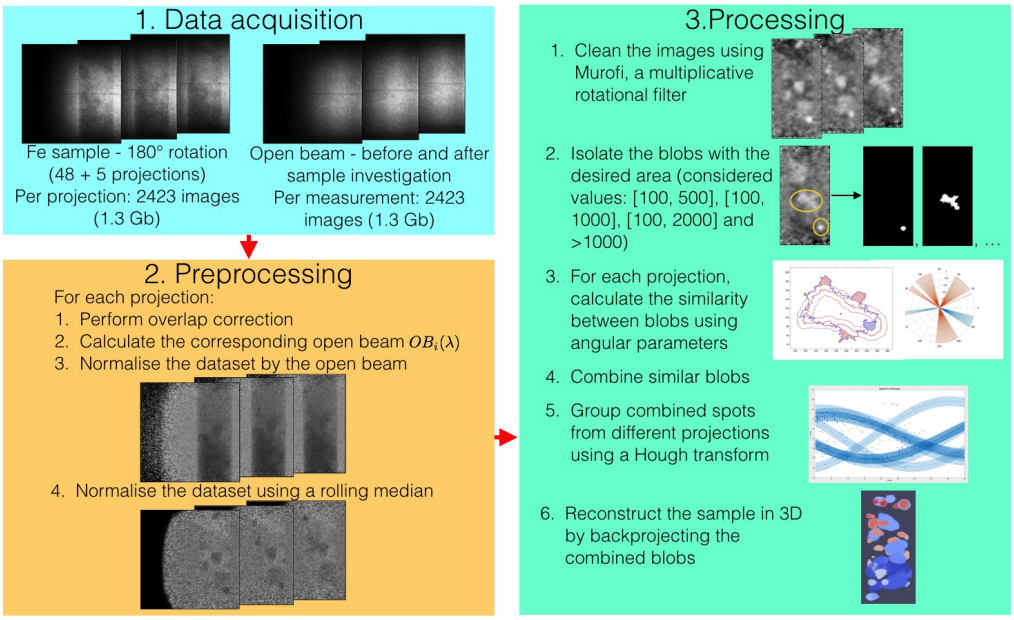

Figure 6.1: Overview of the steps in data acquisition (*1*) and analysis (divided in (*2*), pre-processing, and (*3*), processing), showing how the raw data was processed to reconstruct the 3D shape of the grains.

This section describes the procedure developed to analyse the transmission data collected at SENJU, J-PARC. At first, data were pre-processed to reduce the noise and improve the signal in the collected images. Data were then processed using algorithms developed to isolate the extinction spots and group together the spots relative to the same grain, recorded at different wavelengths and projections (see Fig. 6.2). A new rotational filter developed by S. Schmidt (DTU), Murofi, was used to segment the extinction spots. A flowchart of the data analysis recipe is sketched in Fig. 6.1.

6.1.1 DATA ACQUISITION

At SENJU, transmission data were collected using the following recipe:

1. Collect an "open beam" dataset, with no sample in. Acquisition time: about one hour (3200 sec to collect neutrons, plus about 400 sec to write the data).

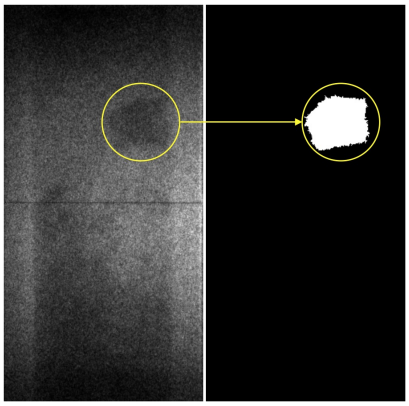

Figure 6.2: *Left:* typical raw image collected by the near-field detector mounted in transmission mode at SENJU. The circle shows an extinction spot. *Right:* extinction spot after the segmentation procedure.

2. Mount the sample and collect the transmission datasets at different projections, regularly distributed over 180°. For each projection, the acquisition time was the same as the open beam acquisition time.

3. Remove the sample and acquire an "open beam" dataset, using the same acquisition time used in 1. and 2.

To collect the diffraction and transmission data, the sample was rotated by 177° around the vertical axis, for a total of 54 projections: 49 projections in 3° step from 0° to 144°, and 5 projections in 6° step from 153° to 177°. At each projection 2423 frames were collected, each corresponding to a wavelength interval of $1.48{\cdot}10^{-3}$ Å, that is 12.8 μs in time-of-flight using Eq. 3.3. In total, the sample was imaged for more than two days. To take into account possible variations of the beam intensity over such time interval, for each projection the collected signal was divided by the relative open beam, calculated from the open beam datasets collected before and after studying the sample.

6.1.2 DATA PRE-PROCESSING

The frames acquired by the near-field detector were first processed using an *overlap correction algorithm*, described below and in [Tremsin et al., 2014], and then, for each projection, normalised by the corresponding open beam and using a rolling median (see Fig. 6.3).

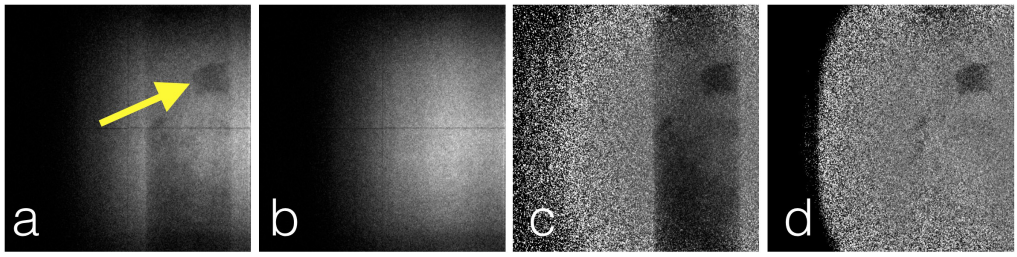

Figure 6.3: Typical images collected by the near-filed detector and pre-processing steps. *a*: Raw collected image, with the iron sample mounted. The arrow points an extinction spot. *b*: Open beam dataset, calculated for the same projection of *a*. *c*: Raw image after being normalised by the corresponding open beam (Eq. 6.1). *d*: *c* after being filtered using a rolling median (Eq. 6.2).

6.1.2.1 Overlap correction algorithm

The MCP detector used to collect data in transmission mode at SENJU is equipped with a Timepix readout [Tremsin et al., 2013]. When a sample is illuminated by many time-of-flight neutron pulses, a given pixel records i neutrons with ToF values $\{t_i\}_i$. The list of events is later divided in a number of time-of-flight intervals (2423 for the Fe sample, 2500 for the Co-Ni-Ga sample), each resulting in a separate image.

The Timepix readout used in the MCP detector can only register one event per pixel for each time interval (*shutter*) between two readouts. As a result, the measured time-of-flight spectra of the input flux is affected by distortions: neutrons arriving towards the end of an acquisition shutter have lower probability to be detected, as the relative pixel might be occupied by previous events [Tremsin et al., 2014]. Fig. 6.4 shows the distribution of the readout pauses among the frames returned by the MCP detector.

To overcome the one event per pixel count limitation, A. Tremsin and collaborators developed an algorithm that uses the periodic structure of the incoming time-of-flight beam to calculate the number of neutrons that the pixel would count if there wasn't a maximum of one event per pixel per shutter (see Fig. 6.5) [Tremsin et al., 2014]. As a first step of the data pre-processing, the collected images were corrected, frame by frame, using the overlap correction algorithm.

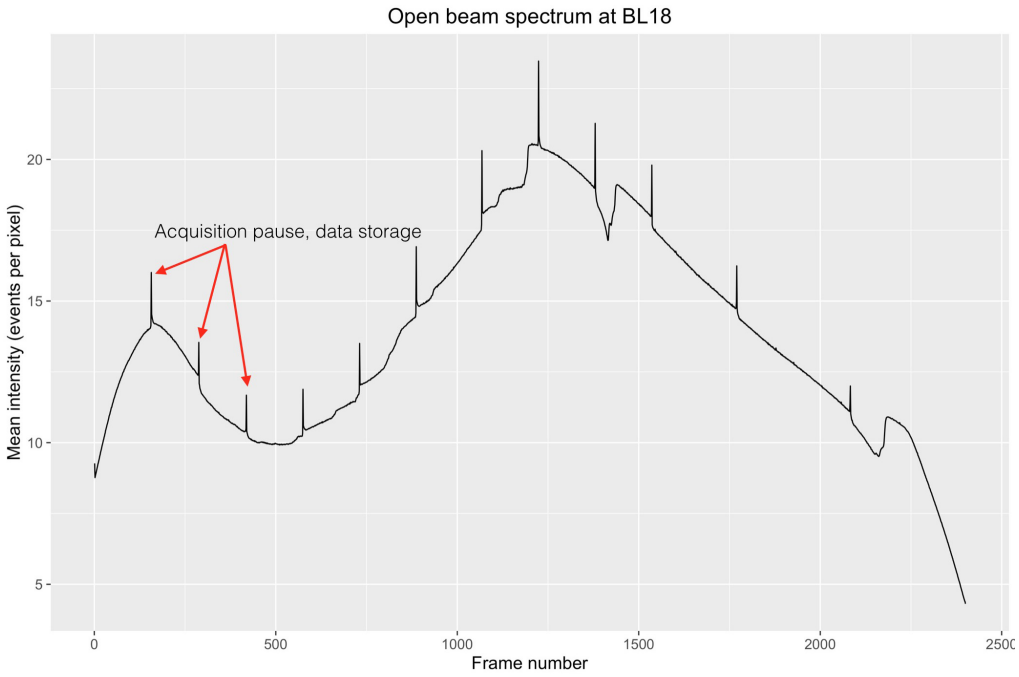

Figure 6.4: Open beam spectrum collected by the near-field detector used at SENJU, showing the total number of counts as a function of the frame number. Spikes in event counts correspond to data acquisition pauses for data storage.

6.1.2.2 Image normalisation

After traversing a sample of thickness L, a neutron beam of intensity $I_0(\lambda)$ is attenuated by an exponential factor, as described by the Beer-Lamber law:

$$I(\lambda) = I_0(\lambda)e^{-\int \mu(z)dz} \tag{1.1}$$

where $\mu(z)$ is the attenuation coefficient and $I(\lambda)$ is the detected intensity

To consider the contribution from the sample in collected signal, for each considered projection i we divided the collected dataset $I_i(\lambda)$ by the corresponding open beam, calculated using the formula

$$OB_i(\lambda) = OB_{Start}(\lambda) - \frac{OB_{Start}(\lambda) - OB_{End}(\lambda)}{\text{Number of projections}} \cdot i \tag{6.1}$$

where OB_{Start} and OB_{End} are the open beam datasets measured, respectively, before and after imaging the iron sample (the beam intensity decreased during the measurements). In this way, inhomogeneities of the detector and of the neutron beam profile were taken into account.

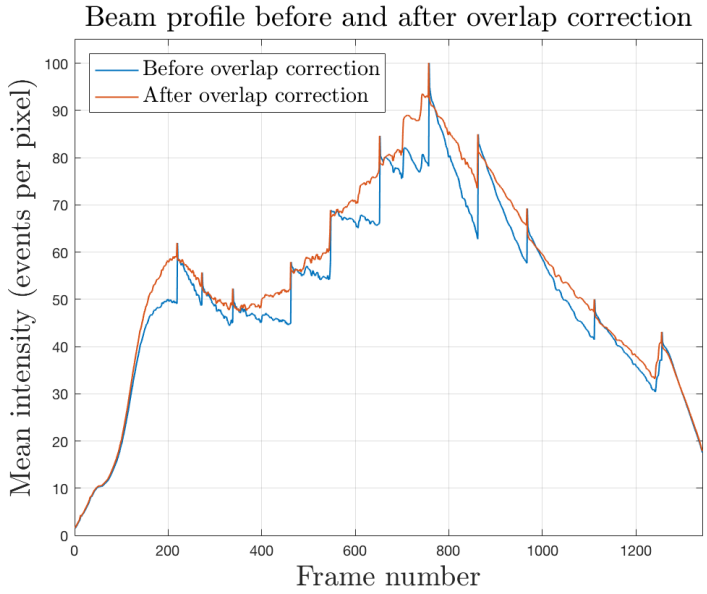

Figure 6.5: Beam profile collected at SENJU by the transmission detector during a test measurement in 2014. The MCP detector is equipped with a Timepix readout, which can only measure one event per pixel per shutter. To account for distortion introduced by this limitation, as a first pre-processing step the images collected at SENJU were processed with an overlap correction algorithm [Tremsin et al., 2014]. When applied, the overlap correction smooths the beam profile.

To reduce the noise and enhance the extinction spots, the images were processed using a rolling median with a window size of 41 frames. For each projection, after pre-processing the image dataset was thus

$$\widetilde{I}_i(\lambda) = \frac{I_i(\lambda)}{OB_i(\lambda) \cdot \text{median}[I(\lambda - n\Delta\lambda), \ldots, I(\lambda + n\Delta\lambda)]} \tag{6.2}$$

where $n = 20$ and $\Delta\lambda$ is the wavelength interval relative to a single frame. The value was chosen to match the maximum number (for the Fe sample) of consecutive frames where the same extinction spot was observed.

6.1.3 DATA PROCESSING

This section presents the methods we developed to *a)* locate extinction spots in the transmission data, *b)* group and combine spots relative to the same grain, and *c)* reconstruct 3D grain shapes.

6.1.3.1 Extinction spots detection

The starting point for reconstructing the 3D shape of the grains was to determine the shape of the extinction spots in the transmission images. To do so, we borrowed ideas from the field of computer vision, whose aim is to extract useful information from raw images [Liu et al., 2012]. Determining the shape of objects in an image is a typical *image segmentation* task[1]. For a quick overview of computer vision, see the information box below.

Even after pre-processing, segmenting the transmission images to locate the extinction spots was particularly challenging, because regions of the sample inside and outside an extinction spot had similar intensity profile and salt-and-pepper pattern, as shown in Fig. 6.6. On top of that, as a consequence of mosaicity (orientation spread within a crystal) the recorded intensity varies among the images collected for a given grain. Concluding, these are the characteristics required to segment extinction spots from the pre-processed data:

1. Ability to detect a noisy shape on a noisy background.
2. Sensitivity to small intensity variations.
3. Ability to detect extinction spots with different intensity values.
4. Ability to detect spots of different shapes and in different regions of the considered images.
5. The false detection rate should be kept as low as possible.
6. Computationally efficiency, since for each projection thousands of images must be processed.

Various segmentation techniques, ranging from simple thresholding (not satisfying requirements 1. and 2.) to more sophisticated techniques such as adaptive contouring (a.k.a. "snakes" algorithm, requiring *a-priori* information [Kass et al., 1988]) were tested with no satisfactory results. Different filters were tried before segmenting the images, with no success. It is possible that successful solutions are available but have not been properly implemented.

To efficiently segment the extinction spots, we developed a new segmentation technique basing on the **mu**ltiplicative **ro**tational **fi**lter Murofi, by S. Schmidt (DTU). The developed approach satisfies all the requirements listed above and consists of the following steps:

[1] In computer vision, image segmentation can be defined as the division of an image into parts that have a strong correlation with objects contained in the image [Sonka et al., 2014].

Computer vision

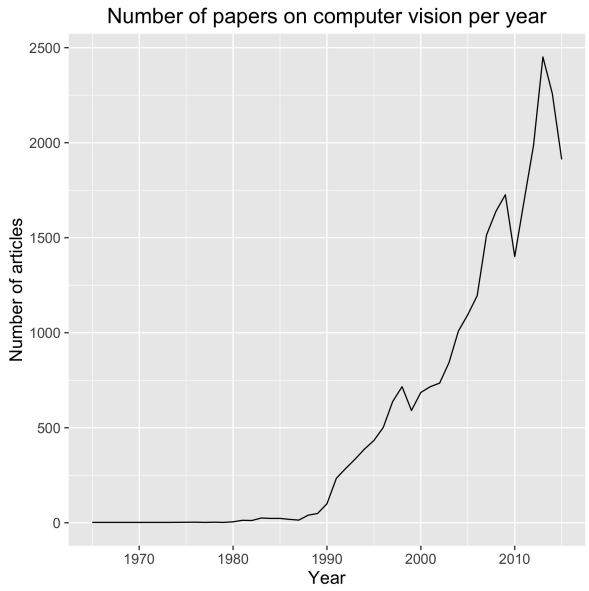

While humans and animals can subconciously determine the conditions of their environment (like illumination) and the properties of the objects around them (shape, color, ...), implementing the same task on computers is very challenging and error prone. And it is easy to underestimate the complexity of the challenges, as known by Marvin Minsky, one of the fathers of artificial intelligence: in 1966 he asked one of his undergraduate students at MIT, Gerald J. Sussman, to "*spend the summer linking a camera to a computer and getting the computer to describe what it saw*" [Boden, 2006]. We now know that the problem is much more complicated than that [Szeliski, 2010]. As shown in the graph above, in the last few decades computer vision rapidly developed as a research field. At present, computer vision has many industrial applications, including handwriting recognition, medical imaging, fingerprint recognition and biometrics, surveillance, and automotive safety (now evolving towards self-driving cars) [Szeliski, 2010, Google X,].
In the Figure: number of papers published per year under the topic "computer vision". Data from [Thompson Reuters,].

1. Filter the pre-processed images using Murofi;

2. Segment the filtered images using a threshold, to get binary images.

Basic morphologic operations were used to locate the shape of the extinction spots in the binary images.

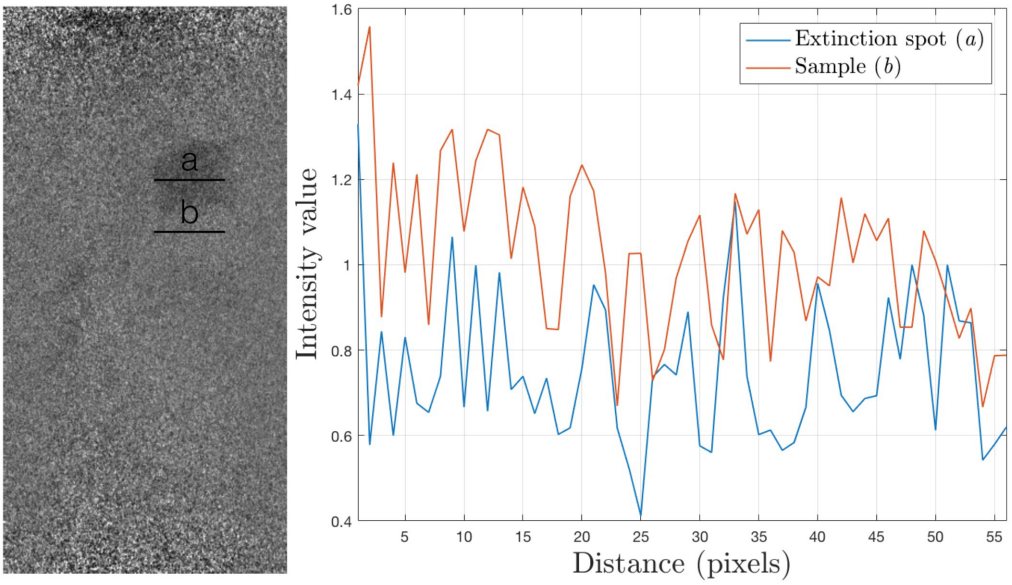

Figure 6.6: Intensity profile for the pixels across the diameter of an extinction spot (a) and outside it (b). The difficulty to isolate the extinction spots arises from the fact that both the intensity profile and the salt-and-pepper 2D distribution of the intensity values are similar.

6.1.3.2 The Murofi filter

To enhance the extinction spots in an image IM_0, Murofi works as follows: it rotates IM_0 by an angle $i \cdot \alpha$, smooths the rotated image row by row using a rolling interval, rotates the image back to the original position and multiplies it, pixel by pixel, by the initial image. The process is repeated, stepping by α degrees from 0° to 180°. In this way, the filtered image IM_f is given by

$$IM_f = IM_0 \cdot \prod_{i=1}^{N} (R_{i\cdot\alpha}^{-1}(R_{i\cdot\alpha} IM_0)^\dagger) \tag{6.3}$$

with $N = 180^\circ/\alpha$. R and $\dagger$ denote, respectively, the rotation matrix and the row-by-row smoothing performed in the rotated matrix before rotating it back. As an output, Murofi returns two datasets, shown in Fig. 6.8: a set of greyscale, filtered images and the corresponding set of binarised images, obtained by thresholding the greyscale images.

To the best of our knowledge, the approach used by Murofi has not been reported before. It can be applied to solve various challenging segmentation problems, such as counting the number of nanoparticles in an image or enhancing the contrast in a smarthone picture without using a-priori information (see

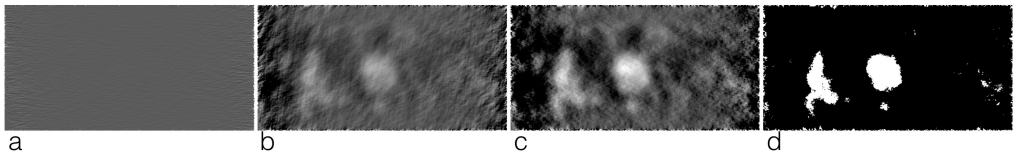

Figure 6.7: Murofi filters an image multiplying it by its copies, incrementally rotated by an angle α (in the shown case, $\alpha = 10^{\circ}$). Steps *a-d* show how Murofi was used to filter transmission images after pre-processing. *a-c*: filtered image after two, ten and 18 (final result) multiplications of the original image by its rotated copies. Bright regions correspond to extinction spots. *d*: binarised image, obtained by thresholding *c*.

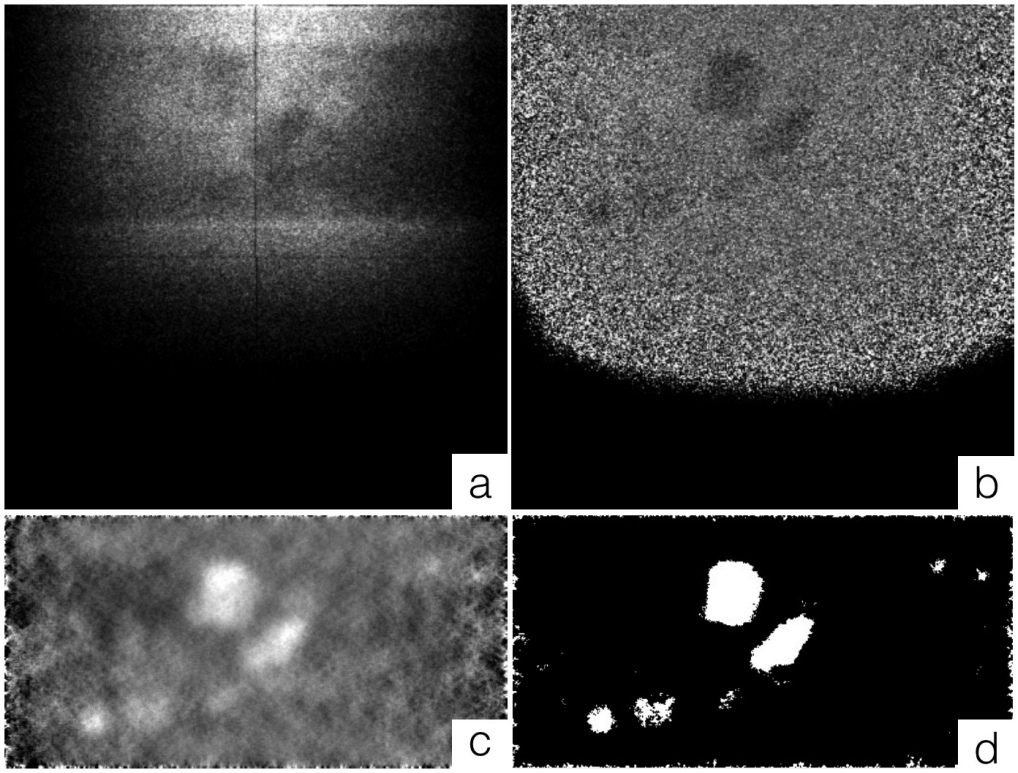

Figure 6.8: The Murofi filter was developed to enable segmenting extinction spots in the images collected in transmission mode at SENJU. *a*: raw image collected imaging the Fe sample. *b*: *a* after pre-processing. *c*: *b* after filtering using Murofi. *d*: *c* binarized using a threshold value. In *c* and *d*, only the sample region is shown.

Fig. 6.6). The philosophy behind Murofi is similar to that of *steerable filters*, a family of computer vision algorithms that process images by applying many versions of the same filter, each of which differ by some small angular rotation [Freeman and Adelson, 1991].

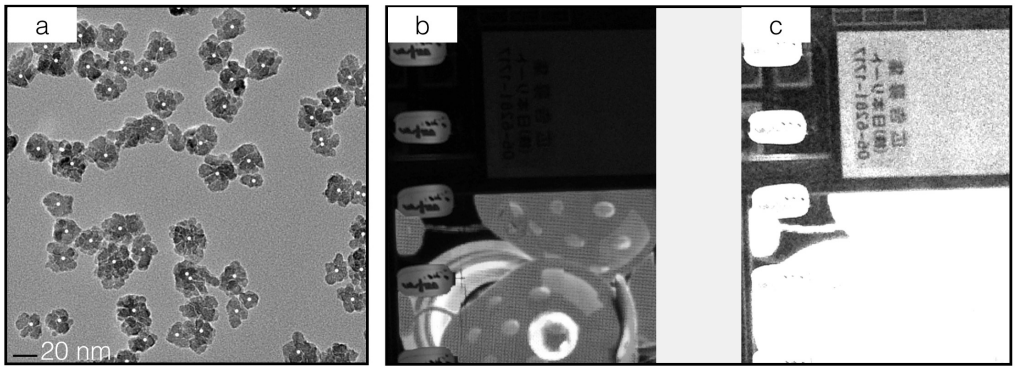

Figure 6.9: Murofi was developed to segment neutron imaging data whose change from frame to frame and are hardly distinguishable from the background. Murofi uses a general approach that can be applied to many problems involving image segmentation, such as counting the number of $\gamma - Fe_2O_3$ nanoparticles (nanoflowers) [Zhong et al., 2006] in a transmission electron microscopy (TEM) (*a*), or to sharpen a phone picture (*b*: raw image, *c*: image processed using Murofi). The accuracy of Murofi to count nanoparticles in the considered TEM image is better than what returned by the routinely used algorithm, which is specifically designed to measure sperical particles and has difficulties dealing with more complex structures such as nanoflowers [Sperling, 2009, Varón, 2016]. Raw images are courtesy of M. Varón and M. Zamboni.

6.1.3.3 Extinction spots localization

After being filtered with Murofi and binarised, the transmission images were processed to isolate the extinction spots. This was done using the built-in MATLAB® function `bwlabel`, which locates the connected components in a 2D image and labels them [MATLAB®, 2015, MATLAB®,]. The approach consisted in locating the connected components in the binarized images returned by Murofi, select those with an area in the desired range and save each connected component ("blob") in a separate image. Alg. 1 illustrates the process in pseudocode.

Algorithm 1 Blobs selection in filtered images

```
to limit the noise, clean the image using a frame
label the blobs in the image using bwlabel or a similar function
for each blob do
    if the blob area is in the desired range then
        save the blob in a dedicated image
    end if
end for
```

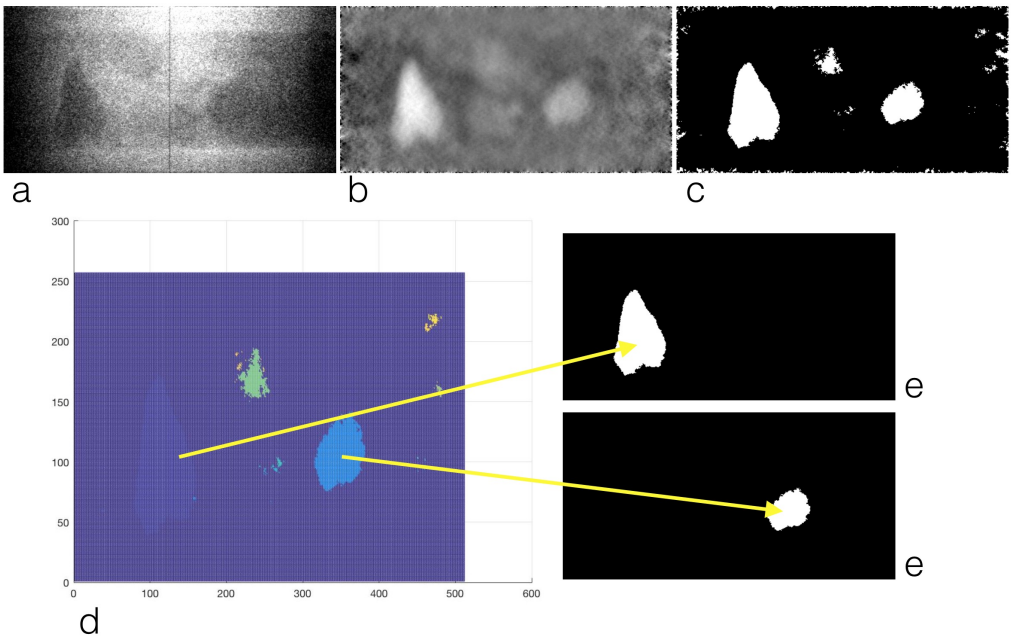

Figure 6.10: Procedure used to segment the extinction spots in the images collected by the near-field detector. The raw image *a* was filtered using Murofi (*b*; binarized version in *c*) and then processed using the `bwlabel` function of MATLAB® to isolate the different blobs, each corresponding to a different extinction spot [MATLAB®, 2015, MATLAB®,]. Different bobs were saved in different images (*e*).

For a given projection, the spots relative to a given grain were observed in up to 20 consecutive frames, with shapes that were sometimes very different. The spreading of the extinction spots is due to the mosaicity of the grains and increases the probability of overlaps with spots from other grains. This effect makes small grains harder to reconstruct than big ones, because their extinction spots are more easily covered by others. To be able to find both small and big grains, we considered four different intervals of the blobs area (A): A $\in$ $[100, 500]$ pixels, A $\in$ $[100, 1000]$ pixels, A $\in$ $[100, 2000]$ pixels and A $>$1000 pixels. The reconstruction of the grain shape in 3D was performed separately for each interval of the extinction spots area, and then the four reconstruction were combined in a single one as described in 6.1.3.6.

6.1.3.4 Morphological operations

After segmenting the extinction spots, the remaining data analysis steps focus on finding which spots beloing to the same grain. This is done by comparing the shapes of the different spots and measuring their similarity. These oper-

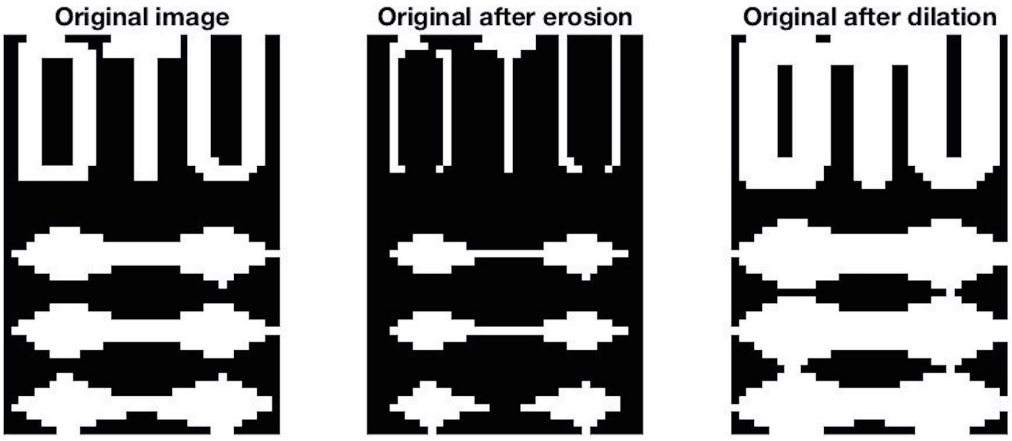

Figure 6.11: Erosion and dilation are two basic morphologic operations used to process the shapes contained in binary images. Erosion turns from ON to OFF (respectively white and black pixels in the image) ON pixels that are in contact with the background. Dilation turns to ON background pixels that are in contact with ON pixels.

ations were done combining different *morphological procedures*: operations, developed by the field of mathematical morphology, used to process binary images [Russ, 2015]. For a formal introduction, see [Sonka et al., 2014]. Intuitively, morphological operations add or subtract pixels from a binary image following given rules, which depend on the distribution of the pixels in the original image [Russ, 2015].

The two basic morphological operations are *erosion* and *dilation*, respectively consisting in turning OFF (assign value 0) pixels that are originally ON (have value 1) and vice versa. In its simplest incarnation, erosion removes (swithing it from ON to OFF) any pixel touching the background, by default set to OFF. Dilation is the complementary operation: it adds (swithing it from OFF to ON) any pixel touching the background. In the extinction spots images OFF pixels (background) are set to 0, and ON pixels are set to 1[2].

Two other morphological operations, *opening* and *closing*, are a combination of erosion and dilation. An opening consists of an erosion followed by a dilation, and a closing consists of a dilation followed by an erosion.

In the next Section, we will describe how morphological operations, combined with a new approach, were used to measure the difference between extinction spots and group those relative to the same grain.

[2]In mathematical morphology usually it's the other way around.

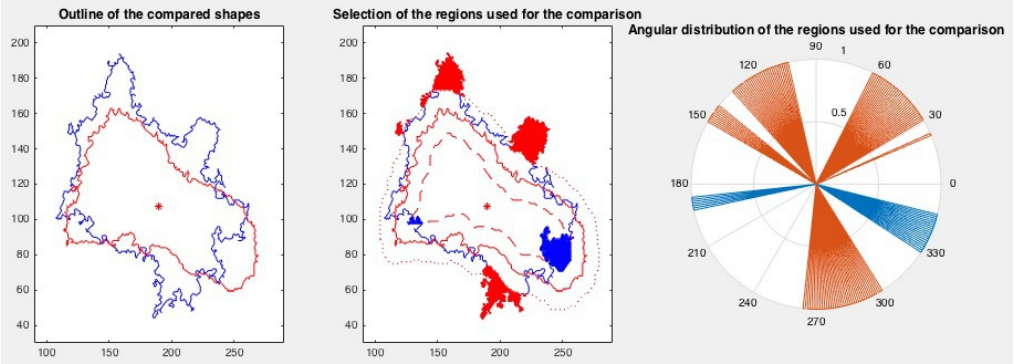

Figure 6.12: Sketch of the algorithm developed to compare the shapes of different extinction spots, to check if they are relative to the same grain. *Left:* perimeter of the two extinction spots A and B (area(A)>area(B)), translated so to have the same centre of mass; *centre:* regions used to measure the shape similarity: part of eroded B that is outside A (blue filled region), and part of A outside dilated B (red filled region); *right*: angular distribution of the regions previously located. Using threshold values, the developed algorithm decides whether two spots are similar or not: do they differ over a small or large angular region?

6.1.3.5 Grain sorting

To group the extinction spots relative to a given grain, we developed an algorithm that measures, based on angular parameters, how similar two shapes are. To compare two spots A and B (A being the one with the greater area of the two), we superimposed their centres of mass and measured the angular distribution of the pixels of B that are inside the eroded perimeter of A, and of the pixels of A that are outside the dilated perimeter of B (see Fig. 6.12). If the angular regions where the spots differ are smaller than the chosen threshold values, the spots are considered similar and thus relative to the same grain.

The opening and closing operations were implemented using the MATLAB® functions `imopen` and `imclose`. In both cases, the shapes of the blobs were processed using as a structuring element a circle with radius $r = \sqrt{\text{Area blob}/3} * 0.2$. By varying the structuring parameter with the size of the considered blob, it was possible to efficiently smooth blobs with different sizes, minimizing the loss of features.

For each projection, similar blobs were marked as members of the same group and combined. In the combined image, a pixel is marked as 1 if it has value 1 in at least half of the relative grouped images, containing blobs with similar shapes. For each group of extinction spots, the projection number and the image number of each element were stored as a list.

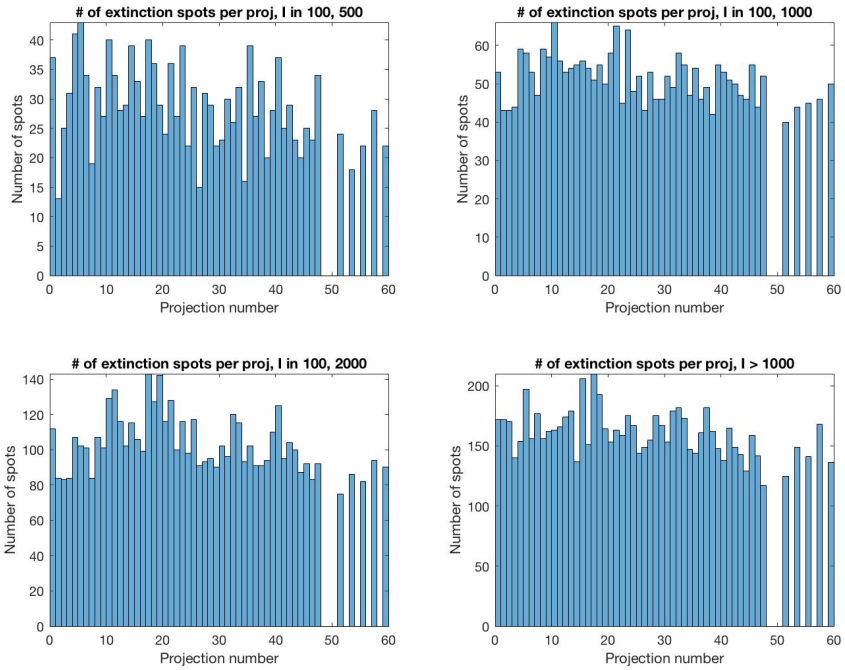

Figure 6.13: Number of combined extinction spots per projection for the four extinction spots area (A) intervals considered: $A \in [100, 500]$ pixels, $A \in [100, 1000]$ pixels, $A \in [100, 2000]$ pixels and $A > 1000$ pixels.

The number of combined extinction spots varied from projection to projection, as shown in Fig. 6.13. To merge duplicates, for each combined exctinction spot the procedure outlined in Alg. 2 was followed. In short, a circle was built on the centre of mass of each combined blob; in case other centres of mass were found within the circle, the respective blobs were combined as usual: in the final image, a pixel had value 1 if it was 1 in at least half of the grouped images. Fig. 6.14 illustrates how the procedure outlined in Alg. 2 cleans the distribution of the centre of mass values for the combined extinction spots.

In the presented approach, the 3D shape of the grains composing the considered sample was reconstructed using a back projection algorithm, that takes as input the projections of the grains at different angles (see Fig. 6.15). For a given grain, as the best estimate of its projected shape we considered the combination of the relative extinction spots.

Algorithm 2 Goup combined blobs to avoid duplicates

```
for each combined blob do
    build a circle centered in its centre of mass
    search for other centre of mass values within the circle
    if a centre of mass value is found in the circle then
        if the area of the smaller blob is > 0.5· area of the bigger blob then
            the two blobs are combined
        end if
    end if
end for
```

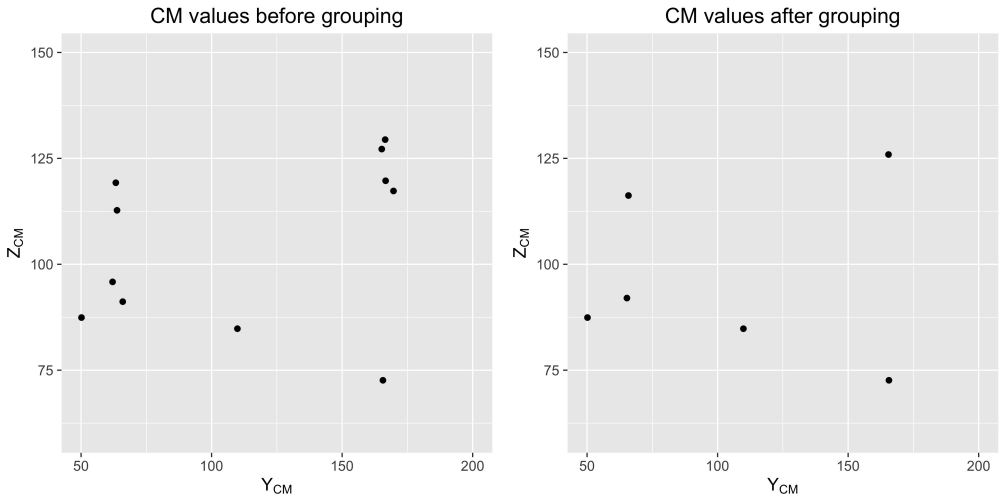

Figure 6.14: Distribution, on the transmission detector plane, of the centres of mass for the combined extinction spots before and after the procedure described in Alg. 2. Values relative to projection number two.

The Hough transform. Let us consider a given grain within a polycrystalline sample. When the sample, illuminated by a neutron beam, is rotated around its vertical axis, the centre of mass of the extinction spots relative to the grain (which, roughly, corresponds to the projection of the centre of mass of the grain) moves along horizontal lines on the detector plane $y_d z_d$. These straight lines correspond to sinusoids in the $y_d z_d \omega$-space (see Fig. 6.16).

In the collected data, spots relative to the same grain have centre of mass distribute around the same soinoid in the $y_d z_d \omega$-space, and thus around the same horizontal line in the $y_d z_d$-plane, as shown respectively in Fig. 6.17 **b** and **c**.

To divide extinction spots in groups, each corresponding to a different grain,

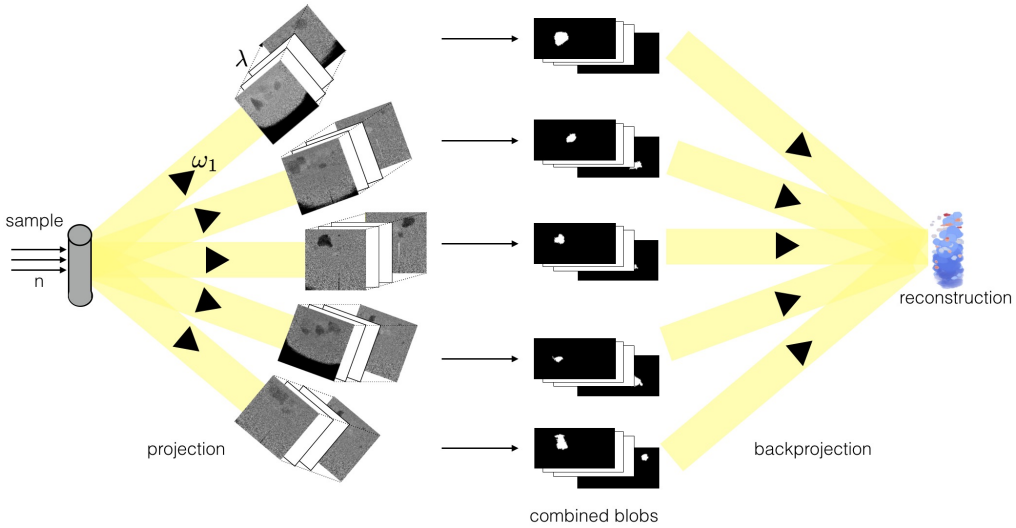

Figure 6.15: Projection and backprojection procedure in ToF 3DND. *Left*: for each rotation angle the time-of-flight beam projects to the detector plane the extinction spots relative to different grains at different wavelengths. The images relative to each angle were then filtered and treated, to combine extinction spots relative to the same grain. The 3D shapes of the grains were obtained by backprojecting (*right*) the relative combined extinction spots from the different angles.

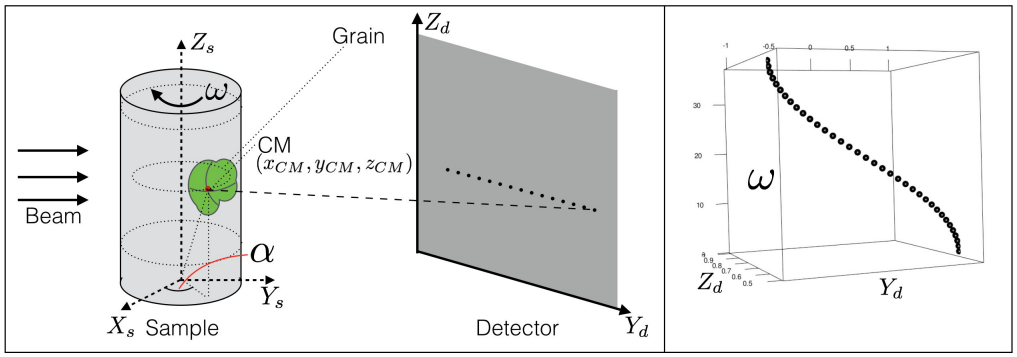

Figure 6.16: *Left:* let us consider a polycrystalline sample, illuminated by a neutron beam. For a given grain with centre of mass in (x_{CM}, y_{CM}, z_{CM}), the centre of mass of the relative extinction spots trace a horizontal line on the plane of the transmission detector. In the $y_d z_d \omega$-space, the line is a sinusoid lying on a $y_d \omega$-plane (*right*). ω represents the angles where the projections have been recorded. The coordinate systems of the sample and of the detector are (x_s, y_s, z_s) and (y_d, z_d).

we considered the distribution of their centres of mass in the $y_d z_d \omega$-space: in the $y_d z_d$-plane, the distribution of points is crowded and hard to fit (see Fig.

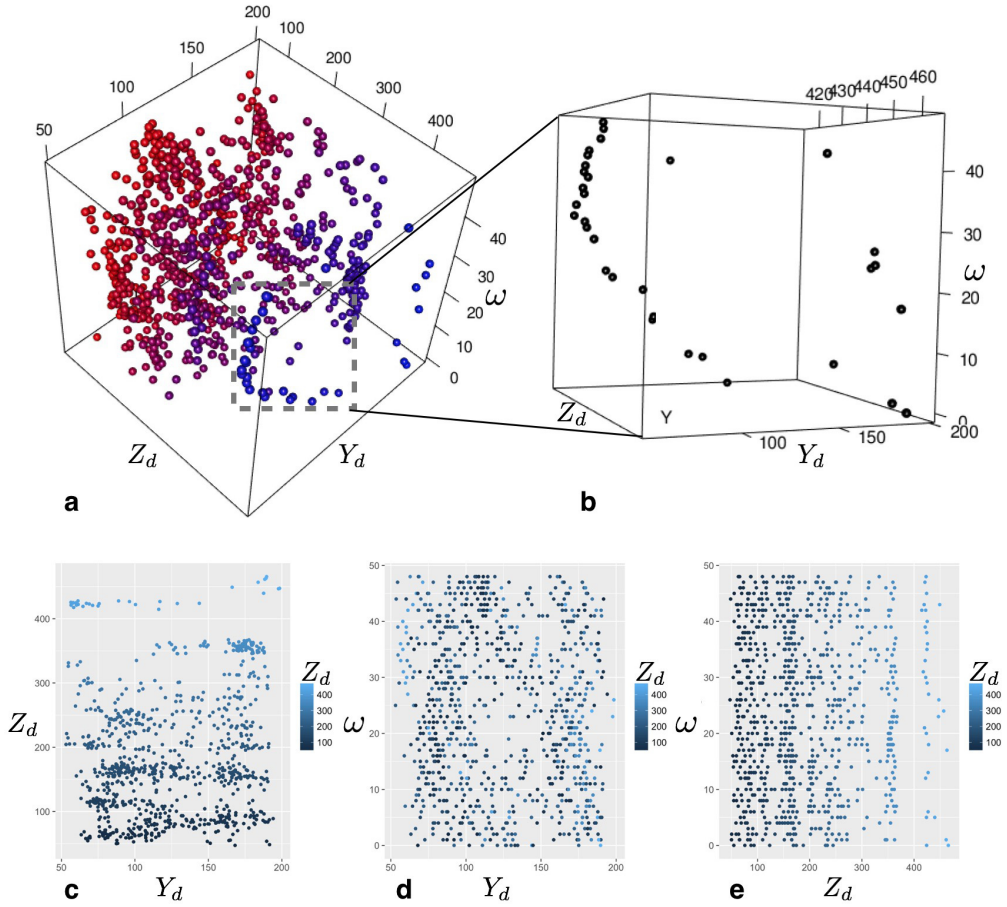

Figure 6.17: Distribution of the centres of mass of the combined extinction spots for the first 48 considered angles. *a*: distribution of the centres of mass in the $y_d z_d \omega$-space. y_d and z_d are the coordinates of the centre of mass of the combined extinction spots on the detector plane, and ω is the angle where the extinction spots were collected. *b*: points relative to a given grain are distributed around a sinusoid on a $y_d\omega$-plane. *c*, *d* and *e* show the distribution of points on the $y_d z_d$-, $y_d\omega$- and $z_d\omega$-plane, respectively.

6.17 **c**). The grouping was done by sweeping the Z_d axis using a rolling window (see Fig. 6.18) and locating, for each interval, the different sinusoids in the $y_d\omega$-plane, obtained by assigning the same z_d value to all points. The rolling window was used to avoid missing fitting curves: in this way, the points distribution gradually changes from interval to interval. The algorithm is presented in detail in Alg. 3.

The sinusoidal fitting curves were calculated using the *Hough transform*, a tool to detect shapes that is particularly efficient in presence of noise [Hough,

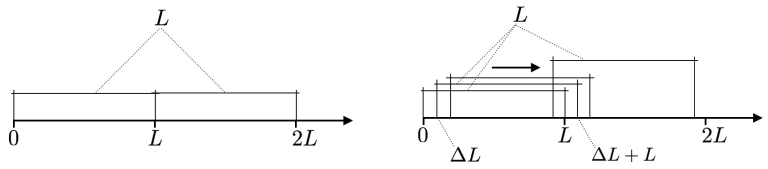

Figure 6.18: To find the curves fitting the points distribution in the $x_d y_d \omega$-space, the Z_d axis was divided into intervals using a rolling window. *Left*: an axis is divided into intervals of length L, each starting at $\Delta L = n \cdot L$. *Right*: an axis is divided into intervals using a rolling window of length L, starting at intervals ΔL.

Algorithm 3 Grouping of the combined extinction spots

```
consider the distribution of points in the y_d z_d ω-space
make a rolling window running along the Z_d axis
for each rolling interval do
    consider the distribution of centre of mass values on the y_d ω-plane
    fit the points distribution using sinusoids
    for each sinusoid do
        built a band around the curve
        mark the points that are in the band
    end for
end for
```

1962, Haidekker, 2011]. Originally, the Hough transform was developed to detect the trajectories recorded by bubble chamber detectors [Hough, 1959].

The idea behind the Hough transform is to parametrize the space where data are represented and transform the points composing the shape of interest to the space of the parameters [Haidekker, 2011]. For example, a line described by the equation

$$y = m \cdot x + n \tag{6.4}$$

m being the slope of the line and n the intercept on the Y-axis, can be represented as a point in the mn-plane. A point (x,y) in the xy-plane corresponds a set of (m,n) values satisfying Eq. 6.4, which can be rewritten as a line equation[3] in the mn-space, also called *parametric space*:

$$m = \frac{y}{x} - \frac{1}{x}n \tag{6.5}$$

[3]The case is presented only to illustrate the Hough transform and is mathematically inconsistent: for vertical lines, Eq. 6.5 is undefined in the parametric space.

as illustrated in Fig. 6.19.

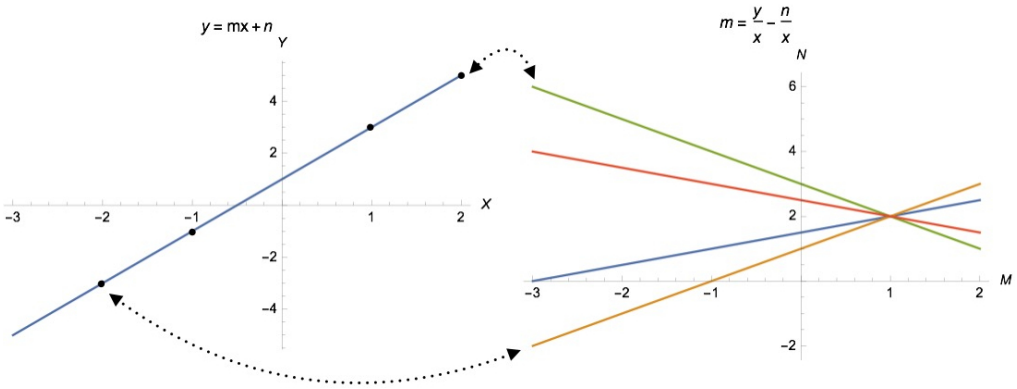

Figure 6.19: The Hough transform is a powerful tool for detecting shapes in noisy images. It transforms the points composing a shape into a curve in the relative parameter space. In the figure above, the points along a line of equation $y = m \cdot x + n$ are transformed into a system of lines of equation $m = \frac{y}{x} - \frac{1}{x} \cdot n$, each passing through the point (m,n) in the mn-space.

In the mn-space, all lines corresponding to points along $y = m \cdot x + n$ meet in one point (m,n). To detect the point, a so-called *voting scheme* is used, employing the following procedure:

1. Divide the region of the mn-space around (m,n) in bins, each with intensity set at 0;
2. Each time a line passes through a bin, the bin intensity is increased by 1;
3. The bin containing the point (m,n) is the one with the higher intensity. In case there are multiple bins with maximum intensity value, the bin containing (m,n) is their centre of mass.

The procedure is described in pseudocode in 4.

Calculation of the fitting function. In the $y_d z_d \omega$-space, the centres of mass of the combined extinction spots relative to the same grain are distributed around a sinusoidal.

For a given grain, the line drawn on the detector plane $y_d z_d$ by the relative extinction spots is, in first approximation, the same that is described by the projection of the centre of mass of the grain, with coordinates (x_{CM}, y_{CM}, z_{CM}), as the sample is rotated around its vertical rotation axis.

Algorithm 4 Voting system to detect accumulation points in the parameter space

```
divide the parameter space into bins
for each line do
    for each bin do
        if the lines passes by the bin then
            add 1 to the vote counter of the bin
        end if
    end for
end for
find bins with a number of votes higher than a given threshold
find the centre of mass of each cluster of bins
```

For a given grain with centre of mass $\mathbf{r_0} = \begin{pmatrix} x_{CM} \\ y_{CM} \\ z_{CM} \end{pmatrix}$ in the sample reference system, the centre of mass $\mathbf{r_d} = \begin{pmatrix} x_d \\ y_d \\ z_d \end{pmatrix}$ in the detector reference system is given by

$$\mathbf{r_d} = \Omega \mathbf{r_0} \tag{6.6}$$

where Ω is a rotation matrix defined as

$$\Omega = \begin{pmatrix} \cos\omega & \sin\omega & 0 \\ -\sin\omega & \cos\omega & 0 \\ 0 & 0 & 1 \end{pmatrix} \tag{6.7}$$

The curve described on the detector surface by the centre of mass of the grain is defined by the equations (see Fig. 6.16)

$$\begin{aligned} y_d &= x_{CM}\cos\omega + y_{CM}\sin\omega = R\cdot\cos(\omega+\alpha) \\ z_d &= z_{CM} \end{aligned} \tag{6.8}$$

with $R = \sqrt{x_{CM}^2 + y_{CM}^2}$. ω is the angle where the considered projection has been collected, and α the angle describing the position of the centre of mass of the grain in polar coordinates in the sample reference system (see Fig. 6.16):

$$(x_{CM}, y_{CM})_{cartesian} \rightarrow (R, \alpha)_{polar} \tag{6.9}$$

For each rolling window along the Z_d axis, the equation of the curves fitting the points distribution was calculated using the following procedure:

1. In the parametric space $R\alpha$, plot the curves with equation

$$R = \frac{y_d}{\cos(\omega + \alpha)}; \tag{6.10}$$

obtained from Eq. 6.8;

2. Following Alg. 4, find the nodes of the plotted curves, each with coordinates (α_i, R_i);

3. For each node i calculate, using Eq. 6.8, from the parameters (α_i, R_i) the formula of the relative fitting curve in the $y_d\omega$-space.

The fitting procedure is illustrated in Fig. 6.20.

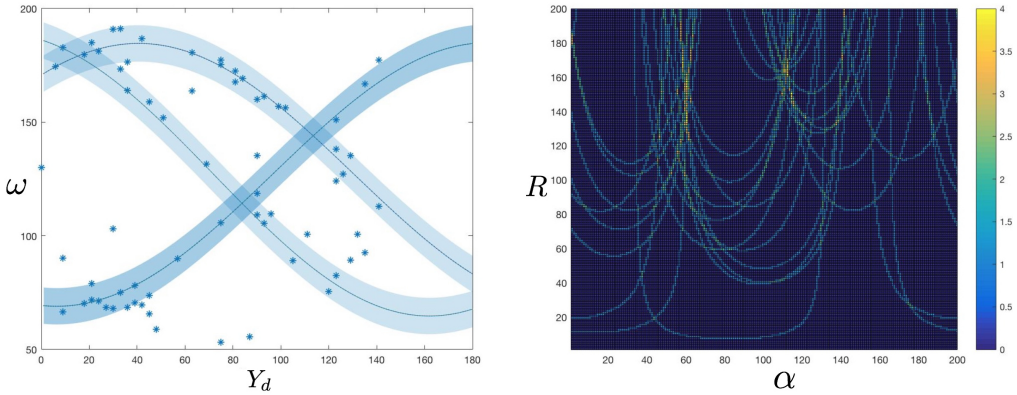

Figure 6.20: The Hough transform was used to group combined extinction spots relative to the same grain. *Left:* distribution of centre of mass values in one of the considered intervals along the Z_d-axis and calculated fitting curves, returned by the Hough transform. Interval centered at 200; data relative to the first 48 projection angles. *Right:* corresponding parameters space αR. Each family of αR-curves, relative to a sinusoid in the $y_d\omega$-space, meets in one point. A colorscale is used to illustrate the voting system employed to detect the nodes located by each family of curves.

6.1.3.6 Reconstruction

The Fe sample investigated at SENJU contained grains of different size; the diameter of those that could be imaged by the MCP detector ranged from a few hundred microns to more than a millimetre. To detect both small and big grains, extinction spots were divided in four size ranges and separately processed as described above. In detail, the four different intervals of the extinction spots area (A) were: A $\in [100, 500]$ pixels, A $\in [100, 1000]$ pixels, A $\in [100, 2000]$

pixels and A >1000 pixels. The four intervals partially overlap to avoid missing grains. Dividing the extinction spots in groups was necessary to avoid losing information on the smaller grains.

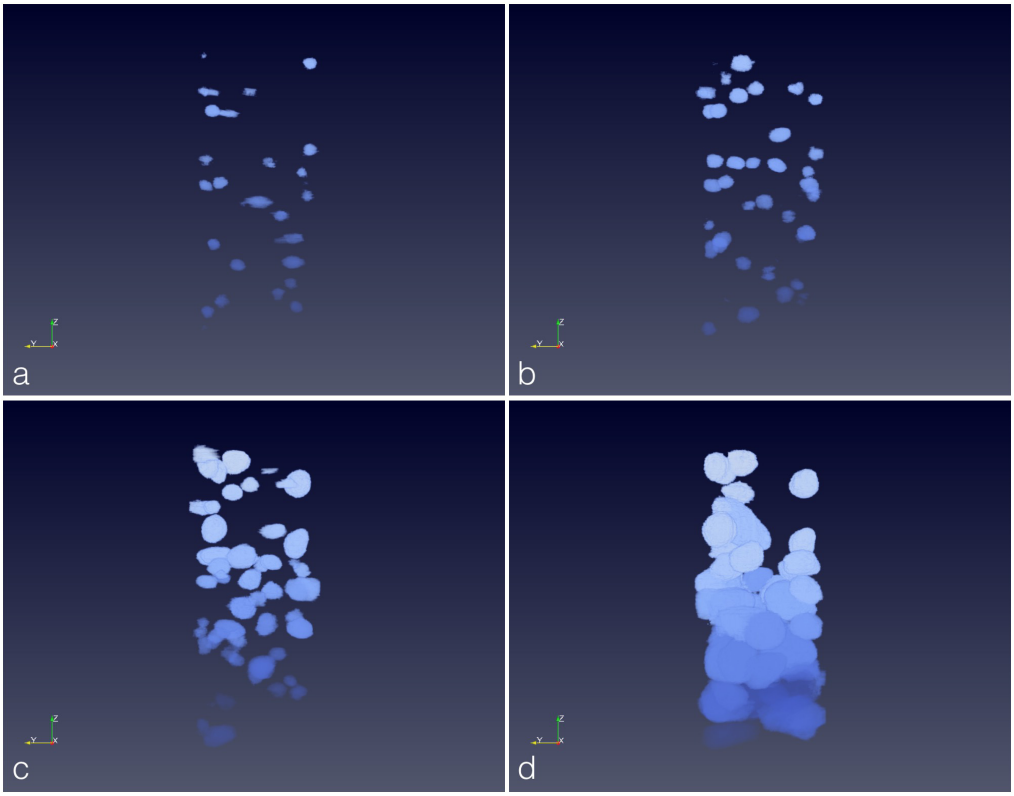

Figure 6.21: The shape of the grains within the Fe sample were reconstructed by back-projecting the relative extinction spots, combined as described in Sec. 6.1.3. Four different reconstructions were performed, respectively combining spots with area in the following intervals: A $\in [100, 500]$ pixels (*a* in the Figure above, 36 grains); A $\in [100, 1000]$ pixels (*b*, 43 grains); A $\in [100, 2000]$ pixels (*c*, 60 grains) and A >1000 pixels (*d*, 63 grains). Different grains are plotted in different colours.

For each area interval, a 3D sample reconstruction was obtained by back-projecting the corresponding combined extinction spots into a matrix consisting of $200 \times 200 \times 500$ voxels[4], as illustrated in Fig. 6.15. In this way, four reconstructions were obtained, with grains of increasing size, as shown in Fig. 6.21. The partial reconstructions were combined in the final one using a Matryoshka-like approach: if a grain was contained by a bigger one, it was considered part of it (see Fig. 6.22). If two grains, returned from different reconstructions,

[4]Each voxel is a cube of $50 \times 50 \times 50$ μm^3.

compenetrated each other, they were considered as a single grain if the centre of mass of one felt into the volume of the other (see Fig. 6.23). The final reconstruction, shown in Fig. 6.24, consists of 108 different grains, with volume ranging from 119 to $4.7 \cdot 10^5$ voxels. Nine grains with volume smaller than 110 voxels, which corresponds to that of a sphere with radius three voxels, were discarded as possibly unphysical. The centres of mass of the reconstructed grains are shown in Fig. 6.25.

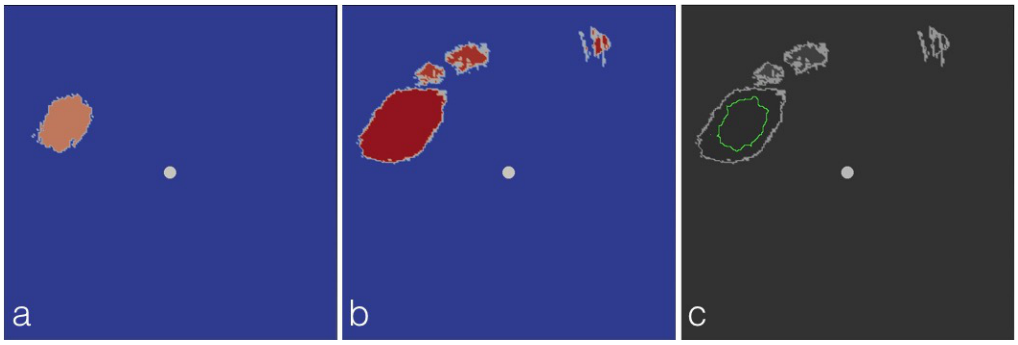

Figure 6.22: The four partial reconstructions, relative to extinction spots with different area, were combined using a Matryoshka-like approach: if a grain is contained in a bigger one, it is considered part of it. *a*: XY slice from the $I \in [100, 1000]$ pixels reconstruction; *b*: XY slice from the $I \in [100, 2000]$ pixels reconstruction. *c*: outline of the grain in *a* (in yellow), overlapped over *b*. In the final reconstruction, the grain in *a* is considered part of the one from *b* containing it.

In cubic microns, the grains volumes range between $1.49 \cdot 10^7$ and $5.91 \cdot 10^{10}$ μm^3, corresponding to a sphere with radius 150 μm and 2.4 mm, respectively. Fig. 6.26 shows the distribution of the grains volume in voxels and Tab. 6.1 shows the number of grains at different steps of the data analysis.

Dataset	Number of grains
Before centre of mass check	164
After centre of mass check	117
Volume $>$ 110 voxels	108

Table 6.1: Number of grains in the final reconstruction of the Fe at different steps of the data analysis. The centre of mass check consists in assigning to a grain the label of its centre of mass. The procedure was used to label together different volumes relative to the same grain.

To distinguish the various groups of extinction spots, which are expected to

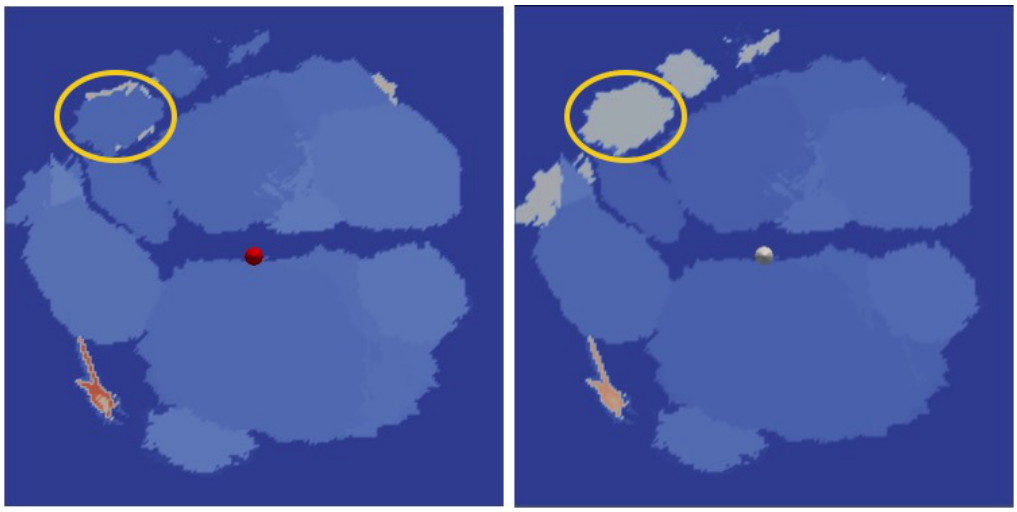

Figure 6.23: In the final 3D reconstruction of the Fe sample, different grains were labelled with different tags. In case the centre of mass of one grain felt into the volume of another (*left*), they were considered as a single grain (*right*).

correspond to different grains, labels were used, with each label corresponding to a different grain. A voxel was marked with a given label if, in the back-projecting procedure, at least half of the extinction spots in the relative group had pixels that were back-traced to it. In case a voxel had multiple labels, the one relative to more back-projected extinction spots was assigned.

6.2 PROCEDURE VALIDATION

To validate the shape reconstruction algorithms, the obtained grain map for the Fe sample was compared with what returned by a surface microscopy technique. Moreover, the algorithms were used to reconstruct a shape memory alloy sample, consisting of two cubic grains.

6.2.1 COMPARISON WITH ELECTRON BACKSCATTERING DIFFRACTION

After being analysed at SENJU, the Fe sample was sliced in four (longitudinally and radially). The plane surfaces were polished and imaged using electron backscatter diffraction (EBSD), a technique employing electrons to study shape and orientation of the grains on a sample surface [Schwartz et al., 2009]. The sample surface was investigated in 50 microns steps.

To test the validity of the reconstruction algorithm, the outlines of the grains

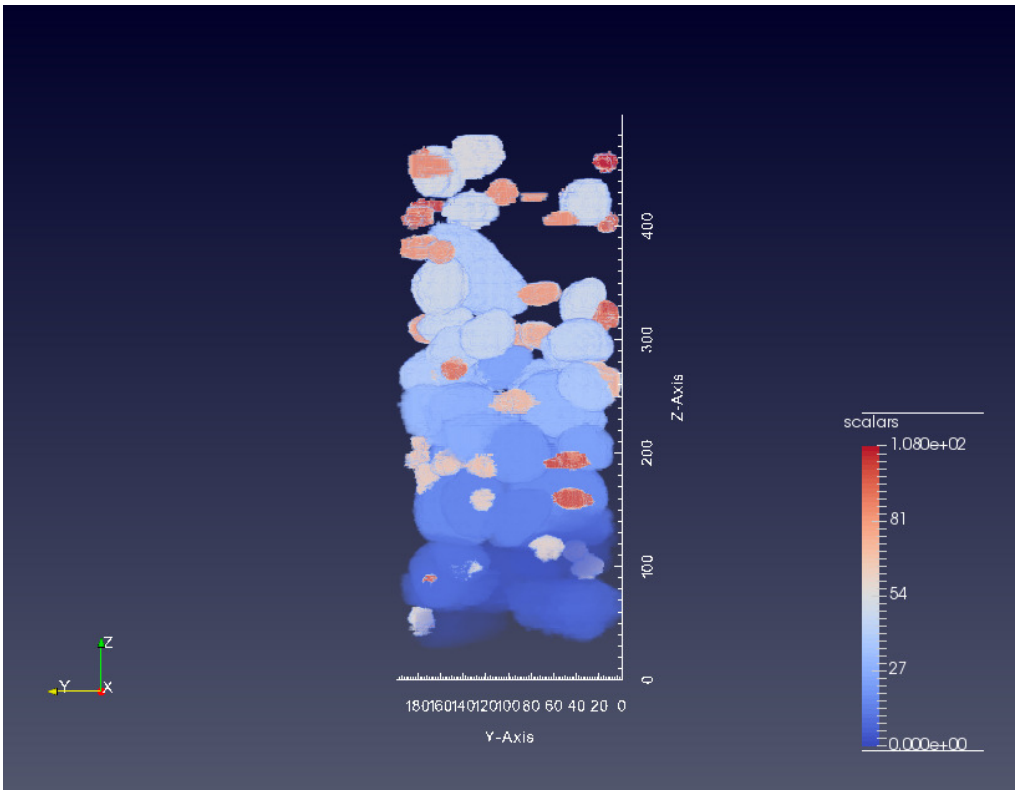

Figure 6.24: The final 3D grain map of the Fe sample combines the four partial reconstructions obtained for extinction spots with area A $\in [100, 500]$ pixels, A $\in [100, 1000]$ pixels, A $\in [100, 2000]$ pixels and A $>$1000 pixels. The final reconstruction consists of 108 individual grains, each represented in a different color. The grain numbering is the same in Fig. 6.24 and Fig. 6.26. Empty regions are probably occupied by small (down to powder-like) grains.

in a section of the 3D sample reconstruction were compared with the shapes returned by the EBSD scan. This was done by selecting a vertical slice of the sample reconstruction, locating the perimeters of the grains using the MATLAB® function `bwlabel` [MATLAB®, 2015,MATLAB®,] and superimposing them to the EBSD map. The satisfactory result is visible in Fig. 6.27.

6.2.2 Co-Ni-Ga sample

The reconstruction procedure presented above, where the 3D shape of the grains within a sample is reconstructed from the extinction spots recorded by a detector mounted in transmission mode, was also applied to reconstruct a much simpler sample than the Fe rod the procedure has been developed on. The

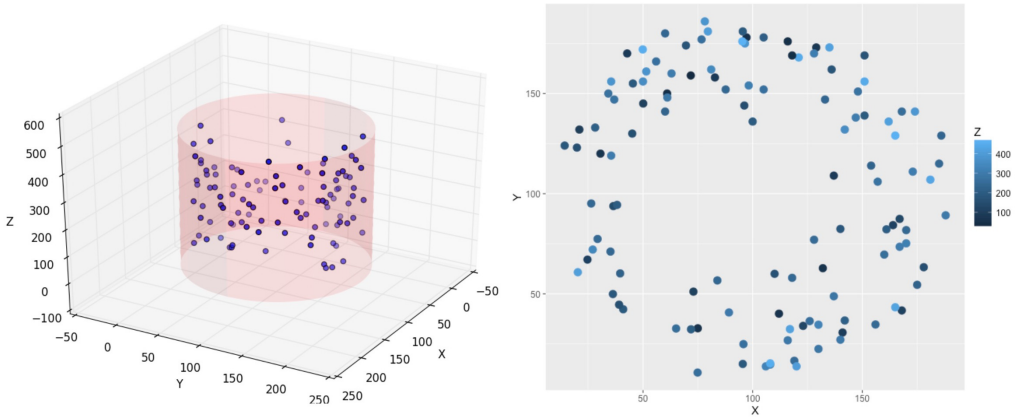

Figure 6.25: Distribution of the centres of mass of the reconstructed grains in 3D (*left*) and on the XY-plane (*right*). On the right, points have different colors depending on their Z coordinates.

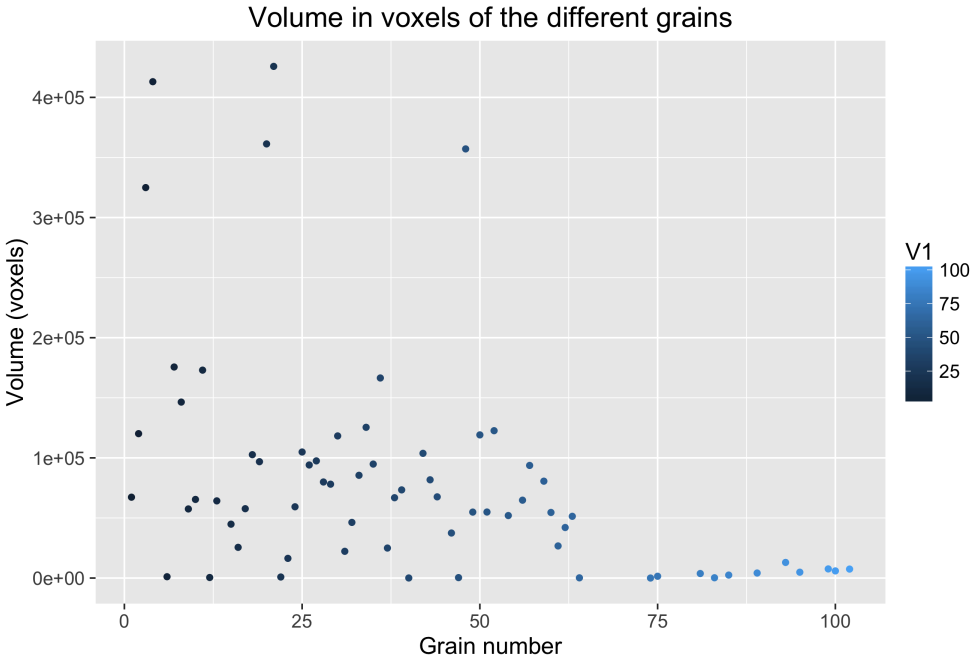

Figure 6.26: Volume, in voxels, of the grains in the final reconstruction. Data relative to different grains are shown in different colours. The grain numbering is the same in Fig. 6.24 and Fig. 6.26.

sample, imaged on February 2016 at SENJU, consisted on two cobalt-nickel-gallium (Co-Ni-Ga) cubes, with size of 4 mm, placed on top of each other in a

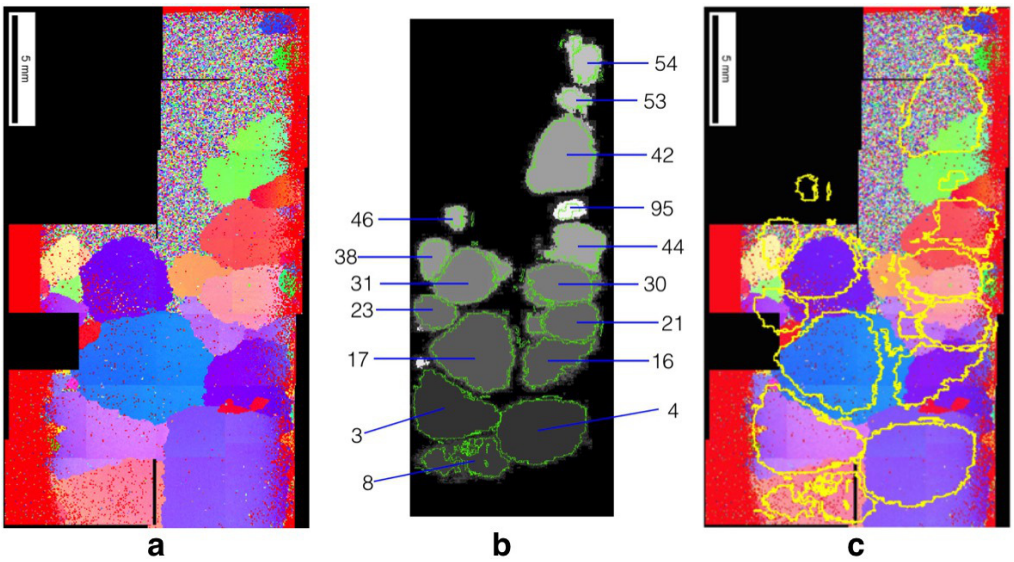

Figure 6.27: Validation using EBSD of the algorithms developed to reconstruct the shape of the grains in 3D. *a*: EBSD map of a sample slice, obtained by cutting the sample in half horizontally first and then vertically. *b*: corresponding slice from the 3DND reconstruction. The ID of each grain is indicated. *c*: EBSD map with superimposed the perimeter of the grains from the 3DND reconstruction.

bamboo-like structure, and a third smaller grain that was ignored for simplicity [Vollmer et al., 2015]. The two large grains were successfully reconstructed using a simplified version of the algorithms developed for the Fe rod: considering two grains with roughtly the same size, there is no need to divide the recorded extinction spots in size groups. As a result only one reconstruction was performed, instead of the four (later combined) done for the Fe sample.

With its very simple structure, the Co-Ni-Ga sample was chosen to illustrate the indexing procedure based on the analysis of the transmission data, which will be presented in Ch. 7.

6.3 BEFORE INDEXING - DATA FILTERING

Section 7.1 will present how to index grains using the distribution of their extinction spots in the $\omega\lambda$-plane. To make the indexing easier, data were filtered by excluding, for each grain, the extinction spots that do not contain the projection of the centre of mass of the corresponding grain. For a grain with centre of mass in (x_{CM}, y_{CM}, z_{CM}), the projection y_d on the detector can be calculated using Eq. 6.8.

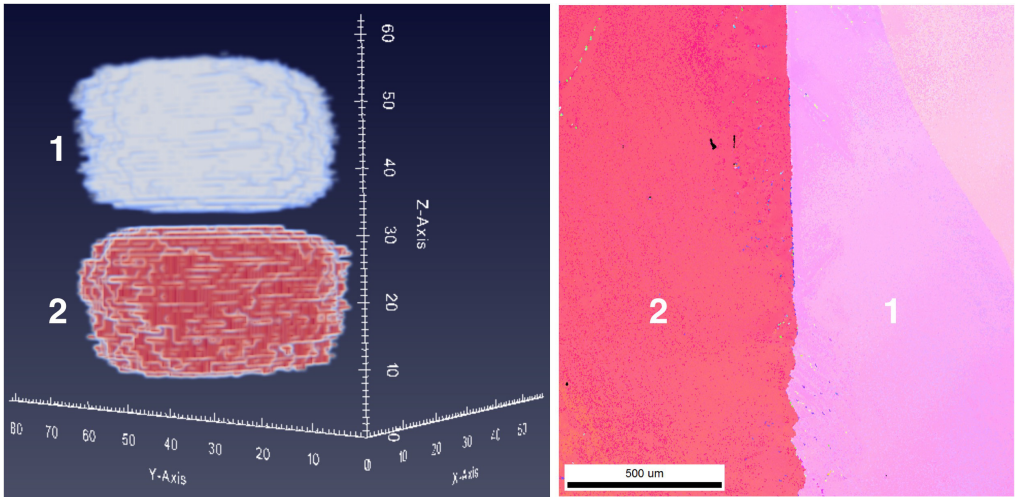

Figure 6.28: *Left*: 3D reconstruction of the two largest grains (cubes with 4 mm side) in the Co-Ni-Ga sample studied at SENJU. *Right*: EBSD map of a sample slice. The grain numbering is the same in the two figures.

In this way, grains are indexed using information relative to less extinction spots than those used to reconstruct the 3D shape of the grains.

6.4 CHAPTER SUMMARY

At SENJU, we studied an iron sample using a time-of-flight neutron beam, and collected real-space information via a transmission detector. To analyse these data and reconstruct, starting from the extinction spots, the grains within the sample, we developed a suite of algorithms including various new solutions, that address the peculiarities of the collected data (they are energy-resolved and the extinction spots can hardly be distinguished). We successfully reconstructed in 3D the shape and justaxposition of 108 grains.

The method used to analyse the Fe data is general and can be applied to study other polycrystalline samples containing grains in the hundreds of microns to millimetre scale, investigated using a time-of-flight neutron beam. We tested the validity of the developed algorithms by reconstructing a completely different sample (Co-Ni-Ga "bamboo" sample, consisting of two large grains and a smaller one) and by comparing the outline of the grains in a section of the 3D model with the shapes in the corresponding EBSD map.

7

Grain indexing

Contents

THIS chapter presents two different approaches to index grains composing a polycrystalline sample. The first, new, approach is based on the analysis of transmission data and is presented in Sec. 7.1. In Sec. 7.2, the orientation of the grains is calculated from the diffraction data using GrainSpotter [Schmidt, 2014]. In Sec. 7.3, orientations calculated from the transmission and diffraction data are compared and bechmarked against 2D grain orientation maps from electron backscattering diffraction (EBSD). Lastly, in Sec. 7.4 a procedure to reconstruct the shape of the grains from their orientation is outlined.

7.1 INDEXING USING NEAR-FIELD DATA

In Ch. 6 we showed how to reconstuct the 3D shape and justaxposition of the grains composing a polycrystalline sample illuminated by a time-of-flight neutron beam. For each grain, the procedure returns the distribution of the rela-

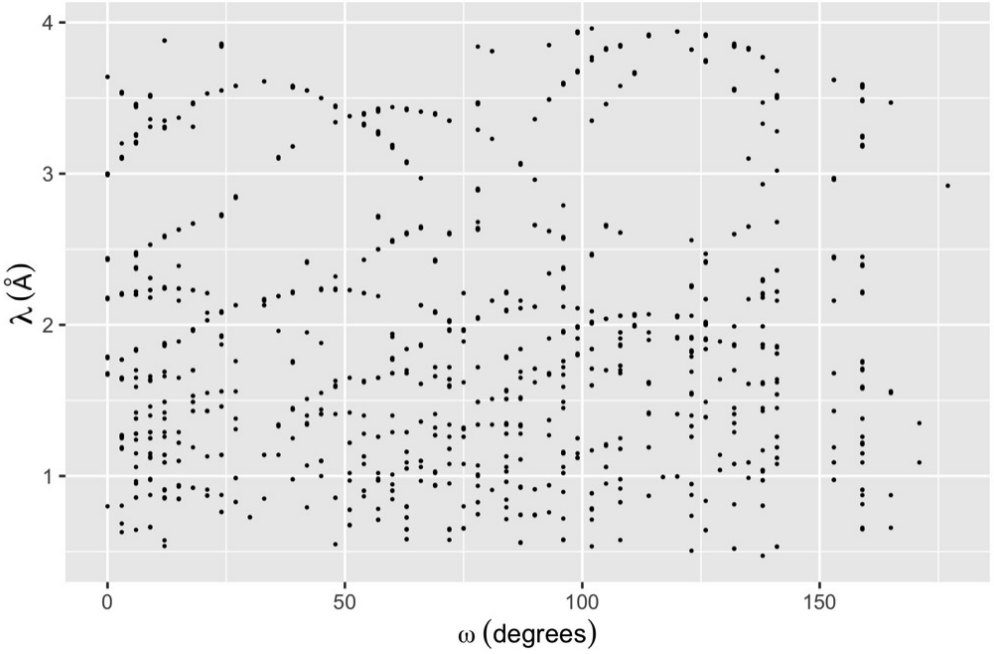

Figure 7.1: Distribution, as a function of the rotation angle, of the wavelength intervals where the extinction spots for grain 31 were detected. We denote each interval centre with λ.

tive extinction spots over the different sample rotation angles ω_i and the wavelength intervals Λ_i. The wavelength intervals have fixed width (12.8 μs), with $1 \leq i \leq 2423$ for the Fe sample and $1 \leq i \leq 2500$ for the Co-Ni-Ga sample. To make the grain indexing easier, the extinction spot distribution was filtered following the procedure described in Ch. 6.3.

As visible in Fig. 7.1, in the $\omega\lambda$-space the occurrence of extinction spots is distributed along multiple curves. To fit these point distributions we need to establish a forward model that calculates, for each orientation, the corresponding functions in the $\omega\lambda$ space. We will now derive the forward model.

The starting points are Bragg's law

$$\lambda = 2d \sin\theta \tag{7.1}$$

and the diffraction equation in the form used by [Poulsen et al., 2001]:

$$\mathbf{G} = \frac{d}{2\pi}\Omega U \mathcal{B}\mathbf{h} \tag{7.2}$$

where $|\mathbf{G}| = 1$. d is the spacing between the lattice planes, Ω is a left-hand

rotation around the z-axis[1] by an angle ω, U is the orientation matrix, $\mathbf{h} = \begin{pmatrix} h \\ k \\ l \end{pmatrix}$ and $\mathcal{B}$ is the matrix transforming the hkl lattice into the reciprocal space.

The detailed expressions of Ω and $\mathcal{B}$ are

$$\Omega = \begin{pmatrix} \cos\omega & \sin\omega & 0 \\ -\sin\omega & \cos\omega & 0 \\ 0 & 0 & 1 \end{pmatrix} \tag{6.7}$$

and

$$\mathcal{B} = \begin{pmatrix} a^* & b^*\cos\gamma^* & c^*\cos\beta^* \\ 0 & b^*\sin\gamma^* & -c^*\sin\beta^*\cos\alpha \\ 0 & 0 & c^*\sin\beta^*\sin\alpha \end{pmatrix}, \tag{7.3}$$

where (a, b, c, α, β, γ) and (a^*, b^*, c^*, α^*, β^*, γ^*) are the lattice parameters in the direct and reciprocal space.

Using Bragg's equation and renormalizing $\mathbf{G}$ so that $|\mathbf{G}| = \frac{\lambda}{2d} = \sin\theta$, as required by the equivalence of Bragg's and Laue's conditions (see Ch. 2), Eq. 7.2 can be rewritten as

$$\mathbf{G} = \frac{\lambda}{4\pi}\Omega U \mathcal{B}\mathbf{h} \tag{7.4}$$

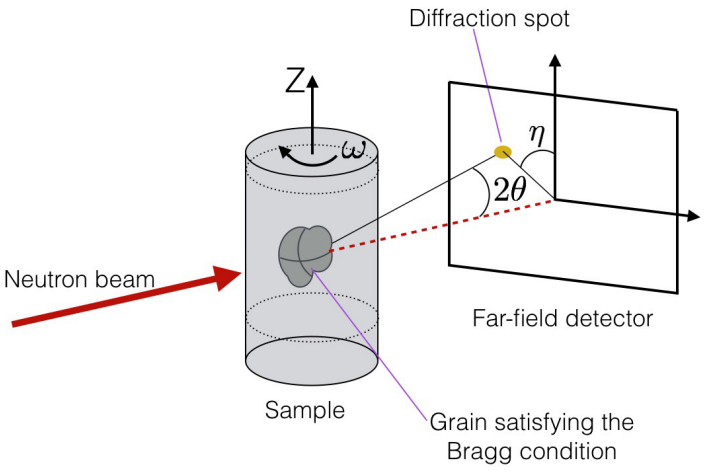

Figure 7.2: Sketch of the diffraction geometry, with definition of the angles ω, 2θ and η.

[1]The rotation stage used at SENJU moved in the left-hand direction.

Following the geometry sketched in Fig. 7.2, $\mathbf{G}$ can be expressed as a function of 2θ and η [Schmidt, 2014]:

$$\mathbf{G} = \frac{1}{2}\begin{pmatrix} \cos 2\theta - 1 \\ -\sin 2\theta \sin \eta \\ \sin 2\theta \sin \eta \end{pmatrix} \tag{7.5}$$

Considering the first component of $\mathbf{G}$ and using Bragg's law, from 7.5 we have[2]

$$\mathbf{G}_1 = -\sin^2 \theta = -\frac{\lambda^2}{4d^2} \tag{7.6}$$

hence from Eq. 7.4 we have

$$-\frac{\lambda^2}{4d^2} = \frac{\lambda}{4\pi}(\Omega U \mathcal{B}\mathbf{h})_1 \tag{7.7}$$

Writing that λ is a function of ω and introducing the vector $\mathbf{v} = \mathcal{B}\mathbf{h}$, we have the fundamental equation used to fit the point distribution in the $\omega\lambda$-space:

$$\boxed{\lambda(\omega) = -\frac{d^2}{\pi}(\Omega U \mathcal{B}\mathbf{h})_1 = -\frac{d^2}{\pi}(\Omega U \mathbf{v})_1} \tag{7.8}$$

Writing all terms and using $|\mathbf{G}| = \frac{\lambda}{2d} = \frac{\lambda}{4\pi}|\mathcal{B}\mathbf{h}|$, wich gives $|\mathcal{B}\mathbf{h}| = \frac{2\pi}{d}$, Eq. 7.8 becomes

$$\begin{aligned} \lambda(\omega) = -\frac{4\pi}{|\mathcal{B}\mathbf{h}|^2}\Big[&(u_{11}v_1 + u_{12}v_2 + u_{13}v_3)\cos\omega + \\ &(u_{21}v_1 + u_{22}v_2 + u_{23}v_3)\sin\omega\Big] \end{aligned} \tag{7.9}$$

For a given reflection, corresponding to a given *hkl* family, the coefficients $A = u_{11}v_1 + u_{12}v_2 + u_{13}v_3$ and $B = u_{21}v_1 + u_{22}v_2 + u_{23}v_3$ have constant value, leading to the concise expression

$$\lambda(\omega) = -\frac{4\pi}{|\mathcal{B}\mathbf{h}|^2}(A\cos\omega + B\sin\omega) \tag{7.10}$$

with the functions of ω being the only variables in the right-hand side.

[2] $\cos(2\theta) - 1 = \cos^2\theta - \sin^2\theta - 1 = 1 - \sin^2\theta - \sin^2\theta - 1 = -2\sin^2\theta$.

7.1.1 INDEXING PROCEDURE FOR EXTINCTION SPOTS

For a given grain the correct orientation is the one that, through the forward model, best fits the distribution of the relative extinction spots in the $\omega\lambda$-space. This is the procedure used to assign a grain the corresponding orientation is, thus:

1. Scan the Rodrigues space for orientations. For each considered orientation, calculate the relative $\lambda(\omega)$ curves, which fit the distribution of extinction spots in the $\omega\lambda$-space.

2. For the various orientations, measure the distance of the fitting curves from the experimental values.

3. Select the orientation whose $\lambda(\omega)$ curves are closest to the experimental values.

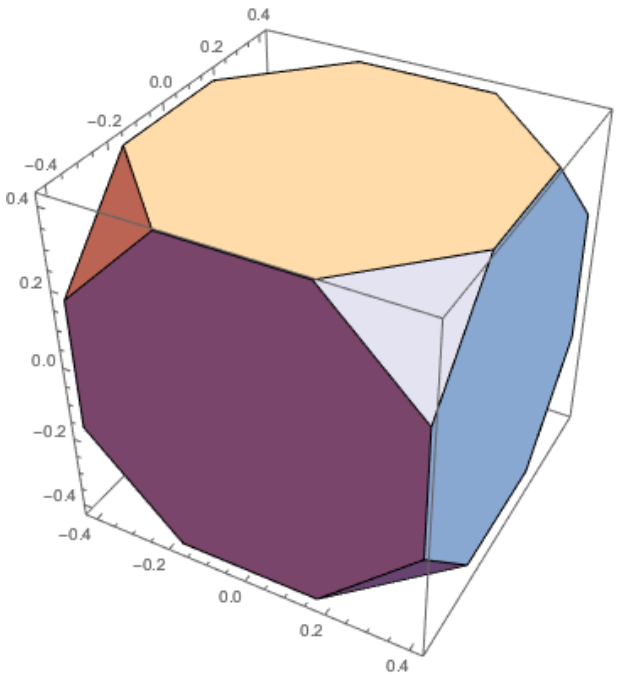

Figure 7.3: For materials with cubic crystal symmetry, the fundamental zone of the Rodrigues space is a truncated cube with side $2\cdot(\sqrt{2}-1)$ [He and Jonas, 2007].

The region of the Rodrigues space sampled by the forward model is a cube with side $2\cdot(\sqrt{2}-1)$ centered around the origin. The cube is an approximation

of the *fundamental zone*, that for crystals with cubic symmetry, as both the considered samples (Fe and Co-Ni-Ga) are, is a truncated cube of size $2 \cdot (\sqrt{2}-1)$ (see Fig. 7.3) [He and Jonas, 2007]. The fundamental zone has two main properties: it contains all possible orientations and the axioms of Euclidean geometry are approximately valid inside it. Note that Rodrigues space is Euclidean only locally, but not generally [Morawiec and Field, 1996].

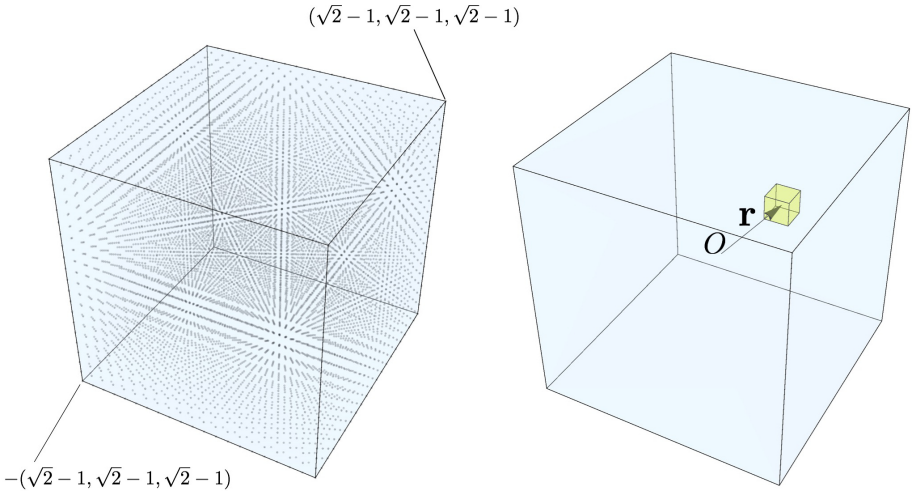

Figure 7.4: For a given grain, the *forward model* searches the Rodrigues space for orientations fitting the distribution of the relative extinction spots in the $\omega\lambda$-space. *Left*: this is done by considering, at regular steps, the points in a cube of side $2(\sqrt{2}-1)$, centered on the origin in the Rodrigues space. *Right*. Once an orientation candidate **r** is found, the procedure is repeated considering a smaller volume centered on it.

In detail, for each given point, the model calculates the corresponding orientation matrix U and, for chosen *hkl* sets, the relative $\lambda(\omega)$ functions using Eq. 7.10. When the $\lambda(\omega)$ curves that fit the experimental data are found, the corresponding orientation is refined by sampling, with a finer grid, a smaller region of the Rodrigues space built around the orientation vector (see Fig. 7.4). Alg. 5 presents the forward model in pseudocode.

For a given grain, we proceeded as follows to choose the $\lambda(\omega)$ curves best fitting the extinction spots distribution in the $\omega\lambda$-space:

1. For each curve, measure the vertical distance from it (d_i) of the points located in a band around it (see Fig. 7.5).
2. Considering all the different $\lambda(\omega)$ curves, calculate $D = \sum_i d_i$.
3. Select the set of curves returning the minimum D.

Algorithm 5 Forward model to index grains using transmission data

for each grain **do**
  consider the extinction spots distribution in the $\omega\lambda$-space
  sample with regular steps a cube of size $2(\sqrt{2}-1)$, built around the origin in the Rodrigues space
  for each considered point **do**
    calculate the orientation matrix U
    for different hkl sets **do**
      calculate $\lambda(\omega)$ using 7.10
    end for
    calculate the distance of the (ω,λ) values from the $\lambda(\omega)$ curves, as illustrated in Fig. 7.5
  end for
  consider the orientation U_1, corresponding to the minimal distance from the (ω,λ) values
  refine U_1 by sampling with smaller steps the Rodrigues space region around it and recalculating $\lambda(\omega)$
  assign to the grain the refined orientation U_2
end for

To index the orientation of the Fe and Co-Ni-Ga grains, we considered the *hkl* families 110, 200 and 211. With the forward model, we fitted the points with $\lambda > 2\text{Å}$: at lower wavelengths, the point distribution is more dense and harder to fit with the $\lambda(\omega)$ curves.

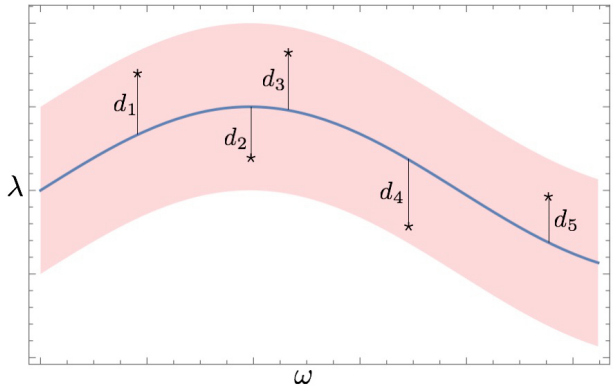

Figure 7.5: To compare $\lambda(\omega)$ curves relative to different orientations, we used the vertical distanced_i of the fitted points (extinction spots) from the curve. The set of curves returning the lower $D = \sum_i d_i$ was taken as the best fit.

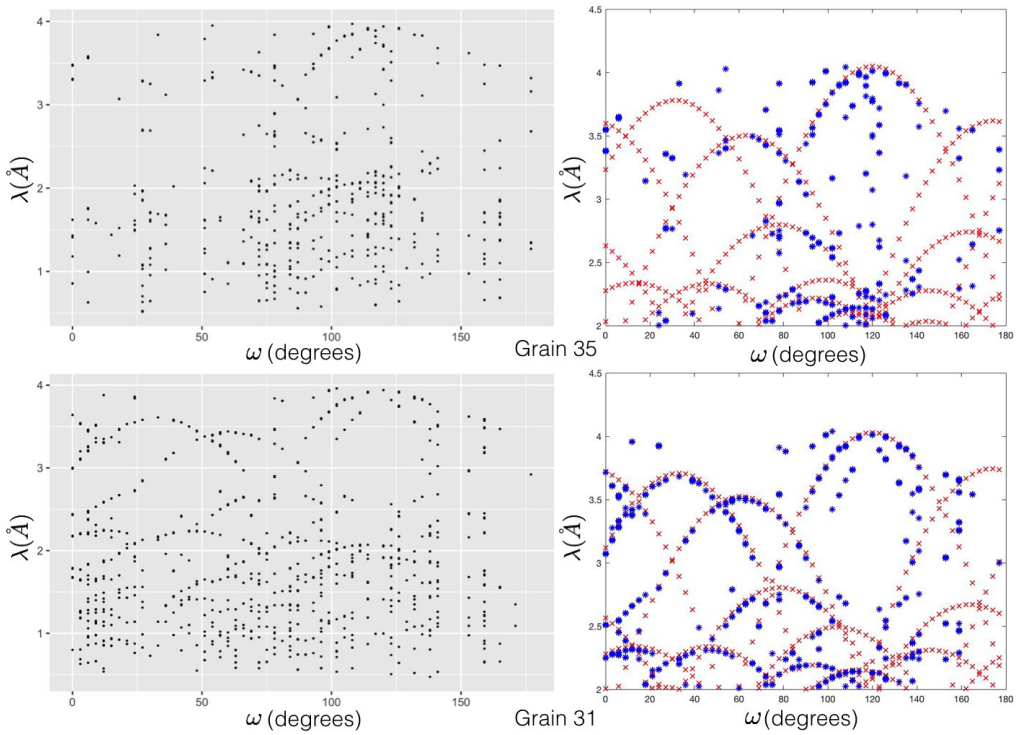

Figure 7.6: The forward model can index both sparse and overpopulated datasets. Raw (*left*) and indexed (*right*) data relative to the iron sample, grain 35 (*above*) and 31 (*below*). The wavelength range is different in the left and right figures: above 2 Å, curves are better separated and easier to distinguish.

The forward model proved to be a robust solution to index grains composing a polycrystalline sample starting from the data collected in transmission mode. It can be used to index both sparse datasets (where data relative to only a few angles are available) and overcrowded ones (with data relative to more than one grain). Examples are shown in Fig. 7.6.

If data are available for almost every angle, grains could also be indexed using the Hough transform, following an approach similar to the one presented in 6.1.3.5 [Hough, 1962]. In this case, the $\lambda(\omega)$ curves are calculated directly from the distribution of points in the (ω, λ) space, and the grain orientations are then calculated from the $\lambda(\omega)$s.

7.1.2 UNIQUENESS OF THE SOLUTION

While the (ω, λ) dataset is only two dimensional, the data collected at SENJU are four dimensional: three dimensions are set by the spatial coordinates of

the diffraction spots on the detector banks (defining **G**) and one is set by the time-of-flight (corresponding to a wavelength and hence to a d-spacing) when the diffraction spot is collected. In the following, we will show that the lower-dimensional (ω, λ) data does not uniquely determine the correct crystallographic orientation. To overcome this limitation, we developed a procedure to identify the correct orientation using additional information from the diffraction spots recorded by the MCP detector.

Following the procedure outlined in Alg. 5, we fitted the points in the (ω, λ) space using curves with

$$\lambda(\omega) = -\frac{4\pi}{|\mathcal{B}\mathbf{h}|^2}\Big[(u_{11}v_1 + u_{12}v_2 + u_{13}v_3)\cos\omega + (u_{21}v_1 + u_{22}v_2 + u_{23}v_3)\sin\omega\Big] \tag{7.9}$$

As will be shown, different orientation matrices can return the same $\lambda(\omega)$. This section describes why, for each grain, there are at least two candidate orientations, and how we selected the correct one.

7.1.2.1 The C symmetry

To calculate the number of orientation candidates per grain, let us start from Eq. 7.9 and from the expression for the determinant of U. To be a proper rotation matrix, U must satisfy the condition $\det(U) = 1$, with

$$\det(U) = u_{11}(u_{22}u_{33} - u_{23}u_{32}) + u_{22}(u_{11}u_{33} - u_{13}u_{31}) + u_{33}(u_{11}u_{22} - u_{12}u_{21}) \tag{7.11}$$

Let us consider the inversion $v_3 \to -v_3$. A change of sign of v_3 in Eq. 7.9 results in the following changes:

1. $u_{13} \to -u_{13}$ and $u_{23} \to -u_{23}$, to conserve Eq. 7.9.
2. $u_{31} \to -u_{31}$ and $u_{32} \to -u_{32}$, to conserve Eq. 7.11.

In other words, changing the sign of v_3 results in the following changes of sign for the elements of the orientation matrix U:

$$U_{v_3} = \begin{pmatrix} + & + & + \\ + & + & + \\ + & + & + \end{pmatrix} \to U_{-v_3} = \begin{pmatrix} + & + & - \\ + & + & - \\ - & - & + \end{pmatrix} \tag{7.12}$$

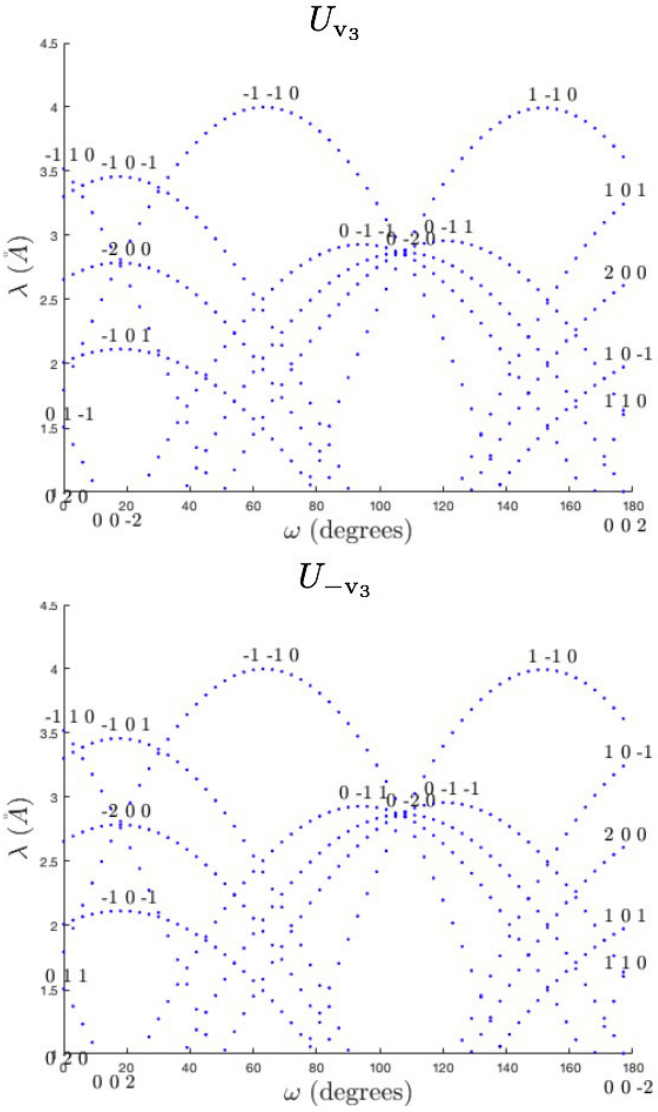

Figure 7.7: Even if the orientation matrices U_{v_3} and $U_{-v_3} = CU_{v_3}C$ are different, they result in the same $\lambda(\omega)$ curves in the $\omega\lambda$-space. The plot shows how, in the two cases, a given curve corresponds to the indices hkl (U_{v_3}) and $hk-l$ (U_{-v_3}).

It is therefore necessary to assign to each grain the correct orientation matrix, distinguishing between the cases U_{v_3} and U_{-v_3} (see Fig. 7.7 and 7.8).

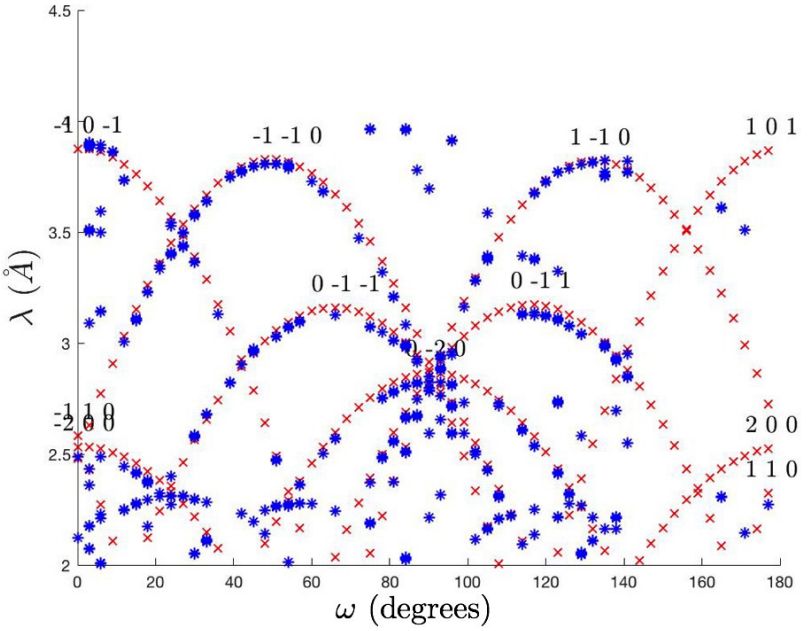

Figure 7.8: Raw data (blue stars) and $\lambda(\omega)$ curves (red crosses) used to fit the (ω,λ) data distribution for grain three of the Fe sample. For each *hkl* family the maximum λ value is, from Bragg's law, $\lambda_{max} = 2 \cdot \frac{a}{\sqrt{h^2+k^2+l^2}}$.

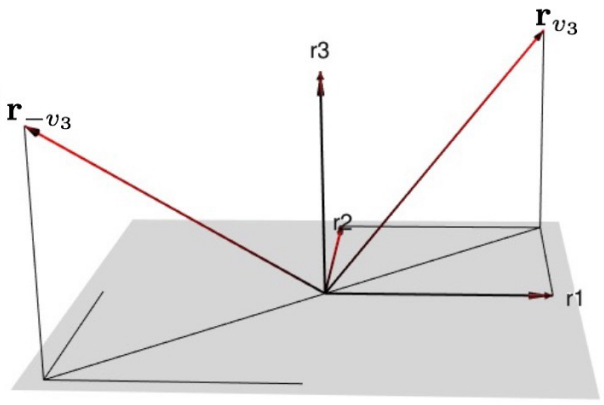

Figure 7.9: The $\lambda(\omega)$ curves (Eq. 7.9) fitting the point distribution in the $\omega\lambda$-space do not uniquely define a grain orientation. In fact, a change of sign of v_3 returns two different orientations, U_{v_3} and $U_{-v_3} = CU_{v_3}C$. Here, orientations are represented by the corresponding Rodrigues vectors $\mathbf{r}_{v_3}$ and $\mathbf{r}_{-v_3}$.

The two orientation matrices and the relative Rodrigues vectors, $\mathbf{r}_{v_3} = \begin{pmatrix} r_1 \\ r_2 \\ r_3 \end{pmatrix}$

and $\mathbf{r}_{-v_3} = \begin{pmatrix} -r_1 \\ -r_2 \\ r_3 \end{pmatrix}$ (see Fig. 7.9 and 7.10) are related by the expressions

$$U_{-v_3} = CU_{v_3}C^{-1} \tag{7.13}$$

$$\mathbf{r}_{-v_3} = -C\mathbf{r}_{v_3} \tag{7.14}$$

with

$$C = \begin{pmatrix} 1 & 0 & 0 \\ 0 & 1 & 0 \\ 0 & 0 & -1 \end{pmatrix} \tag{7.15}$$

$$C = C^{-1} \tag{7.16}$$

By sistematically going through the various possible symmetries, it can be shown that C is the only transformation for which Eq. 7.8 is invariant.

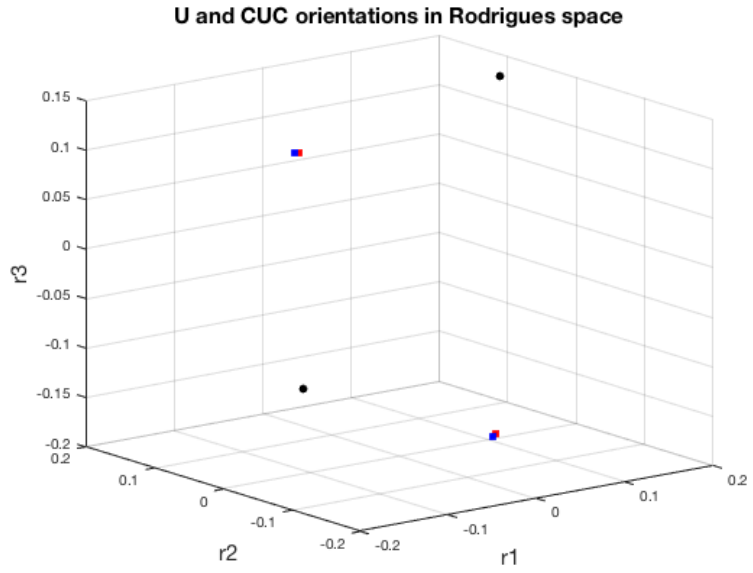

Figure 7.10: For a given grain, the possible orientations U and CUC correspond to identical curves in the $\omega\lambda$-space, and to different vectors in the Rodrigues space. The figure shows orientations U (squares) and CUC (dots) for the two large grains in the Co-Ni-Ga sample. Orientations from the diffraction data are in blue and orientations from the transmission data are in red.

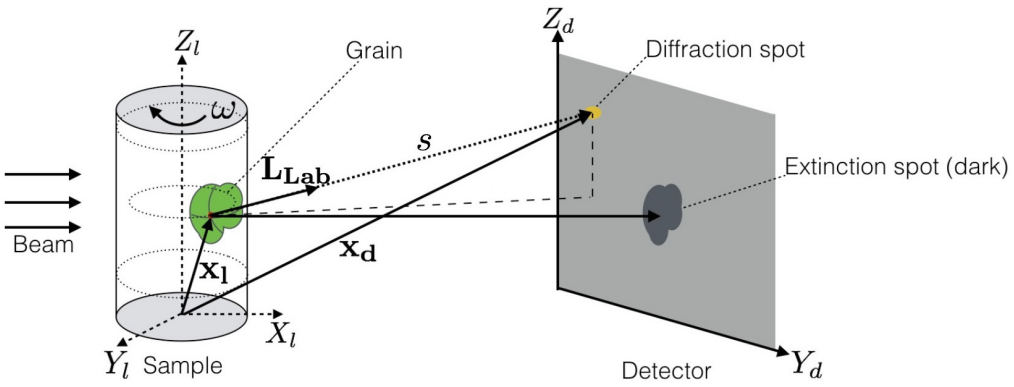

Figure 7.11: The correct orientation of a grain was selected by considering the direction of the diffraction vector $\mathbf{L_{Lab}}$ in real space. In the figure, the laboratory reference system has coordinates (x_l, y_l, z_l) and the detector reference system has coordinates (y_d, z_d). In the laboratory reference system, the position of the centre of mass of the grain is $\mathbf{x_l}$ and the position of the centre of mass of the relative diffraction spot is $\mathbf{x_d}$, with $\mathbf{x_d} = \mathbf{x_s} + \mathbf{L_{Lab}} \cdot s$.

7.1.2.2 How to select the right orientation

To uniquely determine the orientation of a grain we considered the frames, collected by the near-field detector, where both the relative extinction and diffraction spots were visible and we studied the position of the centre of mass of the diffraction spots [Schmidt, 2014].

Let us introduce the reciprocal vector $\mathbf{G^r}$ and the direction, in the sample reference system, of the diffraction vector in real space $\mathbf{L}$ (see Fig. 7.11), defined as

$$\mathbf{G^r} = \Omega^{-1}\mathbf{G} \tag{7.17}$$

$$\mathbf{L} = 2\mathbf{G^r} + \Omega^{-1}|_1 \tag{7.18}$$

with $\mathbf{G} = \frac{\lambda}{4\pi}\Omega U \mathcal{B}\mathbf{h}$ (Eq. 7.2). In the laboratory reference system, the direction of the diffracted beam is given by $\mathbf{L_{Lab}}$, defined as

$$\mathbf{L_{Lab}} = \Omega L \tag{7.19}$$

Fig. 7.14 and 7.15 show the distribution of the $\mathbf{G}$ and $\mathbf{G^r}$ vectors for the Fe sample.

For a grain with centre of mass $\mathbf{x_l}$ in the laboratory reference system, and $\mathbf{x_s}$ in the sample reference system, with

$$\mathbf{x_s} = \Omega \mathbf{x_l} \tag{7.20}$$

the centre of mass $\mathbf{x_d}$ of the relative diffraction spot on the detector plane is, in the laboratory system,

$$\mathbf{x_d} = \mathbf{x_l} + \mathbf{L_{Lab}} s \tag{7.21}$$

For a given geometry, once the orientation U and the hkl indexes are determined, Eq. 7.18 returns a unique $\mathbf{L_{Lab}}$ for a given wavelength (the dependance on λ is included in $\mathbf{G}$), uniquely determining the location of the diffraction spot.

Considering the possible orientations U and CUC, we used Eq. 7.21 to calculate the expected location on the detector plane of the diffraction spots for selected hkl sets. For each diffraction spot, we loaded the frames where it should have been recorded and checked if it was effectively present. To consider possible wavelength shifts, a window of 100 images centered on the expected frame was considered. The procedure is presented in pseudocode in Alg. 6.

Algorithm 6 Procedure to uniquely determine the orientation of a grain

```
for the two possible orientations, U and CUC do
  for selected hkl sets do
    use Eq. 7.21 to calculate the expected position of the relative diffraction
    spots on the detector plane
  end for
  for each expected diffraction spot do
    load the images around it
    check for diffraction spots
    if a diffraction spot is found then
      compare the located position with the calculated one
    end if
  end for
end for
```

Fig. 7.12 shows the expected locations of the diffraction spots for one of the grains within the Fe sample, calculated both for orientation U and for orientation CUC.

Considering the transmission data collected at SENJU for the Fe sample, it was not possible to uniquely determine the orientation of selected grains using the position of diffraction spots as outline above. The main reasons for this are:

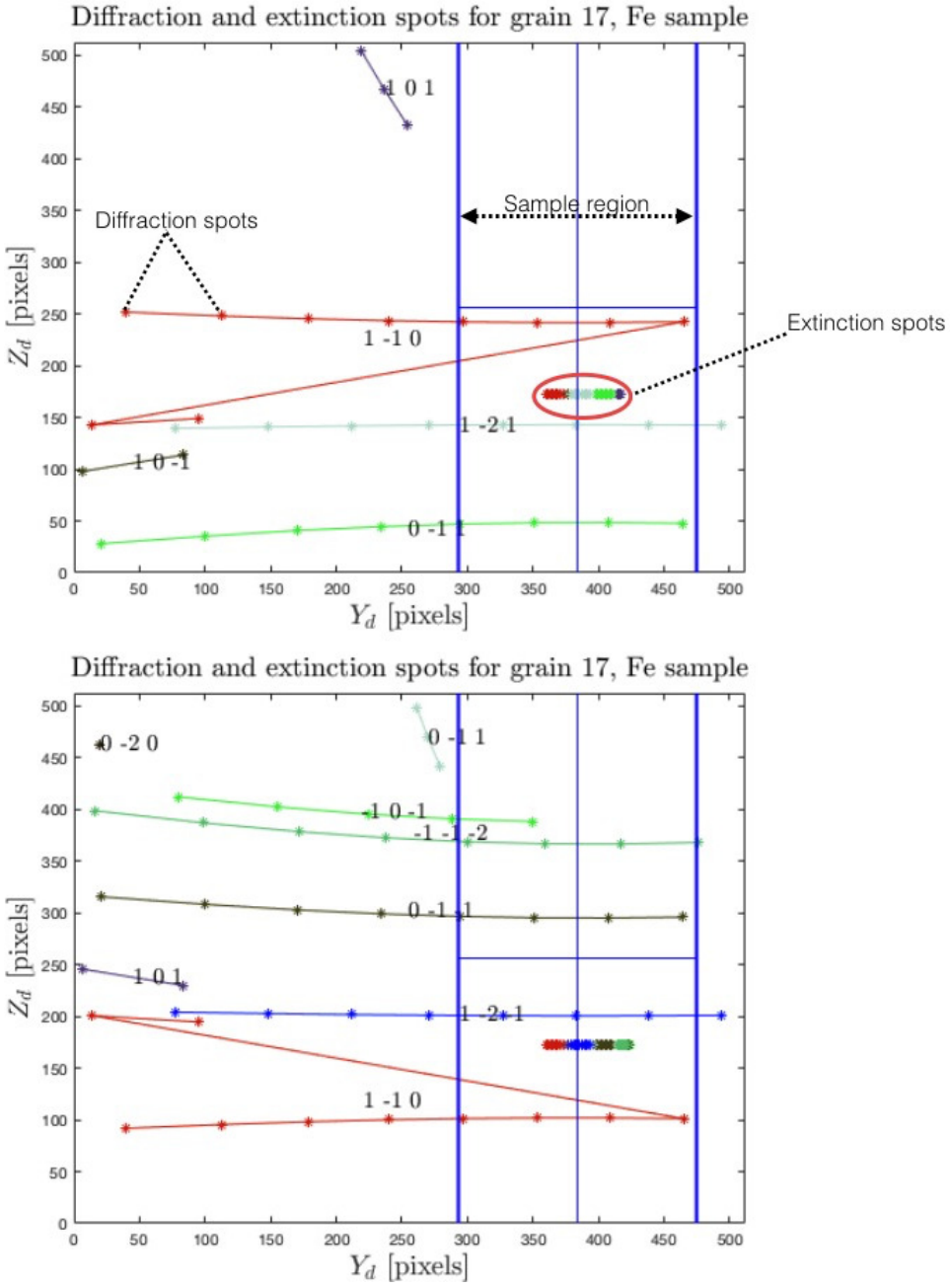

Figure 7.12: Expected location on the detector plane of the diffraction spots for grain 17. Data for orientation *CUC* are shown *above* and data for orientation *U* are shown *below*. Depending on the considered orientation, diffraction spots relative to different *hkl* combinations are recorded in different locations.

1. Diffraction spots are visible only at short wavelengths (below 1.2 Å), where many different spots are often recorded in the same frame;

2. The incident beam has strong tails around the sample (see Fig. 7.13), greately reducing the detector region where diffraction spots can be observed.

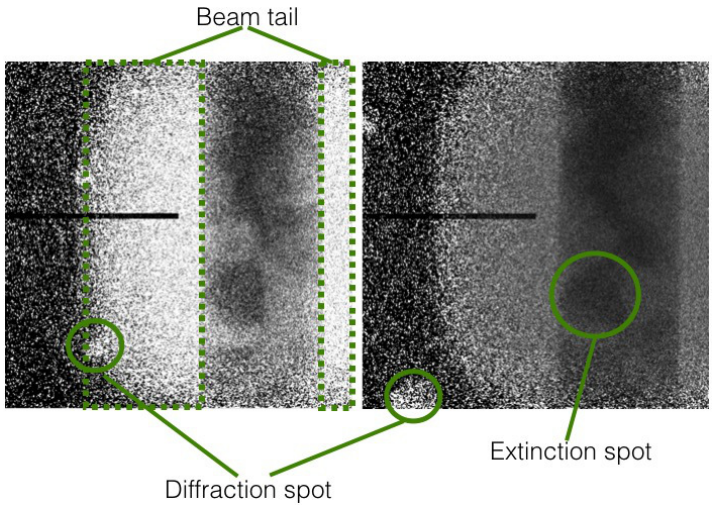

Figure 7.13: Features observed when searching for diffraction spots in the frames recorded by the MCP detector for different time-of-flight.

To overcome these limitations, the following changes in the acquisition mode are suggested:

1. Partially mask the incoming beam, so that it only illuminates the sample. In this way, the background from the direct beam is reduced;

2. Introduce a second rotation axis perpendicular to the Z-axis, to avoid incurring in the $U-CUC$ symmetry. This solution would enable to uniquely determine grain orientations based on transmission data alone, with a small price to pay in terms of acquisition time (the second rotation stage only needs a shorter rotation range).

7.2 INDEXING USING FAR-FIELD DATA

The main limitation of the method presented above, where the orientation of the grains comes from data collected in transmission mode, is that it only works for the grains that have been reconstructed in 3D.

In this Section we will explain how diffraction data can be used to index the grains, and how this can be used to improve the quality of the 3D reconstruction.

7.2.1 STARGAZER AND GRAINSPOTTER

To calculate the orientation of the grains from the diffraction data, we used the STARGazer and GrainSpotter software packages, respectively developed by J-PARC and by S. Schmidt [Ohhara et al., 2009, Schmidt, 2014]. The diffraction data collected by the far-field detectors were processed by STARGazer, returning the position of the Bragg spots at different time-of-flight. The list of **G** vectors was given as an input to GrainSpotter, which identified the crystallographic orientations. Fig. 7.14 shows, in the laboratory and sample reference system, the diffraction spots collected by the far-field detectors when studying the Fe sample at SENJU. For the same data, Fig. 7.15 shows the distribution of the $\mathbf{G}^r$ vectors. The lattice relative to a single grain orientation is shown in Fig. 7.16.

GrainSpotter was originally developed for grains that are part of a polycrystalline sample illuminated by a monochromatic X-ray beam, as in the case of 3DXRD and DCT [Poulsen et al., 2001, Ludwig et al., 2008, Ludwig et al., 2009]. The procedure described above was the first application of GrainSpotter to index time-of-flight neutron diffraction data.

Orientations calculated from the transmission and diffraction data are shown in Fig. 7.17 for the two grains composing the Co-Ni-Ga sample and in Fig. 7.18 for two Fe grains. For a given grain the difference between the orientations from the transmission and the diffraction data, also called *misorientation*, can be calculated as

$$\min_i \left[\arccos\left(\frac{\mathrm{tr}(U_{tr} E_i U_2') - 1)}{2} \right) \right] \tag{7.22}$$

where tr is the trace of a matrix and E_i are the space group generators, which are the symmetry operators of a given crystalline structure [Rupp, 2009].

From the diffraction data collected studying the Fe sample, GrainSpotter returned 107 unique orientations, well matching with the number of grains reconstructed from transmission data (108). Fig. 7.20 shows, in Rodrigues space, the orientations calculated by GrainSpotter for 107 Fe grains (above) and for the two larger grains in the Co-Ni-Ga sample (below).

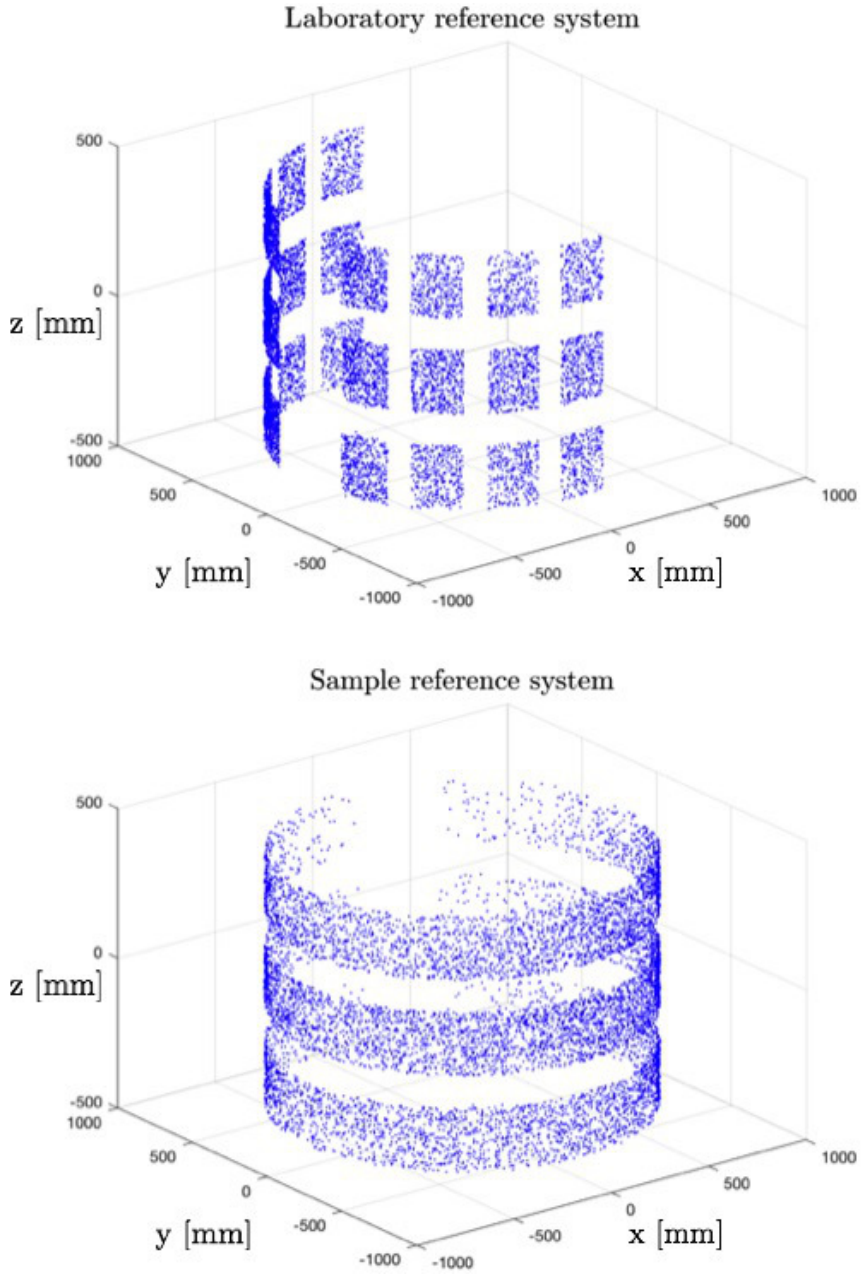

Figure 7.14: Distribution, in the laboratory (*above*) and in the sample (*below*) reference system, of the diffraction spots recorded at SENJU when illuminating the Fe sample.

GrainSpotter returns no information on the location of the grains. The only spatial information available came from the analysis of the transmission data, from which the orientation of the grains was also calculated. Considering an

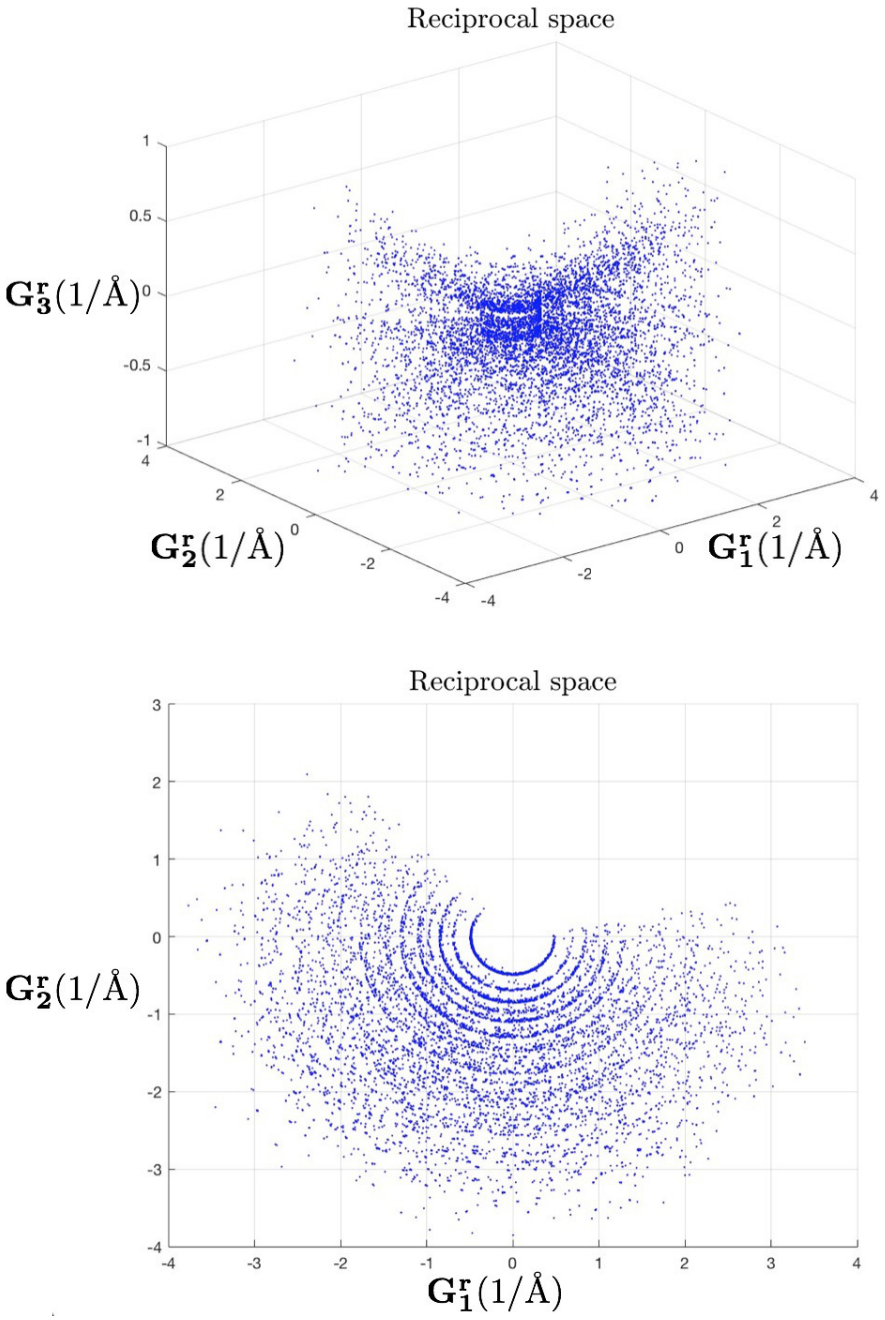

Figure 7.15: Distribution in reciprocal space of the $\mathbf{G^r}$ vectors relative to the Fe sample. *Below*: the circular profiles show the $d_s = d^{-1}$ relative to different *hkl* combinations, with $d = \frac{a}{h^2+k^2+l^2}$ (cubic system).

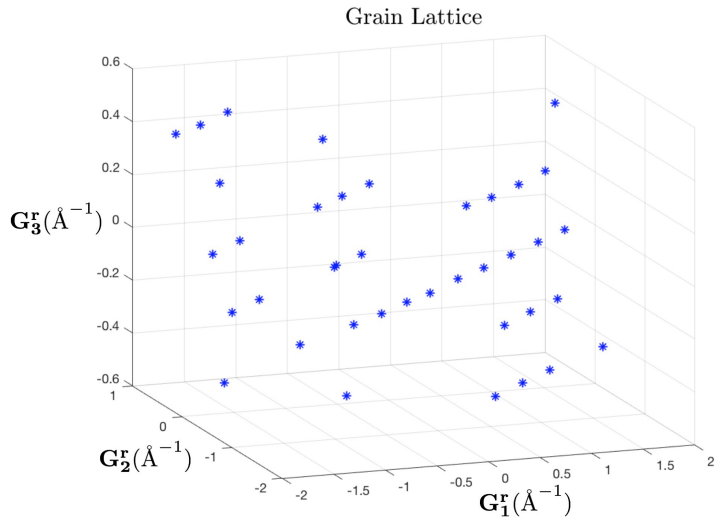

Figure 7.16: Lattice relative to a single grain orientation.

orientation U_{FF} returned by GrainSpotter, the relative grain can be located by searching for the closest orientation U_{NF}, calculated from transmission data. As a distance between the two orientation matrices, the minimum of the norm distance was considered, with the norm distance defined as [Rudin, 1964]

$$d(U_{FF}, U_{NF}) = \max_{1\leq i\leq 3} \max_{1\leq j\leq 3} |a_{ij} - b_{ij}| \tag{7.23}$$

where a_{ij} and b_{ij} are the elements of U_{FF} and U_{NF}.

7.3 COMPARISON WITH ORIENTATIONS FROM EBSD

Electron backscatter diffraction (EBSD) returns the orientation of the grains on the surface of the considered sample, illuminated by an electron beam [Wilkinson and Britton, 2012]. Fig. 6.28 shows the EBSD grain map for a section of the Co-Ni-Ga sample.

Table 7.1 lists the misorientation between the two large grains in the Co-Ni-Ga sample in the following cases: *a)* orientations calculated from the transmission data, *b)* orientations calculated from the diffraction data, *c)* orientations returned by EBSD, expressed following Bunge's convention [Maitland and Sitzman, 2007]. Considering that the uncertainty from *EBSD* is between 1° and 2°, the agreement between the three misorientation values is good.

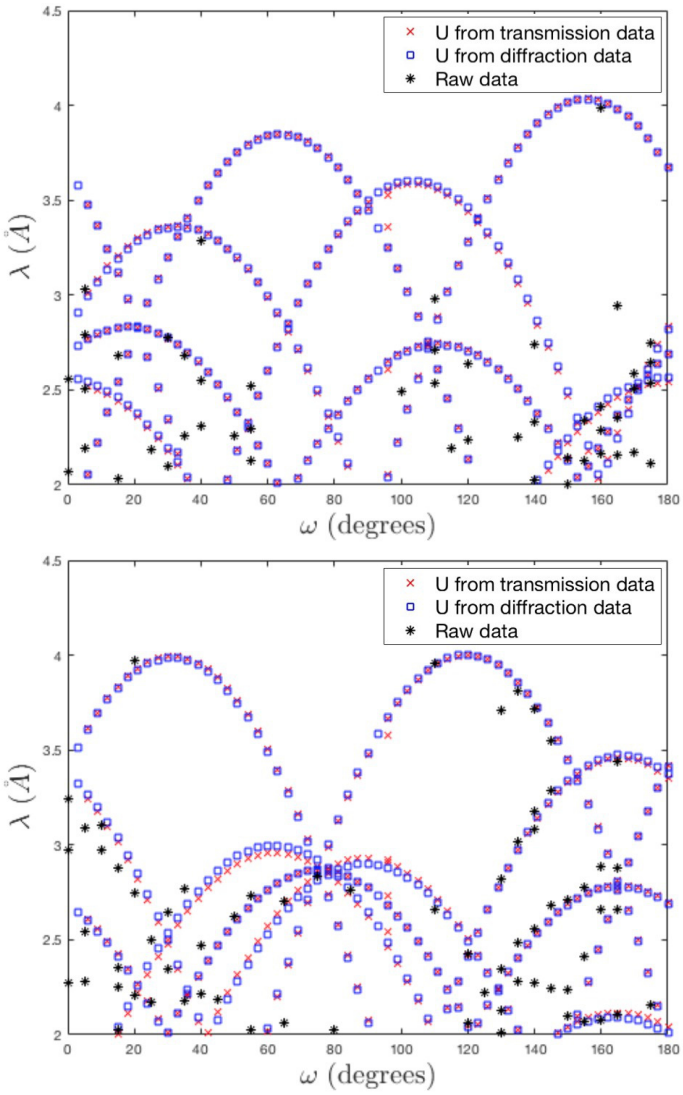

Figure 7.17: Orientations, shown as $\lambda(\omega)$ curves, of the two larger Co-Ni-Ga grains. *Top*: grain 1, *bottom*: grain 2. Data relative to the extinction spots are shown as black stars, the $\lambda(\omega)$ curves calculated from the transmission data as red crosses and the $\lambda(\omega)$ curves calculated from the diffraction data as blue squares. The misorientation between the orientation calculated from the transmission and the diffraction data is 0.84° for grain 1, and 0.57° for grain 2.

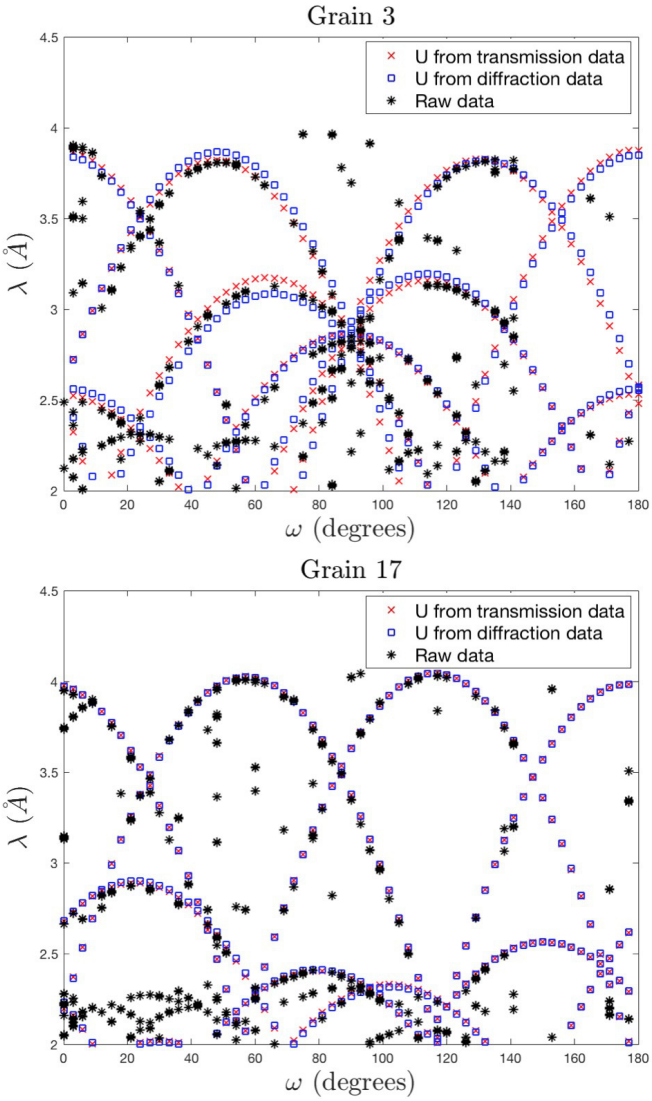

Figure 7.18: Orientations, shown as $\lambda(\omega)$ curves, of the Fe grains 3 and 17. Extinction spots data are shown as black stars, the $\lambda(\omega)$ curves calculated from the transmission data as red crosses and the $\lambda(\omega)$ curves calculated from the diffraction data as blue squares. GrainSpotter returns 107 unique orientations, with no spatial information on to which grains they refer to. The orientation, calculated from the far-field data, relative to each grain (U_{FF}) was selected by searching for the matrix with the minimum norm distance from the U_{NF}, which is the orientation calculated from the transmission data. The misorientation between the orientation calculated from the transmission and the diffraction data is 4.56°, probably due to mosaicity, for grain 3 and 0.45° for grain 17.

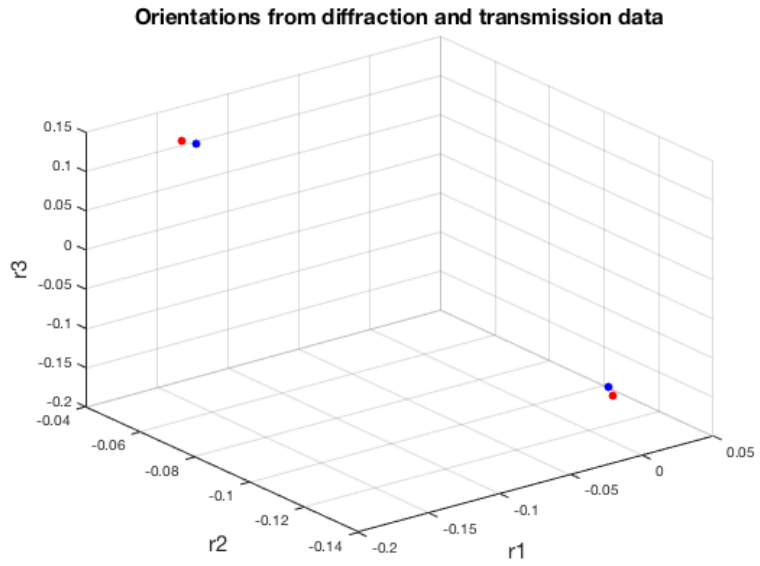

Figure 7.19: Orientation, in Rodrigues space, of the two large grains within the Co-Ni-Ga sample investigated at SENJU. Orientations calculated from the diffraction data and from the transmission data (correct orientation selected based on the one from diffraction data) are plotted in blue and red, respectively.

Transmission data	Diffraction data	EBSD
39.95°	39.72°	40.48°

Table 7.1: Misorientation between the two large grains in the Co-Ni-Ga sample. The difference in orientation is calculated considering the transmission data, the diffraction data and what returned by the EBSD analysis.

7.4 3D RECONSTRUCTION STARTING FROM DIFFRACTION DATA

The prerequisite for reconstructing grain shapes based on trasmission data is to correctly identify and group extinction spots relative to the different grains (mode *I*, presented in Ch. 6). When both transmission and diffraction data are available, the grain shapes can also be reconstructed following mode II, which proceeds in the opposite way: for one of the orientations calculated by GrainSpotter, the relative extinction spots are selected and the grain shape reconstructed.

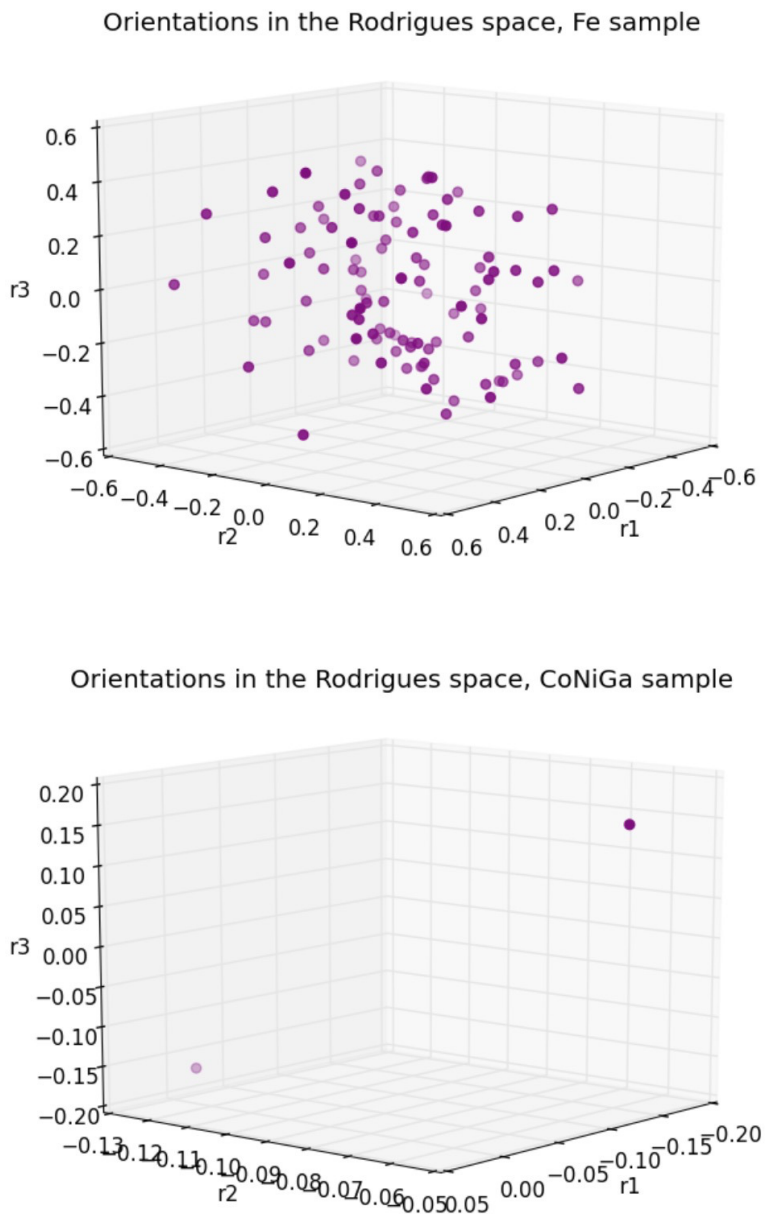

Figure 7.20: Distribution in Rodrigues space of the grain orientations for the Fe and the Co-Ni-Ga sample, calculated from the diffraction data using GrainSpotter. 107 orientations are shown for the Fe sample and two for the Co-Ni-Ga sample, consisting of two grains. Data are represented in a relaxed version of the fundamental zone, which is a truncated cube of side $2(\sqrt{2}-1)$.

These are the steps we followed to reconstruct a grain in mode II:

1. Consider a given orientation
2. Consider the relative $\lambda(\omega)$ curves.
3. Consider the a region of the $\omega\lambda$-plane, with width 40 frames, built around the $\lambda(\omega)$ curves. The size of the frame was chosen considering that the maximum number of consective MCP frames where the same extinction spot is visible is about 40.
4. Search for extinction spots in the images selected in point 3.
5. Follow the reconstruction recipe presented in Ch. 6, where extinction spots are grouped and combined.
6. Backproject the combined extinction spots to get a 3D reconstruction of the grain relative to the considered orientation (the procedure is described in Sec. 6.1.3.6).

In principle, mode II enables reconstructing a number of grains equal to the orientations calculated by GrainSpotter.

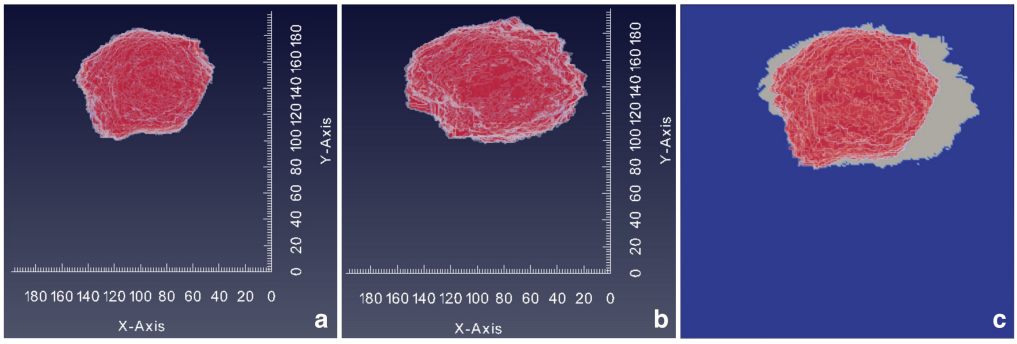

Figure 7.21: When both transmission and diffraction data are collected, the 3D shape of a grain can be reconstructed in two different ways. Mode I consists in searching the transmission data for the relative extinction spots, which are then combined and backprojected. In mode II the starting point is U, one of the orientations calculated from the diffraction data. Using the $\lambda(\omega)$ curves relative to U, the extinction spots relative to the grain with orientation U are selected. The spots are then combined as in mode I. *a*: grain 17 of the Fe sample, reconstructed from the transmission data (mode I). *b*: the same grain, reconstructed from the orientation calculated from the diffraction data (mode II). *c*: 2D section of the grain in *b*, and 3D shape of the grain in *a*.

For both mode I and II, linear solvers such as the Algebraic Reconstruction Technique (ART), the Simultaneous Iterative Reconstruction Technique (SIRT) or Total Variation (TV) may help to overcome this limitation [Gordon et al., 1970, Avinash and Slaney, 1988, Rudin et al., 1992].

Reconstruction mode	Centre of mass (voxels)	Volume (voxels^3)
I	(96,21; 143,73; 157,23)	$4.73 \cdot 10^5$
II	(85,72; 142,18; 162,18)	$5{,}38 \cdot 10^5$

Table 7.2: To benchmark the two shape reconstruction modes, we used them to reconstruct the same Fe grain. While mode I requires no diffraction data, the starting point for mode II is the grain orientation, calculated from diffraction data. The two grains are shown in Fig. 7.21.

7.5 CHAPTER SUMMARY

In this Chapter, we presented the procedures used to calculate grain orientations from transmission and diffraction data. The indexing procedure based on the analysis of the transmission data does not uniquely determine a grain orientation. This limitation could be overcomed with simple modifications in the experimental setup (it is necessary to collect more diffraction spots using the MCP detector). Using GrainSpotter, we calculated 107 unique orientations, which in principle correspond to 107 different grains. The number well agrees with the number of grain shapes reconstructed from transmission data, 108. Orientations calculated from transmission and diffraction data well agree, and their agreement with the orientations returned by EBSD is within the EBSD uncertainty.

For a given orientation returned by GrainSpotter, we selected the relative extinction spots and showed that they can be used to reconstruct a 3D grain shape. In first approximation, the shape agrees with the one reconstructed using transmission data.

To increase the number of grains indexed by GrainSpotter, one could remove the profile of the powder rings from the diffraction data, and then apply a lower threshold cut for the peak intensities. This would also enable reconstruction of the shape of smaller grains.

8

Conclusions and outlook

Contents

THIS thesis presented time-of-flight 3DND, a new neutron imaging technique to study the 3D shape and orientation of the grains composing polycrystalline materials.

In this Chapter conclusions are drawn (Sec. 8.1), followed by suggestions for potential use of the technique. In the outlook section (Sec. 8.2), we suggest which technical improvements would benefit 3DND in the next decade, and how the developed solutions could be transferred back to the X-ray world.

8.1 CONCLUSION

Compared with X-rays, neutrons have the advantage of being able to image light elements (such as lithium, a key component for energy materials, which is almost invisible to X-rays), and to penetrate heavy elements. Moreover, they can be used to study thicker samples. While with X-rays the typical sample diameter is in the millimeter range, with neutrons it can be in the centimeter range.

As described in Ch. 4, we developed two 3DND methodologies, each with different setup requirements. In both cases, a time-of-flight neutron beam with

sufficient flux is necessary. Methodology I, which requires an MCP detector and a rotation stage, can be implemented at any time-of-flight imaging beamline. In methodology II, the MCP detector is combined with high-coverage diffraction detectors. For both methodologies, exploratory simulations can be performed using the McStas polycrystalline module also developed in this thesis.

Thanks to its minimal setup requirements, methodology I can be used in combination with complicated sample environments, which may end up shielding eventual diffraction detectors. Although feasibility of methodology II has been established, in this thesis work we could not prove its advantages, in terms of reconstruction details. However, by doing more careful data normalization and background subtraction, e.g. removing the powder rings from the small iron grains, it is likely that methodology II will result in reconstructing small grains that can be difficult to observe using the MCP detector alone.

8.1.1 COMPARISON WITH nDCT

The first grain map of a sample studied using a neutron beam was obtained by S. Peetermans et al. in 2014 based on the data collected at PSI [Peetermans et al., 2014]. In their work, they illuminated an aluminium sample using a continuous, polychromatic beam and collected the diffracted beam in backscattering Laue mode. Both shape and orientation of the crystals were retrieved from the diffracted signal, using a combination of the algorithms developed for DCT and for grain mapping with X-ray laboratory sources [Ludwig et al., 2009, Reischig et al., 2013, King et al., 2013].

To limit spot overlapping, Peetermans et al. acquired data in two scans, respectively centered around 3.7 Åand 4.3 Å, so to collect diffraction spots relative to the (111) and (200) reflection [Peetermans et al., 2014]. At SENJU, we collected data using a much broader (and time-of-flight) wavelength interval: from 0.4 to 4.4 Å.

According to [Peetermans et al., 2014], the number and size of the grains that can be reconstructed using nDCT is limited by

- Diffraction spots overlapping: all diffraction spots relative to different grains are recorded in the same frame. The effect is worsen by the large bandwidth of the incoming beam ($\Delta\lambda/\lambda \simeq 15\%$). Spots overlapping limits to a few tens the total number of grains that can be detected (in the reported case, 12 were reconstructed).

- Signal-to-noise ratio in the collected data, which sets to 1 millimeter the lower limit for the grains size.

8.1.2 POTENTIAL USERS

Now that the feasibility of 3DND has been established, the technique is available to researchers from different fields. In particular, our hope is that material scientists and geologists will add 3DND to their toolbox, increasing the arsenal of techniques they can use to obtain 3D information.

- For the material scientist, 3DND is a new tool to study, nondestructively, shape and orientation of grains in the hundreds of microns to millimetre scale. Taking inspiration from 3DXRD, 3DND could be used to study how polycrystalline samples evolve under pressure and how cracks propagate [Merkel et al., 2010, Herbig et al., 2011]. Moreover, 3DND can map the evolution (before and after loading) of the grain structure in shape memory alloys, as NiTi or Co-Ni-Ga (for our reconstruction of an unloaded Co-Ni-Ga sample, see 6.28). As a result of the penetration capabilities of the neutron, materials innaccessible to X-rays could be studied, such as tungsten (W). With a high melting point and high thermal conductivity, tungsten is a promising material for facing plasma in fusion reactors [Khripunov et al., 2015, Holtkamp et al., 2007, Motojima, 2015]. To test the usability of tungsten, 3DND could be used to study how its grain structure evolves under extreme conditions.

- For the scientist interested in techniques development within neutron imaging, 3DND is a new, diffraction-based, tomography and indexing technique that could be used in combination with other neutron imaging techniques such as Bragg-edge tomography (for randomly oriented grains below the detection limit) or 3D imaging of magnetic domains [Woracek et al., 2015, Kardjilov et al., 2008]. The output of the suggested combinations would be multidimensional 3D maps showing, on top of the grain shape and orientation, how phase (Bragg-edge tomography) and magnetic domains (polarised neutrons) are arranged in the sample.

- 3DND can help geologist to investigate how polycrystalline structures form and evolve in nature. For example, 3DND could be used to study the structure of meteorites (see Fig. 8.1), thus provinding new data on the formation and evolution of asteroids and planetary system [Peetermans et al., 2013]. Annealed for long times, meteorites are usually made of large grains, and their 3D structure cannot be retrieved using other nondestructive techniques. Moreover, with 3DND resesrchers could map how forces are distributed in granular materials (most of the load is carried by a minority of the particles, that form so-called *force chains* [Hall and Wright,

2015, Peters et al., 2005]). Recently, force chains were investigated combining *a)* spatial information from neutron tomography (attenuation-based) with *b)* strain measurements for the different grains, obtained by focusing one by one on each of them [Wensrich et al., 2014]. With 3DND, the same studies could be done in a faster and more efficient way.

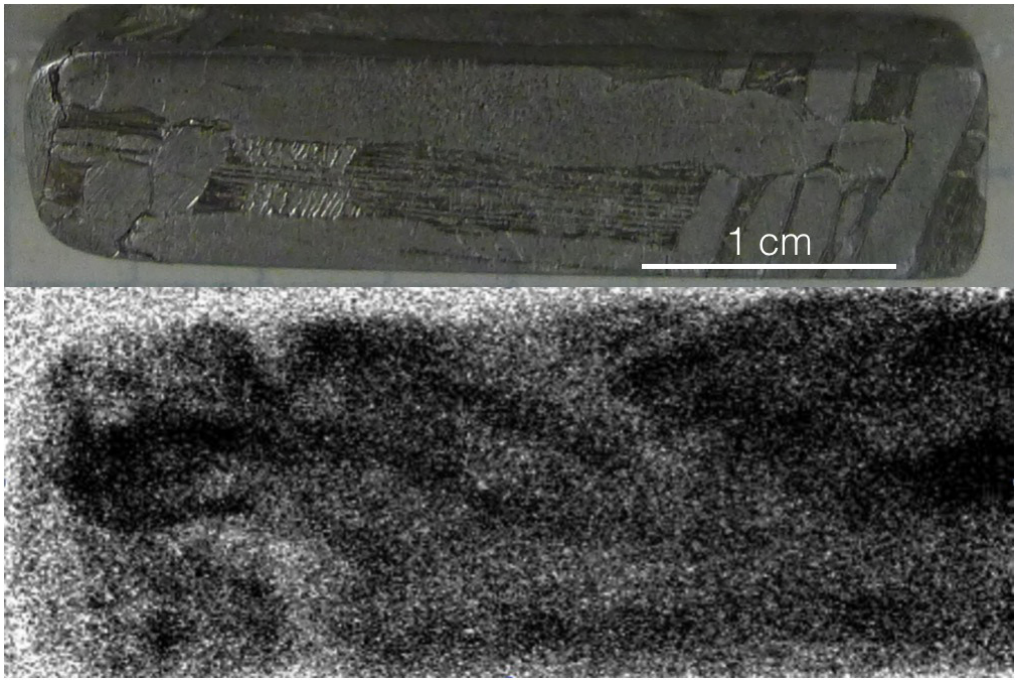

Figure 8.1: 3DND could be used to study the structure of meteorites, annealing for long time in space. Similar studies are essential to better understand the formation and evolution of asteroids and planetary system. *Top*: piece of the Seymchan meteorite, mainly composed by iron. *Bottom*: radiography, recorded at SENJU, of a section of the meteorite piece. A different scale than in the top figure is used.

8.1.3 ALGORITHMS

Developing the 3DND technique required new computer vision algorithms, such as the denoising filter Murofi and the criterion to compare shapes based on angular parameters. These solutions are general and could be applied to different areas in science and industry where standard segmentation approaches fail.

8.2 OUTLOOK

In terms of spatial resolution and of acquisition time, the performance of ToF 3DND depends on the pixel size of the different detectors and on the flux of the beam illuminating the sample. In this Section we present how ToF 3DND should improve within the next decade, considering a constant development pace for detectors and neutron sources. Later, a possible solution to increase spatial resolution using current detectors is presented. As usual, it's hard to make predictions, especially about the future[1].

8.2.0.1 Algorithms development

In the reconstruction algorithms developed in this thesis work, the shape of the grains were reconstructed by backprojecting the relative extinction spots. More advanced solutions, such as Algebraic Reconstruction Techniques (ART), could return more realistic grain shapes and would help improving spatial resolution [Gordon et al., 1970].

8.2.0.2 Detectors developments

In the next few years, the spatial resolution of the MCP detector used in transmission mode is expected to improve from the current 55 μm to $\sim$ 12.6 μm thanks to the new TimePix chip [Tremsin, 2016]. While the actual pixel size will remain constant, measuring the centroid of the incoming neutrons will enable to reduce the effective pixel size by about four times. This will lead to higher resolution 3DND reconstructions. The 3DND algorithms developed in this thesis do not depend on the number of grains considered, and with minor adjustements several hundred grains could be reconstructed. Moreover, both indexing techniques presented in Ch. 7 could still be used:

- For the procedure based on transmission data, having more extinction spots would help data-fitting in the $\omega\lambda$-plane
- For the procedure based on diffraction data, GrainSpotter succesfully indexes several thousand grains [Schmidt, 2014].

In principle, the 3D shape of the grains could also be retrieved from the diffraction data, in analogy to what is routinely done in 3DXRD [Poulsen, 2012] and to what S. Peetermans et al. have done at PSI using a non time-resolved

[1] This traditional Danish saying was one of Niels Bohr's favourites.

neutron beam [Peetermans et al., 2014]. At present this solution does not seem feasible: the far-field detectors used at SENJU have a pixel size of 4 mm, two orders of magnitude bigger than the pixels in the near-field detector.

For a given wavelength range, the near-field detector can return a maximum of 3100 frames, each corresponding to a wavelength interval Λ_i (the limit is set by the 32-bit Pixelman interface of the MCP) [Turecek et al., 2011, Tremsin, 2016]. In the measurements for the Fe and the Co-Ni-Ga sample, we considered 2423 and 2500 Λ_i intervals, each resulting in a different image. A finer sampling would help improve the spatial resolution of the 3D reconstruction: the more the intervals (compatibly with the signal-to-noise ratio), the closer one can get to the wavelength where Bragg diffraction happens.

The MCP detector could also be configured to consider a subset of the incoming wavelengths, thus obtaining a finer time-of-flight resolution. This improvement could enable measuring strain in individual grains.

8.2.0.3 Flux increase

At the time of writing (May 2016) the spallation source providing the highest beam power is SNS in the US, with 1 MW [sns,]. MLF at J-PARC is designed to provide the same beam power, and is ramping up towards it [Ikeda, 2009]. ESS, now under construction, is expected to provide a 5 MW beam from 2020 [Peggs et al., 2013]. Time-of-flight 3DND, whose algorithms were developed analysing the data collected illuminating the Fe rod with a 0.4 MW beam, will benefit from these power (and hence flux) increases, which will improve the spatial resolution and reduce the acquisition times.

A higher flux could be used to *a)* improve the signal-to-noise ratio in the transmission data, enabling to detect extinction spots more accurately than we did and hence improving the spatial resolution, or *b)* reduce the exposure time (one hour per angle for the Fe sample studied using a 0.4 MW beam). In the latter case, the time gained could be used to investigate the sample at more angles, improving the reconstruction quality, or to do more tomographic measurements, i.e. mapping time evolution of 3D grain structures under strain. Ultimately, the power of future spallation sources such as ESS will permit to both improve the spatial resolution of the reconstruction and reduce the acquisition time per angle.

8.2.0.4 The ESS case

Using a conservative approach, at ESS a ToF 3DND experiment will be between 2.5 and 5 times faster than the one reported in this thesis, done at J-PARC with a 0.4 MW beam power (acquisition time: one hour per angle) [Strobl, 2016]. The

improvement will be mainly due to the higher beam power and the innovative features of the moderator [Peggs et al., 2013, Andersen, 2015].

8.2.0.5 Progressive zooming

As explained above, smaller pixels are essential to improve the spatial resolution of 3DND reconstructions. The problem could also be attacked laterally, developing a set of lenses to zoom inside a given sample region and return detailed information about grain shapes and orientations in the considered volume. In this way the *de facto* sample volume is reduced and no detector improvements are required. The solution would be the neutron version of *dark-field X-ray microscopy*, a recently introduced technique that can study shape, orientation and strain on lengths scales from 100 nm to 1 mm within embedded sampling volumes [Simons et al., 2015]. The zooming system could be produced using optics with reduced chromatic aberration, as presented in [Poulsen et al., 2014].

8.2.0.6 Energy dispersive X-ray detectors

In ToF 3DND, the energy of the collected neutrons is calculated from their time of arrival on the detector. Energy dispersive detectors, now under development, will return similar information for X-rays (they measure the energy of the collected photons) [Amp, 2016]. With energy dispersive detectors, 3DND algorithms could be adopted at synchrotron sources, where collimated beams are available. The main limitations to get competitive energy dispersive X-ray detectors are, first and foremost, the size of the pixels, and then the energy resolution [Poulsen, 2016].

APPENDIX A

McStas simulation of the experiment at BL18

Contents

THIS is the McStas code used to simulate experiments at BL18, J-PARC. The code runs with McStas 2.1 [Willendrup et al., 2014b]. As a sample, a simulated iron cylinder made of 20 grains was used.

These are the files used in the simulations. For a schematic view, see Fig. A.1.

- The core file is `BL18_pxtal.instr`, describing the experimental setup used at beamline BL18. I developed the code in collaboration with E. Knudsen and P. Willendrup, basing on the code written by K. Oikawa to optimise the parameters of the beamline components [Tamura et al., 2012]. The description of the far-field detectors is contained in a separate file,
  `detector_arms.instr`. The instrument file takes, as inputs, a description of the J-PARC source
  (`source_BL18.txt`), and files describing the sample structure and characteristics (`Fe.lau`, `default.map_101x101_rectified` and
  `default.orts`). To save the simulation output in the same formats used by the near- and far-field detector at BL18, the instrument file uses the new components `FITS_monitor_new.comp` and `HDB_monitor_new.comp`, developed by E. Knudsen. To speed-up the computational time, versions of `BL18_pxtal.instr` with, respectively, only the near- or the far-field detectors installed have been used.

- `source_BL18.txt` lists the neutron flux from the J-PARC source at different energies.
- A Laue pattern file (`Fe.lau`) lists the reflections for iron. The file was generated using Crystallographica and is formatted as [h k l Mulitplicity d-spacing 2Theta F-squared] [Siegrist, 1997, Cereser and Willendrup, 2014, Willendrup et al., 2014a].
- `default.map_101x101_rectified` lists the position and orientations of the 100x100x100 voxels composing the simulated sample. To make the sample, I selected 20 random points inside a cube, built the corresponding 3D Delunay tessellation, extracted a cylinder and assigned a random orientation to each region [Okabe et al., 2009]. The point distribution was generated using `Voro++` [Rycroft, 2009].
- `default.orts` lists the orientations of the different Delunay regions.
- `FITS_monitor_new.comp` saves the output of the simulated MCP monitor as fits files, that is the same format used by the near-field detector at BL18.
- `HDB_monitor_new.comp` saves the output of the far-field detectors as hdp files, accepted as an input by `STARGazer` [Ohhara et al., 2009].

The scripts are available at https://github.com/albusdemens/McStas_3DND.

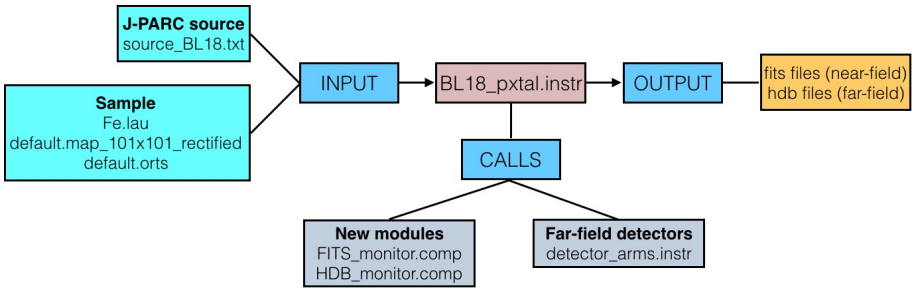

Figure A.1: Structure of the McStas simulation used to cross-check the algorithms developed analysing data collected at BL18 via ToF 3DND. The main file of the simulation, describing the beamline geometry, is `BL18_pxtal.instr`.

A.1 BL18_PXTAL.INSTR

```
/*******************************************************************************
*
* Written by: A. Cereser and E. Knudsen
* Based on code by K. Oikawa
* September 2013 - February 2016
* Written at DTU and J-PARC
*
* Instrument: BL18 SENJU at J-PARC
*
* mcstas ./BL18_pxtal_event.instr
*
* %P
* L_min (AA) lower edge of wavelength band to be emitted from the Source
* L_max (AA) upper edge of wavelength band to be emitted from the Source
* NX ( ) Number of voxels along X
* NY ( ) Number of voxels along Y
* NZ ( ) Number of voxels along Z
* XW (m) Width of the polycrystal hull.
* YH (m) Height of the polycrystal hull
* ZD (m) Depth og the polycrystal hull
* map_fn ( ) name of file containing the orientation map
* orts_fn ( ) name of file containing orientations
* lau_fn ( ) name of file ocntaining the reflection list
* AX ( ) X-component of unit cell vector a
* ...
* CZ ( ) Z-component of unit cell vector c
* samplename ( ) name of the sample to produce SENJU style filenames
* runnumber ( ) runnumber to produce SENJU style filenames
*
* These are some lines from the original J-parc simulation
*         E_min=81.8049/lmax/lmax;
*         E_max=81.8049/lmin/lmin;
*         tof_min=dd*505.555*35.6*sin((TTT)/360*PI)-delt;
*         tof_max=dd*505.555*35.6*sin((TTT)/360*PI)+delt;
*         E_min=81.8049*(252.778*35.6/tof_max)*(252.778*35.6/tof_max);
*         E_max=81.8049*(252.778*35.6/tof_min)*(252.778*35.6/tof_min);
*
*******************************************************************************/
DEFINE INSTRUMENT BL18_SENJU(L_min=0.4, L_max=4, NX=1, NY=1, NZ=1, XW=0.01,
    YH=0.01, ZD=0.01, string map_fn="default.map_101x101_rectified",
    string orts_fn="default.orts",string lau_fn="Fe.lau",
    AX = 2.886,AY = 0, AZ = 0.0, BX = 0.0, BY = 2.886, BZ = 0.0, CX = 0.0,
    CY = 0.0, CZ = 2.886,omega=0, string samplename="C0127", int runnumber=0,
    int side=0
)

DECLARE
%{
  double lmin, lmax, E_min, E_max, tof_min, tof_max;
  double TTS, UML;
  double dd, delt;
  double shtwin, shthin, shtwout, shthout, nchann;
  double ddd, mos, ndd, detx;
  double alpha,wsht, Pi, nD, m5;
  double TG, TG1, TG2, TG3, TG4;
  double mx_Vd, my_Vd;
  double dsp, lam, lw, TT, TTT, TTD;
  double tt0,tt1;
```

```
59    double ux,uy,uz;
60    double kux,kuy,kuz;
61    double anx,any,anz;
62    int xtal_scatter;
63    char crystal_file[]="Al.lau";
64    //the crystal files are in /usr/local/lib/mcstas-2.0/data
65
66    void compute_global_vector(char *s,double kx,double ky, double kz,double *gkx,
67    double *gky, double *gkz, Rotation R){
68      Rotation TT;
69      rot_transpose(R, TT);
70      /* now make the coordinate system change */
71      coords_get(rot_apply(TT,coords_set(kx,ky,kz)),gkx,gky,gkz);
72    }
73
74    void compute_global_coords(char *s,double x,double y,double z,double *gx,
75    double *gy,double *gz,Coords A,Rotation R){
76      Rotation TT;
77      rot_transpose(R, TT);
78      /* now make the coordinate system change */
79      coords_get(coords_add(rot_apply(TT,coords_set(x,y,z)),A),gx,gy,gz);
80    }
81    int sx_scatter;
82    int anton;
83    int oidx;
84
85    long long nid;
86
87    /*The lines below have been added to deal with the polycrystalline sample*/
88    %include "read_table-lib.h"
89    int nx;                /*Number of voronoi regions in each direction*/
90    int ny;                /*The number has to be the same in pixellation.m */
91    int nz;
92    int ix,iy,iz,crystal_miss;
93    int xtals;
94
95    double posx,posy,posz;
96
97    t_Table *map_table,*orts_table;
98
99    Coords ao,bo,co;
100
101   /*heres where we store the orientation dependent hkl_info pointers*/
102   struct hkl_info_struct *poly_hkl_info;
103   int initd;
104
105   int sx_background;
106   /*flag to indicate whether or not this is a void in the crystal*/
107
108   char det_fn[41][256];
109   char *det_fn_001=det_fn[1];
110   char *det_fn_002=det_fn[2];
111   char *det_fn_003=det_fn[3];
112   char *det_fn_004=det_fn[4];
113   char *det_fn_005=det_fn[5];
114   char *det_fn_006=det_fn[6];
115   char *det_fn_007=det_fn[7];
116   char *det_fn_008=det_fn[8];
117   char *det_fn_009=det_fn[9];
```

```
118     char *det_fn_010=det_fn[10];
119     char *det_fn_011=det_fn[11];
120     char *det_fn_012=det_fn[12];
121     char *det_fn_013=det_fn[13];
122     char *det_fn_014=det_fn[14];
123     char *det_fn_015=det_fn[15];
124     char *det_fn_016=det_fn[16];
125     char *det_fn_017=det_fn[17];
126     char *det_fn_018=det_fn[18];
127     char *det_fn_019=det_fn[19];
128     char *det_fn_020=det_fn[20];
129     char *det_fn_021=det_fn[21];
130     char *det_fn_022=det_fn[22];
131     char *det_fn_023=det_fn[23];
132     char *det_fn_024=det_fn[24];
133     char *det_fn_025=det_fn[25];
134     char *det_fn_026=det_fn[26];
135     char *det_fn_027=det_fn[27];
136     char *det_fn_028=det_fn[28];
137     char *det_fn_029=det_fn[29];
138     char *det_fn_030=det_fn[30];
139     char *det_fn_031=det_fn[31];
140     char *det_fn_032=det_fn[32];
141     char *det_fn_033=det_fn[33];
142     char *det_fn_034=det_fn[34];
143     char *det_fn_035=det_fn[35];
144     char *det_fn_036=det_fn[36];
145     char *det_fn_037=det_fn[37];
146     char *det_fn_038=det_fn[38];
147     char *det_fn_039=det_fn[39];
148     char *det_fn_040=det_fn[40];
149
150   %}
151
152   INITIALIZE
153   %{
154     Pi=3.14159;
155     alpha=3.0;
156     wsht=3e-3;
157
158     /*Section below added to work with the polycrystalline sample*/
159
160     /*These should come from analyzing the map file instead*/
161     nx=NX;
162     ny=NY;
163     nz=NZ;
164
165
166     /*Force components initialization to avoid inifite recursion*/
167     if (initd!=1){
168       initd=1;
169       mcinit();
170
171       int status;
172       map_table=malloc(sizeof(t_Table));
173       orts_table=malloc(sizeof(t_Table));
174
175       if ( (status=Table_Read(orts_table,orts_fn,0))==-1){
176         fprintf(stderr,"Error (%s): Could not parse file \"%s\"\n",
```

```
177         NAME_CURRENT_COMP,orts_fn);
178         exit(-1);
179       }
180       if ( (status=Table_Read(map_table,map_fn,0))==-1){
181         fprintf(stderr,"Error (%s): Could not parse file \"%s\"\n",
182         NAME_CURRENT_COMP,map_fn);
183         exit(-1);
184       }
185
186       ao=coords_set(MC_GETPAR2(SX,ax),MC_GETPAR2(SX,ay),MC_GETPAR2(SX,az));
187       bo=coords_set(MC_GETPAR2(SX,bx),MC_GETPAR2(SX,by),MC_GETPAR2(SX,bz));
188       co=coords_set(MC_GETPAR2(SX,cx),MC_GETPAR2(SX,cy),MC_GETPAR2(SX,cz));
189
190       /*allocate memory for all orientation hkl_infos*/
191       if( (poly_hkl_info=malloc(orts_table->rows*sizeof(struct hkl_info_struct)))==NULL ){
192           fprintf(stderr,"Error (%s): Memory allocation error for orts hkl_infos,
193           aborting.\n",NAME_CURRENT_COMP);
194           exit(-1);
195       }
196
197       /*get important parameters from actual component*/
198       char *laufn=MC_GETPAR2(SX,reflections);
199       double SC_mosaic=MC_GETPAR2(SX,mosaic);
200       double SC_mosaic_a=MC_GETPAR2(SX,mosaic_a);
201       double SC_mosaic_b=MC_GETPAR2(SX,mosaic_b);
202       double SC_mosaic_c=MC_GETPAR2(SX,mosaic_c);
203       double *SC_mosaic_ABin=NULL;
204
205       /*loop over all orientations and set up info-lists for each one.*/
206       int i;
207       for (i=0;i<orts_table->rows;i++){
208         poly_hkl_info[i]=MC_GETPAR2(SX,hkl_info);
209         /*by def. we are dealing with crystal prms. in real space*/
210         poly_hkl_info[i].recip=0;
211
212         /*apply rotation to crystal vectors*/
213         Coords a,b,c;
214         Rotation U;
215         memcpy(*U,&(orts_table->data[i*9]),sizeof(U[0][0])*9);
216         a=rot_apply(U,ao);
217         b=rot_apply(U,bo);
218         c=rot_apply(U,co);
219         /*set the crystal parameters to the rotated ones*/
220         coords_get(a,&(poly_hkl_info[i].m_ax), &(poly_hkl_info[i].m_ay),
221         &(poly_hkl_info[i].m_az));
222         coords_get(b,&(poly_hkl_info[i].m_bx), &(poly_hkl_info[i].m_by),
223         &(poly_hkl_info[i].m_bz));
224         coords_get(c,&(poly_hkl_info[i].m_cx), &(poly_hkl_info[i].m_cy),
225         &(poly_hkl_info[i].m_cz));
226
227         /*call read_hkl_list function*/
228         if (!read_hkl_data(laufn, &(poly_hkl_info[i]), SC_mosaic, SC_mosaic_a,
229         SC_mosaic_b, SC_mosaic_c, SC_mosaic_ABin))
230           exit(-1);
231
232
233       }
234       /*This should only be done once*/
235       /*adjust the tunnelling probability to avoid statistical extinction*/
```

```
236       int nmax;
237       if (NX>NY) nmax=NX;
238       else nmax=NY;
239       if(nmax<NZ) nmax=NZ;
240
241       MC_GETPAR2(SX,p_transmit)=exp(log(MC_GETPAR2(SX,p_transmit))/(double)nmax);
242       /*end of polycrystal*/
243
244       return;
245       /*do other initialization stuff*/
246     }else{
247       /*this block gets done before component initialization*/
248       /*set up detector filenames*/
249
250       int j;
251       for (j=1;j<=40;j++){
252         sprintf(det_fn[j],"%s_%06d_%03d",samplename,runnumber,j);
253         if(j==1){
254           printf("detector filenames:\n%s\n .\n .\n .\n",det_fn[j]);
255         }else if(j==40){
256           printf("%s\n",det_fn[j]);
257         }
258       }
259
260       /*position SENJU far field detectors according to calibration*/
261
262     }
263   %}
264
265   TRACE
266
267   COMPONENT Origin = Progress_bar()
268     AT (0,0,0) ABSOLUTE
269   EXTEND
270   %{
271    anton=0;
272    xtals=0;
273    nid=mcget_run_num();
274    //printf("%ld\n",nid);
275
276   %}
277
278   COMPONENT a1 = Arm()
279     AT (0,0,0) ABSOLUTE
280
281   COMPONENT mod = SNS_source(
282     filename="source_BL18.txt",
283     xwidth=0.1, yheight=0.1,
284     dist = 15.19,
285     focus_xw = 0.041, focus_yh = 0.041,
286     Emax=pow((2*M_PI/L_min)*K2V,2.0)*VS2E, Emin=pow((2*M_PI/L_max)*K2V,2.0)*VS2E
287   ) AT (0,0,0) RELATIVE a1
288
289   /*Uncomment the section below to get a pencil beam
290
291   COMPONENT mod=Modr_dcHPb_flux(
292           xws=0.1, yhs=0.1, angle=0.0,
293           Emin=E_min, Emax=E_max,
294     dist = 15.19,
```

```
295     xw = 0.041, yh = 0.041
296   ) AT (0,0,0)  RELATIVE a1
297   */
298
299   COMPONENT slt_in = Slit(
300           xwidth = 0.070, yheight = 0.070)
301           AT (0, 0, 2.271) RELATIVE a1
302
303   COMPONENT slt_out = Slit(
304           xwidth = 0.044, yheight = 0.044)
305           AT (0, 0, 15.140) RELATIVE a1
306
307   COMPONENT guide1 = Guide(w1=0.03951,
308                            h1=0.03951,
309                            w2=0.04146,
310                            h2=0.04146,
311                            l=0.8-0.0000001, R0=0.99, Qc=0.0217, alpha=4,m=4.0,W=0.0015)
312                            AT (0, 0, 15.2) RELATIVE a1 ROTATED (0,0,0) RELATIVE a1
313
314   COMPONENT guide2 = Guide(w1=0.04146,
315                            h1=0.04146,
316                            w2=0.04347,
317                            h2=0.04347,
318                            l=1.0-0.0000001, R0=0.99, Qc=0.0217, alpha=3,m=3.2,W=0.001)
319                            AT (0, 0, 16.0) RELATIVE a1 ROTATED (0,0,0) RELATIVE a1
320
321   COMPONENT guide3 = Guide(w1=0.04347,
322                            h1=0.04347,
323                            w2=0.04507,
324                            h2=0.04507,
325                            l=1.0-0.0000001, R0=0.99, Qc=0.0217,  alpha=3,m=3.2,W=0.001)
326                            AT (0, 0, 17.0) RELATIVE a1 ROTATED (0,0,0) RELATIVE a1
327
328   COMPONENT guide4 = Guide(w1=0.04507,
329                            h1=0.04507,
330                            w2=0.04630,
331                            h2=0.04630,
332                            l=1.0-0.0000001, R0=0.99, Qc=0.0217, alpha=3,m=3.2,W=0.001)
333                            AT (0, 0, 18.0) RELATIVE a1 ROTATED (0,0,0) RELATIVE a1
334
335   COMPONENT guide5 = Guide(w1=0.04630,
336                            h1=0.04630,
337                            w2=0.04718,
338                            h2=0.04718,
339                            l=1.0-0.0000001, R0=0.99, Qc=0.0217, alpha=3,m=3.2,W=0.001)
340                            AT (0, 0, 19.0) RELATIVE a1 ROTATED (0,0,0) RELATIVE a1
341
342   COMPONENT guide6 = Guide(w1=0.04718,
343                            h1=0.04718,
344                            w2=0.04774,
345                            h2=0.04774,
346                            l=1.0-0.0000001, R0=0.99, Qc=0.0217,  alpha=3,m=3.2,W=0.001)
347                            AT (0, 0, 20.0) RELATIVE a1 ROTATED (0,0,0) RELATIVE a1
348
349   COMPONENT guide7 = Guide(w1=0.04774,
350                            h1=0.04774,
351                            w2=0.04799,
352                            h2=0.04799,
353                            l=1.0-0.0000001, R0=0.99, Qc=0.0217,  alpha=3,m=3.2,W=0.001)
```

```
                          AT (0, 0, 21.0) RELATIVE a1 ROTATED (0,0,0) RELATIVE a1

  COMPONENT guide8 = Guide(w1=0.04799,
                          h1=0.04799,
                          w2=0.04799,
                          h2=0.04799,
                          l=0.6-0.0000001, R0=0.99, Qc=0.0217,  alpha=3,m=3.2,W=0.001)
                          AT (0, 0, 22.0) RELATIVE a1 ROTATED (0,0,0) RELATIVE a1

  COMPONENT guide9 = Guide(w1=0.04799,
                          h1=0.04799,
                          w2=0.04774,
                          h2=0.04774,
                          l=1.0-0.0000001, R0=0.99, Qc=0.0217,  alpha=3,m=3.2,W=0.001)
                          AT (0, 0, 22.6) RELATIVE a1 ROTATED (0,0,0) RELATIVE a1

  COMPONENT guide10 = Guide(w1=0.04774,
                          h1=0.04774,
                          w2=0.04718,
                          h2=0.04718,
                          l=1.0-0.0000001, R0=0.99, Qc=0.0217,  alpha=3,m=3.2,W=0.001)
                          AT (0, 0, 23.6) RELATIVE a1 ROTATED (0,0,0) RELATIVE a1

  COMPONENT guide11 = Guide(w1=0.04718,
                          h1=0.04718,
                          w2=0.04630,
                          h2=0.04630,
                          l=1.0-0.0000001, R0=0.99, Qc=0.0217,  alpha=3,m=3.2,W=0.001)
                          AT (0, 0, 24.6) RELATIVE a1 ROTATED (0,0,0) RELATIVE a1

  COMPONENT guide12 = Guide(w1=0.04630,
                          h1=0.04630,
                          w2=0.04507,
                          h2=0.04507,
                          l=1.0-0.0000001, R0=0.99, Qc=0.0217,  alpha=3,m=3.2,W=0.001)
                          AT (0, 0, 25.6) RELATIVE a1 ROTATED (0,0,0) RELATIVE a1

  COMPONENT guide13 = Guide(w1=0.04507,
                          h1=0.04507,
                          w2=0.04347,
                          h2=0.04347,
                          l=1.0-0.0000001, R0=0.99, Qc=0.0217,  alpha=3,m=3.2,W=0.001)
                          AT (0, 0, 26.6) RELATIVE a1 ROTATED (0,0,0) RELATIVE a1

  COMPONENT guide14 = Guide(w1=0.04347,
                          h1=0.04347,
                          w2=0.04146,
                          h2=0.04146,
                          l=1.0-0.0000001, R0=0.99, Qc=0.0217,  alpha=3,m=3.2,W=0.001)
                          AT (0, 0, 27.6) RELATIVE a1 ROTATED (0,0,0) RELATIVE a1

  COMPONENT guide15 = Guide(w1=0.04146,
                          h1=0.04146,
                          w2=0.03840,
                          h2=0.03840,
                          l=1.2-0.0000001, R0=0.99, Qc=0.0217, alpha=4,m=4.0,W=0.0015)
                          AT (0, 0, 28.6) RELATIVE a1 ROTATED (0,0,0) RELATIVE a1

  COMPONENT guide16 = Guide(w1=0.03840,
```

```
                          h1=0.03840,
                          w2=0.03519,
                          h2=0.03519,
                          l=1.0-0.0000001, R0=0.99, Qc=0.0217, alpha=4,m=4.0,W=0.0015)
                          AT (0, 0, 29.8) RELATIVE a1 ROTATED (0,0,0) RELATIVE a1

COMPONENT guide17 = Guide(w1=0.03519,
                          h1=0.03519,
                          w2=0.03120,
                          h2=0.03120,
                          l=1.0-0.0000001, R0=0.99, Qc=0.0217, alpha=4,m=4.0,W=0.0015)
                          AT (0, 0, 30.8) RELATIVE a1 ROTATED (0,0,0) RELATIVE a1

COMPONENT slt1 = Slit(
        xwidth = 0.0292, yheight = 0.035)
AT (0, 0, 31.845) RELATIVE a1 /*31.8624 given by present J-PARC staff*/

COMPONENT slt2 = Slit(
    xwidth = 0.0115, yheight = 0.022)
AT (0, 0, 33.615) RELATIVE a1 /*33.6274 measured by J-PARC staff*/

/******************/
/*sample position*/
/******************/

COMPONENT psdsamp = PSD_monitor(
 xwidth = 0.0512, yheight = 0.0512,restore_neutron=1,
 nx = 128, ny = 128, filename = "PSD_samp.txt"
) AT (0,0,34.8025) RELATIVE a1

COMPONENT tofsampl = TOF_monitor(
  xwidth=0.0512, yheight=0.0512, restore_neutron=1, nt=2424, tmin=1, tmax=40000,
  filename="TOF_samp.txt"
) AT (0,0,0) RELATIVE PREVIOUS

COMPONENT lsamp = L_monitor(
  xwidth=0.0512, yheight=0.0512, restore_neutron=1,Lmin=0, Lmax=20, nL=100,
  filename="L_samp.txt"
)AT (0,0,0)RELATIVE PREVIOUS

SPLIT 20 COMPONENT splitpoint = Arm()
AT(0,0,0) RELATIVE PREVIOUS
EXTEND
%{
 ix=iy=iz=-1;
%}

COMPONENT sx_hull=Arm()
AT(0,0,0) RELATIVE PREVIOUS
ROTATED (0,omega,0) RELATIVE Origin
EXTEND
%{
  do {
    double xw,yh,zd;
    xw=nx*MC_GETPAR2(SX,xwidth);
    yh=ny*MC_GETPAR2(SX,yheight);
    zd=nz*MC_GETPAR2(SX,zdepth);
    crystal_miss=0;
    int s;//,oidx;
```

```
472       double t0,t1;
473       if ( (s=box_intersect(&t0,&t1,x,y,z,vx,vy,vz,xw,yh,zd) )){
474         /*miss crystal hull or already past it*/
475         if(s==0 || t1<=0){
476           crystal_miss=1;
477           break;
478         }
479
480         if(t0>0){
481           PROP_DT(t0+DBL_EPSILON);
482         }
483         /*find out which subcrystal we hit. The dbl_eps are there to protect
484          against rounding errors which may occur in the propagation routines so
485          the neutron does not switch to the next subcrystal*/
486         int iix,iiy,iiz;
487         iix = floor((x + xw*0.5)*nx/xw);
488         iiy = floor((y + yh*0.5)*ny/yh);
489         iiz = floor((z + zd*0.5)*nz/zd);
490         if (iiz==nz || iiz<0 || iix==nx || iix<0 || iiy==ny || iiy<0 ){
491           /*Neutron is outside the crystal hull. This should never happen*/
492           fprintf(stderr,"Warning (%s): Neutron has unpxectedly left the crystal
493           hull: (ix,iy,iz) = (%d %d %d) (x,y,z)=(%g %g %g). Terminating\n",
494           NAME_CURRENT_COMP,iix,iiy,iiz,x,y,z);
495           ABSORB;
496         }
497         /*avoid getting stuck on a boundary*/
498         int count=0;
499         if(iix == ix && iiy==iy && iiz==iz){
500           /*neutron is still in the same voxel as before - move it to enter the
501            next one.*/
502           //fprintf(stderr,"I am stuck...hopping to try to get unstuck.\n");
503           //fprintf(stderr,"ix,iy,iz= %d %d %d nid=%ld\n",ix,iy,iz,nid);
504           PROP_DT(DBL_EPSILON*10.0);
505           iix = floor((x + xw*0.5)*nx/xw);
506           iiy = floor((y + yh*0.5)*ny/yh);
507           iiz = floor((z + zd*0.5)*nz/zd);
508           if(iix == ix && iiy==iy && iiz==iz){
509             fprintf(stderr,"I am still stuck...terminating neutron.\n");
510             ABSORB;
511           }
512         }
513
514         ix=iix;iy=iiy;iz=iiz;
515
516         //SCATTER;
517
518         /*inject the right hkl_info struct and carry over the "old" neutron ki*/
519         /* to skip the orientation search.*/
520         /*orientation index is in the 4th col of map_table. -1 since array is*/
521         /*zero-indexed.*/
522         oidx=Table_Index(*map_table,ix*(ny*nz)+iy*nz+iz,3)-1;
523         double kix_carry=MC_GETPAR(SX,hkl_info).kix;
524         double kiy_carry=MC_GETPAR(SX,hkl_info).kiy;
525         double kiz_carry=MC_GETPAR(SX,hkl_info).kiz;
526         MC_GETPAR(SX,hkl_info)=(poly_hkl_info[oidx]);
527         MC_GETPAR(SX,hkl_info).kix=kix_carry;
528         MC_GETPAR(SX,hkl_info).kiy=kiy_carry;
529         MC_GETPAR(SX,hkl_info).kiz=kiz_carry;
530
```

```
531         posx=(ix-nx*0.5+.5)*xw/nx;
532         posy=(iy-ny*0.5+.5)*yh/ny;
533         posz=(iz-nz*0.5+.5)*zd/nz;
534         /*translate neutron to account for crystal centre position*/
535         x-=posx;y-=posy;z-=posz;
536
537         if(oidx!=-1){
538           sx_background=0;
539         }else{
540           /*This is a void in the polycrystal*/
541           sx_background=1;
542         }
543       }else{
544         /*we miss the compound crystal completely so flag that*/
545         crystal_miss=1;
546       }
547     }while(0);
548   %}
549   JUMP sx_exit WHEN (crystal_miss)
550
551   COMPONENT SX = Single_crystal(
552       reflections = lau_fn,
553       xwidth = XW/(double)NX, yheight = YH/(double)NY,
554       zdepth = ZD/(double)NZ, delta_d_d = 0.01, mosaic = 0.01,sigma_inc=0.4,
555       sigma_abs=2.56,barns=1,
556       ax = AX, ay = AY, az = AZ, bx = BX, by = BY, bz = BZ, cx = CX,cy = CY,
557       cz = CZ,
558       p_transmit = 0.9)
559   WHEN (!sx_background) AT (0, 0, 0) RELATIVE sx_hull
560   EXTEND
561   %{
562   #ifdef MCSTAS_DEBUG
563     printf("I have gone through a crystal: scatter=%d, oidx=%d\n",mcScattered,oidx);
564   #endif
565     do {
566       if (hkl_info.type='t'){
567         //printf("COHSCATTORT: %d\n",oidx);
568       }
569       if(SCATTERED) xtals++;
570       int s;
571       double t0,t1;
572       if ( (s=box_intersect(&t0,&t1,x,y,z,vx,vy,vz,xwidth,yheight,zdepth) ) &&
573       t1>0 ){
574         PROP_DT(t1+DBL_EPSILON);
575       }
576       /*transform back to regular coordinates*/
577       x+=posx;y+=posy;z+=posz;
578       SCATTER;
579     }while(0);
580   %}
581
582   COMPONENT SX_background=Arm()
583   WHEN (sx_background) AT(0,0,0) RELATIVE sx_hull
584   EXTEND
585   %{
586   #ifdef MCSTAS_DEBUG
587     printf("I have gone through background: scatter=%d\n",mcScattered);
588   #endif
589     do {
```

```
590       int s;
591       double t0,t1;
592       if ( (s=box_intersect(&t0,&t1,x,y,z,vx,vy,vz,MC_GETPAR2(SX,xwidth),
593       MC_GETPAR2(SX,yheight),MC_GETPAR2(SX,zdepth) ) ) && t1>0 ){
594         PROP_DT(t1+DBL_EPSILON);
595       }
596       /*transform back to regular coordinates*/
597       x+=posx;y+=posy;z+=posz;
598       SCATTER;
599     }while(0);
600   %}
601
602   COMPONENT sx_exit = Arm()
603   AT(0,0,0) RELATIVE sx_hull
604   EXTEND
605   %{
606     //printf("exit miss: %d\n",crystal_miss);
607   %}
608   JUMP sx_hull WHEN (crystal_miss==0)
609
610   COMPONENT psd_direct_beam0 = PSD_monitor(
611         xwidth=XW,yheight=YH, nx=101, ny=101, filename="psd_direct_beam0",
612         restore_neutron=1)
613   AT(0,0,ZD/2.0+1e-6) RELATIVE psdsamp
614   GROUP g0
615
616   COMPONENT psd_direct_beam_arm = Arm()
617   AT(0,0,0) RELATIVE PREVIOUS
618   GROUP g0
619   EXTEND
620   %{
621       SCATTER;
622   %}
623
624   COMPONENT psd_anton = PSD_monitor(
625       xwidth=0.028, yheight=0.028, nx=301, ny=301,filename="psd_anton.dat",
626       restore_neutron=1)
627   AT(0,0,0.2) RELATIVE psdsamp
628   GROUP g1
629
630   COMPONENT psd_anton_arm = Arm()
631   AT(0,0,0) RELATIVE PREVIOUS
632   GROUP g1
633   EXTEND
634   %{
635       SCATTER;
636   %}
637   /******************/
638   /* far field detectors. u = up, d = down */
639   /****************/
640
641   %include "detector_arms.instr"
642
643   /* Here's the 4pi detector*/
644
645   COMPONENT 4pi_psd=PSD_monitor_4PI(
646       nx=301, ny=301,radius=0.2,filename="4pi_psd", restore_neutron=1
647   )
648   AT (0,0,0) RELATIVE psdsamp
```

```
649
650 COMPONENT det_014 = HDB_monitor_new(
651         xwidth=0.256, yheight=0.256, filename=det_fn_014, noextrafiles=0)
652 WHEN (side & 1) AT(0,0,0) RELATIVE det_014a
653 GROUP det
654
655 COMPONENT det_015 = COPY(det_014)(filename=det_fn_015)
656 WHEN (side & 1) AT (0,0,0) RELATIVE det_015a
657 GROUP det
658
659 COMPONENT det_013 = COPY(det_014)(filename=det_fn_013)
660 WHEN (side & 1) AT (0,0,0) RELATIVE det_013a
661 GROUP det
662
663 COMPONENT det_011 = COPY(det_014)(filename=det_fn_011)
664 WHEN (side & 1) AT (0,0,0) RELATIVE det_011a
665 GROUP det
666
667 COMPONENT det_012 = COPY(det_014)(filename=det_fn_012)
668 WHEN (side & 1) AT (0,0,0) RELATIVE det_012a
669 GROUP det
670
671 COMPONENT det_010 = COPY(det_014)(filename=det_fn_010)
672 WHEN (side & 1) AT (0,0,0) RELATIVE det_010a
673 GROUP det
674
675 COMPONENT det_008 = COPY(det_014)(filename=det_fn_008)
676 WHEN (side & 1) AT (0,0,0) RELATIVE det_008a
677 GROUP det
678
679 COMPONENT det_009 = COPY(det_014)(filename=det_fn_009)
680 WHEN (side & 1) AT (0,0,0) RELATIVE det_009a
681 GROUP det
682
683 COMPONENT det_007 = COPY(det_014)(filename=det_fn_007)
684 WHEN (side & 1) AT (0,0,0) RELATIVE det_007a
685 GROUP det
686
687 COMPONENT det_005 = COPY(det_014)(filename=det_fn_005)
688 WHEN (side & 1) AT (0,0,0) RELATIVE det_005a
689 GROUP det
690
691 COMPONENT det_006 = COPY(det_014)(filename=det_fn_006)
692 WHEN (side & 1) AT (0,0,0) RELATIVE det_006a
693 GROUP det
694
695 COMPONENT det_004 = COPY(det_014)(filename=det_fn_004)
696 WHEN (side & 1) AT (0,0,0) RELATIVE det_004a
697 GROUP det
698
699 COMPONENT det_002 = COPY(det_014)(filename=det_fn_002)
700 WHEN (side & 1) AT (0,0,0) RELATIVE det_002a
701 GROUP det
702
703 COMPONENT det_003 = COPY(det_014)(filename=det_fn_003)
704 WHEN (side & 1) AT (0,0,0) RELATIVE det_003a
705 GROUP det
706
707 COMPONENT det_001 = COPY(det_014)(filename=det_fn_001)
```

```
708  WHEN (side & 1) AT (0,0,0) RELATIVE det_001a
709  GROUP det
710
711
712  /* N monitors */
713
714  COMPONENT det_017 = HDB_monitor_new(
715          xwidth=0.256, yheight=0.256, filename=det_fn_017, noextrafiles=0)
716  WHEN (side & 2) AT(0,0,0) RELATIVE det_017a
717  GROUP det
718
719  COMPONENT det_018 = COPY(det_017)(filename=det_fn_018)
720  WHEN (side & 2) AT (0,0,0) RELATIVE det_018a
721  GROUP det
722
723  COMPONENT det_016 = COPY(det_017)(filename=det_fn_016)
724  WHEN (side & 2) AT (0,0,0) RELATIVE det_016a
725  GROUP det
726
727  COMPONENT det_020 = COPY(det_017)(filename=det_fn_020)
728  WHEN (side & 2) AT (0,0,0) RELATIVE det_020a
729  GROUP det
730
731  COMPONENT det_021 = COPY(det_017)(filename=det_fn_021)
732  WHEN (side & 2) AT (0,0,0) RELATIVE det_021a
733  GROUP det
734
735  COMPONENT det_019 = COPY(det_017)(filename=det_fn_019)
736  WHEN (side & 2) AT (0,0,0) RELATIVE det_019a
737  GROUP det
738
739  COMPONENT det_023 = COPY(det_017)(filename=det_fn_023)
740  WHEN (side & 2) AT (0,0,0) RELATIVE det_023a
741  GROUP det
742
743  COMPONENT det_024 = COPY(det_017)(filename=det_fn_024)
744  WHEN (side & 2) AT (0,0,0) RELATIVE det_024a
745  GROUP det
746
747  COMPONENT det_022 = COPY(det_017)(filename=det_fn_022)
748  WHEN (side & 2) AT (0,0,0) RELATIVE det_022a
749  GROUP det
750
751  COMPONENT det_026 = COPY(det_017)(filename=det_fn_026)
752  WHEN (side & 2) AT (0,0,0) RELATIVE det_026a
753  GROUP det
754
755  COMPONENT det_027 = COPY(det_017)(filename=det_fn_027)
756  WHEN (side & 2) AT (0,0,0) RELATIVE det_027a
757  GROUP det
758
759  COMPONENT det_025 = COPY(det_017)(filename=det_fn_025)
760  WHEN (side & 2) AT (0,0,0) RELATIVE det_025a
761  GROUP det
762
763  COMPONENT det_029 = COPY(det_017)(filename=det_fn_029)
764  WHEN (side & 2) AT (0,0,0) RELATIVE det_029a
765  GROUP det
766
```

```
COMPONENT det_030 = COPY(det_017)(filename=det_fn_030)
WHEN (side & 2) AT (0,0,0) RELATIVE det_030a
GROUP det

COMPONENT det_028 = COPY(det_017)(filename=det_fn_028)
WHEN (side & 2) AT (0,0,0) RELATIVE det_028a
GROUP det

COMPONENT det_032 = COPY(det_017)(filename=det_fn_032)
WHEN (side & 2) AT (0,0,0) RELATIVE det_032a
GROUP det

COMPONENT det_033 = COPY(det_017)(filename=det_fn_033)
WHEN (side & 2) AT (0,0,0) RELATIVE det_033a
GROUP det

COMPONENT det_031 = COPY(det_017)(filename=det_fn_031)
WHEN (side & 2) AT (0,0,0) RELATIVE det_031a
GROUP det

COMPONENT det_035 = COPY(det_017)(filename=det_fn_035)
WHEN (side & 2) AT (0,0,0) RELATIVE det_035a
GROUP det

COMPONENT det_036 = COPY(det_017)(filename=det_fn_036)
WHEN (side & 2) AT (0,0,0) RELATIVE det_036a
GROUP det

COMPONENT det_034 = COPY(det_017)(filename=det_fn_034)
WHEN (side & 2) AT (0,0,0) RELATIVE det_034a
GROUP det

COMPONENT det_037 = COPY(det_014)(filename=det_fn_037)
WHEN (side & 2) AT(0,0,0) RELATIVE det_037a
GROUP det

COMPONENT catch_all = Arm()
AT(0,0,0) RELATIVE PREVIOUS
GROUP det
EXTEND
%{
  SCATTER;
%}

COMPONENT mon_MCP = FITS_monitor_new(
        xwidth=0.028, yheight=0.028, filename="mon_MCP",short_floats=1,nx=258,
        ny=258,nt=400,tmin=1, tmax=40000,restore_neutron=1
)
WHEN (side & 4) AT(0,0,0.02) RELATIVE psdsamp
GROUP mcp

COMPONENT mon_MCP_not = Monitor_nD(
    radius=0.025, filename="mon_MCP_not",
    options="t bins=400 limits=[1e-6 40000e-6]", restore_neutron=1)
AT(0,0,0) RELATIVE psdsamp
GROUP mcp

COMPONENT mon_MCP_catchall = Arm()
AT(0,0,0) RELATIVE PREVIOUS
```

```
826  GROUP mcp
827  EXTEND
828  %{
829    SCATTER;
830  %}
831
832
833  FINALLY
834  %{
835  %}
836
837  END
```

APPENDIX B

Abstract of articles

Time-of-Flight Three Dimensional Neutron Diffraction for mapping crystal grain structures - I. Transmission detector only

Alberto Cereser Markus Strob Stephen Hall
Axel Steuwer Anton Tremsin Ryoji Kiyanagi
Takenao Shinohara Erik Bergbäck Knudsen
Peter Willendrup Alice Bastos da Silva Fanta
Peter Mahler Larsen Srinivasan Iyengar Søren Schmidt

June 1, 2016

Abstract

The physical and mechanical properties of polycrystalline materials depend on their microstructure, which is ultimately determined by the shape, orientation and juxtaposition of the grains they are made of. Grains can have sizes over different scales, ranging from Ångstroms to decimeters. In the last two decades, various X-ray techniques emerged to investigate, nondestructively and in 3D, grain shapes and orientations in micrometer- to millimeter-sized polycrystalline samples, with resolution ranging from hundreds of nanometers to micrometers. This paper presents a new technique to study samples with sizes in the centimeters range: time-of-flight three-dimensional neutron diffraction (ToF 3DND). This new method is complementary to the existing X-ray techniques as it enables studies of samples that can be both larger in size and be made up of denser elements as well as facilitating studies involving more complicated sample environments. The setup Tof 3DND, which consists of an imaging detector with high spatial and temporal resolution, can easily be implemented at any time-of-flight neutron beamline. The development of the technique is presented in this paper using data collected at the Japanese spallation neutron source (J-PARC) for an ultrapure, polycrystalline iron sample. We successfully reconstructed the shape of 108 grains, and developed a new indexing procedure based on transmission data: each time a grain satisfied the Bragg condition, missing intensities (extinction spots) were recorded in transmission mode. To uniquely index a grain, it is necessary that the transmission detector also collects diffraction spots. The reconstruction algorithms and results have been validated by comparison with a post mortem electron backscatter diffraction (EBSD) map.

Time-of-Flight Three Dimensional Neutron Diffraction for mapping crystal grain structures ï£¡ II. Transmission and diffraction detectors

Alberto Cereser Markus Strob Stephen Hall
Axel Steuwer Anton Tremsin Ryoji Kiyanagi
Takenao Shinohara Erik Bergbäck Knudsen
Peter Willendrup Alice Bastos da Silva Fanta
Peter Mahler Larsen Srinivasan Iyengar Søren Schmidt

June 1, 2016

Abstract

Time-of-flight three-dimensional neutron diffraction (ToF 3DND) is a new technique to reconstruct shape and orientation of individual grains within polycrystalline samples. ToF 3DND complements existing X-ray techniques: it enables to study centimetre-sized samples and to investigate samples made of heavy elements. The minimal setup of the technique consists of a ToF imaging detector with high spatial and temporal resolution for acquisition of data in transmission mode. In this work we present a new methodology to reconstruct shape and orientation of the grains within a polycrystalline material using both transmission and diffraction detectors. More specifically, data was collected at the single crystal diffractometer SENJU at J-PARC fitted with a ToF imaging detector. The crystallographic orientations of the individual grains was indexed using the GrainSpotter algorithm. This information was then used as a prior to identify the set of extinction spots from which the 3D grain shape of the individual grains could be reconstructed. The combination of both detector systems could potentially improve the detection limit with respect to the size of the individual grains.

Bibliography

[sns,] SNS status. http://status.sns.ornl.gov/beam.jsp. 107

[Amp, 2016] (2016). Amptek Materials Analysis Division. http://amptek.com/. 108

[sta, 2016] (2016). NIST\SEMATECH e-Handbook of Statistical Methods. http://www.itl.nist.gov/div898/handbook/pmc/section3/pmc331.htm. 41

[xno, 2016] (2016). Xnovo Technology ApS. http://xnovotech.com/. 3

[Als-Nielsen and McMorrow, 2011] Als-Nielsen, J. and McMorrow, D. (2011). *Elements of modern X-ray physics*. John Wiley & Sons. 11

[Andersen, 2015] Andersen, K. (2015). New ESS Moderator Baseline. Technical report, The European Spallation Source. 108

[Anderson, 2011] Anderson, K. (2011). Reactor & Spallation Neutron Sources. http://goo.gl/BuAAsa. 18

[Arai, 2009] Arai, M. (2009). J-PARC and the prospective neutron sciences. *Pramana*, 71:629–638. 22, 23

[Arai and Crawford, 2009] Arai, M. and Crawford, K. (2009). Neutron sources and facilities. In Bilheux, H. Z., McGreevy, R., and Anderson, I. S., editors, *Neutron Imaging and Applications*, Neutron Scattering Applications and Techniques, pages 13–30. 17, 18

[Arai and Maekawa, 2014] Arai, M. and Maekawa, F. (2014). Japan Spallation Neutron Source (JSNS) of J-PARC. *Nuclear Physics News*, 19(4):34–39. 22

[Ashcroft and Mermin, 1976] Ashcroft, N. W. and Mermin, N. D. (1976). *Solid state physics*, volume 293. 11

[Atomic Archive, National Science Digital Library, 2015] Atomic Archive, National Science Digital Library (2015). Nuclear Fission: Basics. http://www.atomicarchive.com/Fission/Fission1.shtml. 18

[Attfield et al., 2016] Attfield, M., Barnes, P., Cockcroft, J. K., and Driessen, H. (2016). Internet Course on Powder Diffraction. http://pd.chem.ucl.ac.uk/pdnn/diff2/thermal.htm. 14

[Avinash and Slaney, 1988] Avinash, C. K. and Slaney, M. (1988). *Principles of computerized tomographic imaging*. IEEE press. 101

[Baltser, 2013] Baltser, J. (2013). *Experiments versus simulations: modelling of instrumentation for X-ray scattering experiments*. PhD thesis, Nanoscience Center, Niels Bohr Institute, University of Copenhagen. 39, 40

[Bennett, 2008] Bennett, J. W. (2008). Commissioning of NAA at the new OPAL reactor in Australia. *Journal of Radioanalytical and Nuclear Chemistry*, 278(3):671–673. 17

[Bergbäck Knudsen et al., 2013] Bergbäck Knudsen, E., Prodi, A., Baltser, J., Thomsen, M., Kjær Willendrup, P., Sanchez del Rio, M., Ferrero, C., Farhi, E., Haldrup, K., Vickery, A., Feidenhans'l, R., Mortensen, K., Meedom Nielsen, M., Friis Poulsen, H., Schmidt, S., and Lefmann, K. (2013). McXtrace: a Monte Carlo software package for simulating X-ray optics, beamlines and experiments. *Journal of Applied Crystallography*, 46(3):679–696. 39

[Boden, 2006] Boden, M. A. (2006). *Mind as machine: A history of cognitive science*. Clarendon Press. 54

[Buras and Gerward, 1975] Buras, B. and Gerward, L. (1975). Relations between integrated intensities in crystal diffraction methods for x-rays and neutrons. *Acta Crystallographica Section A: Crystal Physics, Diffraction, Theoretical and General Crystallography*, 31(3):372–374. 14

[Carlile, 2006] Carlile, C. J. (2006). ILL in the changing international context. *Physica B Condensed Matter*, 385:961–965. 17

[Carpenter, 2015] Carpenter, J. M. (2015). Neutron Production & Moderation and the Characterisation of Sources. http://www.neutron.anl.gov/NeutronProduction.pdf. 23

[Center, 2015] Center, J.-P. (2015). Materials and Life Science Experimental Facility - Technical Details. http://j-parc.jp/researcher/MatLife/en/instrumentation/ns3.html. 10

[Cereser and Willendrup, 2014] Cereser, A. and Willendrup, P. (2014). How to make a new .lau file for use with single_crystal.comp, powdern or isotropic_sqw. http://www.mcstas.org/download/share/Instructions_new_lau_file.pdf/. 110

[Chen et al., 2006] Chen, D. F., Liu, Y. T., Gou, C., and Ye, C. T. (2006). Development of neutron scattering on 60 MW research reactor in CIAE. *Physica B Condensed Matter*, 385:966–967. 17

[Clemens et al., 2008] Clemens, H., Mayer, S., and Staron, P. (2008). Microstructure and Properties of Engineering Materials. *Neutrons and Synchrotron Radiation in Engineering Materials Science: From Fundamentals to Material and Component Characterization*, pages 1–20. 2

[Dürer, 1977] Dürer, A. (1977). *Painter's manual (1525)*. Alabaris Books. 2, 38

[Eckhart, 187] Eckhart, R. (187). Stan ulam, john von neumann, and the monte cralo method. *Los Alamos Science*, Special Issue:131–137. 38

[Fischer, 1997] Fischer, W. E. (1997). SINQ - the spallation neutron source, a new research facility at PSI. In *American Institute of Physics Conference Series*, volume 392 of *American Institute of Physics Conference Series*, pages 1119–1122. 19

[Fortune, 1992] Fortune, S. (1992). Voronoi diagrams and delaunay triangulations. *Computing in Euclidean geometry*, 1:193–233. 44

[Frank, 1988] Frank, C. (1988). Orientation mapping: 1987 mrs fall meeting von hippel award lecture. *MRS Bulletin*, 13(03):24–31. 15

[Freeman and Adelson, 1991] Freeman, W. T. and Adelson, E. H. (1991). The design and use of steerable filters. *IEEE Transactions on Pattern Analysis & Machine Intelligence*, (9):891–906. 56

[Fu et al., 2011] Fu, S., Chen, H., Chen, Y., Chi, Y. L., Dong, H., Dong, L., Fang, S., Huang, K., Kang, W., Li, J., Ma, L., Ouyang, H., Qu, H., Sun, H., Tang, J., Wang, C., Wang, Q., Wang, S., Xu, T., Xu, Z., Yin, X., Zhang, C., and Zhang, J. (2011). Status and Challenges of the China Spallation Neutron Source. In *IPAC 2011*, pages 889–893, San Sebastian, Spain. 19

[Gabriel et al., 2003] Gabriel, T. A., Haines, J. R., and McManamy, T. J. (2003). Overview of the Spallation Neutron Source (SNS) with emphasis on target systems. *Journal of Nuclear Materials*, 318:1–13. 18

[Giacovazzo et al., 1998] Giacovazzo, C., Monaco, H. L., Viterbo, D., Scordari, F., GIlli, G., Zanotti, G., and Catti, M. (1998). Iucr texts on crystallography. In Giacovazzo, C., editor, *Fundamentals of Crystallography*. Oxford Science Publications. 8

[Gillies, D. F., 2016] Gillies, D. F. (2016). Interactive Computer Grapics course notes. https://www.doc.ic.ac.uk/~dfg/graphics/graphics2010/GraphicsSlides11.pdf. [Accessed 16-February-2016]. 39

[Google X,] Google X. Google Self-Driving Car Project. https://www.google.com/selfdrivingcar/. 54

[Gordon et al., 1970] Gordon, R., Bender, R., and Herman, G. T. (1970). Algebraic reconstruction techniques (art) for three-dimensional electron microscopy and x-ray photography. *Journal of theoretical Biology*, 29(3):471–481. 101, 106

[Haidekker, 2011] Haidekker, M. (2011). *Advanced biomedical image analysis*. John Wiley & Sons. 64, 65

[Hall and Wright, 2015] Hall, S. A. and Wright, J. (2015). Three-dimensional experimental granular mechanics. *Géotechnique Letters*, 5(4):236–242. 104

[Halton, 1970] Halton, J. H. (1970). A retrospective and prospective survey of the monte carlo method. *Siam review*, 12(1):1–63. 38

[He and Jonas, 2007] He, Y. and Jonas, J. J. (2007). Representation of orientation relationships in rodrigues–frank space for any two classes of lattice. *Journal of Applied Crystallography*, 40(3):559–569. 80, 81

[Herbig et al., 2011] Herbig, M., King, A., Reischig, P., Proudhon, H., Lauridsen, E. M., Marrow, J., Buffière, J.-Y., and Ludwig, W. (2011). 3-d growth of a short fatigue crack within a polycrystalline microstructure studied using combined diffraction and phase-contrast x-ray tomography. *Acta Materialia*, 59(2):590–601. 104

[Herwif, 2009] Herwif, K. W. (2009). Introduction to the neutron. In Bilheux, H. Z., McGreevy, R., and Anderson, I. S., editors, *Neutron Imaging and Applications*, Neutron Scattering Applications and Techniques, pages 3–11. Springer. 8

[Holtkamp et al., 2007] Holtkamp, N. et al. (2007). An overview of the ITER project. *Fusion Engineering and Design*, 82(5):427–434. 104

[Hough, 1959] Hough, P. V. C. (1959). Machine analysis of bubble chamber pictures. In *International Conference on High Energy Accelerators and Instrumentation*, volume 73. 65

[Hough, 1962] Hough, P. V. C. (1962). Method and means for recognizing complex patterns. US Patent 3,069,654. 64, 83

[Ikeda, 2009] Ikeda, Y. (2009). J-PARC status update. *Nuclear Instruments and Methods in Physics Research A*, 600:1–4. 19, 107

[International Union of Crystallography, 2016] International Union of Crystallography (2016). Online Dictionary of Crystallography. http://reference.iucr.org/dictionary/Main_Page. 10

[J-PARC Center, 2015a] J-PARC Center (2015a). BL18 beamline specifications. http://j-parc.jp/researcher/MatLife/en/instrumentation/ns_spec.html#bl18. 25

[J-PARC Center, 2015b] J-PARC Center (2015b). Facilities at J-PARC. http://j-parc.jp/documents/pamphlet/J-PARC_E2011.pdf. 21, 22

[Jackson, A. J., 2008] Jackson, A. J. (2008). Introduction to Small-Angle Neutron Scattering and Neutron Reflectometry. https://www.ncnr.nist.gov/summerschool/ss08/pdf/SANS_NR_Intro.pdf. 8

[Jarosz, 2008] Jarosz, W. (2008). *Efficient Monte Carlo methods for light transport in scattering media*. ProQuest. 39

[Kalos and Whitlock, 2008] Kalos, M. H. and Whitlock, P. A. (2008). *Monte Carlo methods*. John Wiley & Sons. 37

[Kardjilov et al., 2011] Kardjilov, N., Manke, I., Hilger, A., Strobl, M., and Banhart, J. (2011). Neutron imaging in materials science. *Materials Today*, 14(6):248–256. 5

[Kardjilov et al., 2008] Kardjilov, N., Manke, I., Strobl, M., Hilger, A., Treimer, W., Meissner, M., Krist, T., and Banhart, J. (2008). Three-dimensional imaging of magnetic fields with polarized neutrons. *Nature Physics*, 4(5):399–403. 104

[Kass et al., 1988] Kass, M., Witkin, A., and Terzopoulos, D. (1988). Snakes: Active contour models. *International Journal of Computer Vision*, 1(4):321–331. 53

[Kawasaki et al., 2014] Kawasaki, T., Nakamura, T., Toh, K., Hosoya, T., Oikawa, K., Ohhara, T., Kiyanagi, R., Ebine, M., Birumachi, A., Sakasai, K., Soyama, K., and Katagiri, M. (2014). Detector system of the SENJU single-crystal time-of-flight neutron diffractometer at J-PARC-MLF. *Nuclear Instruments and Methods in Physics Research A*, 735:444–451. 23, 24, 26, 27

[Keen et al., 2006] Keen, D. A., Gutmann, M. J., and Wilson, C. C. (2006). SXD - the single-crystal diffractometer at the ISIS spallation neutron source. *Journal of Applied Crystallography*, 39(5):714–722. 23, 24

[Khripunov et al., 2015] Khripunov, B. I., Koidan, V. S., Ryazanov, A. I., Gureev, V. M., Kornienko, S. N., Latushkin, S. T., Rupyshev, A. S., Semenov, E. V., Kulikauskas, V. S., and Zatekin, V. V. (2015). Study of Tungsten as a Plasma-facing Material for a Fusion Reactor. *Physics Procedia*, 71:63–67. 104

[King et al., 2013] King, A., Reischig, P., Adrien, J., and Ludwig, W. (2013). First laboratory x-ray diffraction contrast tomography for grain mapping of polycrystals. *Journal of applied crystallography*, 46(6):1734–1740. 103

[Kittel, 2005] Kittel, C. (2005). *Introduction to solid state physics*. Wiley. 14

[Kiyanagi, 2015] Kiyanagi, R. (2015). Personal communication. 25, 31

[Lauridsen, 2001] Lauridsen, E. M. (2001). *The 3D X-ray diffraction microscope and its application to the study of recrystallization kinetics*. PhD thesis, Technical University of Denmark, Department of Energy Conversion and Storage. 15

[Lefmann, 2014] Lefmann, K. (2014). Neutron Scattering: Theory, Instrumentation, and Simulation. 21, 38

[Lefmann and Nielsen, 1999] Lefmann, K. and Nielsen, K. (1999). Mcstas, a general software package for neutron ray-tracing simulations. *Neutron News*, 10(3):20–23. 2, 37, 39

[Lefmann et al., 2008] Lefmann, K., Willendrup, P. K., Udby, L., Lebech, B., Mortensen, K., Birk, J. O., KlenØ, K., Knudsen, E., Christiansen, P., Saroun, J., et al. (2008). Virtual experiments: the ultimate aim of neutron ray-tracing simulations. *Journal of Neutron Research*, 16(3-4):97–111. 40

[Lim et al., 2009] Lim, I.-C., Kim, Y.-k., Lee, K.-h., and Ha, J.-j. (2009). Current Status of HANARO and Future Plan 2 . Major Facility Upgrades and Ageing Management. In *12th IGORR*, pages 1–9, Beijing, China. 17

[Lindroos et al., 2011] Lindroos, M., Bousson, S., Calaga, R., Danared, H., Devanz, G., Duperrier, R., Eguia, J., Eshraqi, M., Gammino, S., Hahn, H., Jansson, A., Oyon, C., Pape-Møller, S., Peggs, S., Ponton, A., Rathsman, K., Ruber, R., Satogata, T., and Trahern, G. (2011). The European Spallation Source. *Nuclear Instruments and Methods in Physics Research B*, 269:3258–3260. 20

[Liu et al., 2012] Liu, D., Soran, B., Petrie, G., and Shapiro, L. (2012). A review of computer vision segmentation algorithms. *Lecture notes*. 53

[Liu et al., 2011] Liu, H. H., Schmidt, S., Poulsen, H. F., Godfrey, A., Liu, Z. Q., Sharon, J. A., and Huang, X. (2011). Three-dimensional orientation mapping in the transmission electron microscope. *Science*, 332(6031):833–834. 3

[Ludwig et al., 2009] Ludwig, W., Reischig, P., King, A., Herbig, M., Lauridsen, E. M., Johnson, G., Marrow, T. J., and Buffiere, J.-Y. (2009). Three-dimensional grain mapping by x-ray diffraction contrast tomography and the use of friedel pairs in diffraction data analysis. *Review of Scientific Instruments*, 80(3):033905. 92, 103

[Ludwig et al., 2008] Ludwig, W., Schmidt, S., Lauridsen, E. M., and Poulsen, H. F. (2008). X-ray diffraction contrast tomography: a novel technique for three-dimensional grain mapping of polycrystals. i. direct beam case. *Journal of Applied Crystallography*, 41(2):302–309. 3, 4, 33, 92

[Maitland and Sitzman, 2007] Maitland, T. and Sitzman, S. (2007). *Electron backscatter diffraction (EBSD) technique and materials characterization examples*, volume 14. Springer Berlin. 95

[Mason et al., 2006] Mason, T. E., Abernathy, D., Anderson, I., Ankner, J., Egami, T., Ehlers, G., Ekkebus, A., Granroth, G., Hagen, M., Herwig, K., Hodges, J., Hoffmann, C., Horak, C., Horton, L., Klose, F., Larese, J., Mesecar, A., Myles, D., Neuefeind, J., Ohl, M., Tulk, C., Wang, X.-L., and Zhao, J. (2006). The Spallation Neutron Source in Oak Ridge: A powerful tool for materials research. *Physica B Condensed Matter*, 385:955–960. 18

[MATLAB®,] MATLAB®. The `bwlabel` function. http://it.mathworks.com/help/images/ref/bwlabel.html. 57, 58, 72

[MATLAB®, 2015] MATLAB® (2015). *version 8.6 (R2015b)*. The MathWorks Inc., Natick, Massachusetts. 57, 58, 72

[McStas website, 2016] McStas website (2016). Components and Instruments from the Library for McStas. http://www.mcstas.org/download/components/. 39

[Merkel et al., 2010] Merkel, S., Nisr, C., Ribarik, G., Ungár, T., Vaughan, G., and Cordier, P. (2010). A new method for the experimental study of dislocations in high pressure minerals. In *AGU Fall Meeting Abstracts*, volume 1, page 1862. 104

[Mohanlal, 1979] Mohanlal, S. K. (1979). An experimental determination of the debye-waller factor for iron by neutron diffraction. *Journal of Physics C: Solid State Physics*, 12(17):L651. 15

[Morawiec and Field, 1996] Morawiec, A. and Field, D. P. (1996). Rodrigues parameterization for orientation and misorientation distributions. *Philosophical Magazine A*, 73(4):1113–1130. 15, 81

[Motojima, 2015] Motojima, O. (2015). The ITER project construction status. *Nuclear Fusion*, 55(10):104023. 104

[Nagamiya, 2009] Nagamiya, S. (2009). Overview of J-PARC. In Sato, T., Takahashi, T., and Yoshimura, K., editors, *Particle and Nuclear Physics at J-PARC*, volume 781 of *Lecture Notes in Physics, Berlin Springer Verlag*, page 1. 22

[Nagamiya, 2012] Nagamiya, S. (2012). Introduction to J-PARC. *Progress of Theoretical and Experimental Physics*, 2012:2B001–0. 18, 21

[Neuhaus and Petry, 2007] Neuhaus, J. and Petry, W. (2007). Correspondent's Report: Forschungsneutronenquelle Heinz Maier-Leibnitz (FRM II). *Neutron News*, 18(2):13–15. 17

[Neutron Source Section, Materials and Life Science Division, 2011] Neutron Source Section, Materials and Life Science Division (2011). Technical Design Report of Spallation Neutron Source Facility in J-PARC. 22

[NVIDIA, 2016] NVIDIA (2016). NVIDIA® OptiX™ Ray Tracing Engine. https://developer.nvidia.com/optix. [Accessed 15-February-2016]. 39

[Ohhara et al., 2009] Ohhara, T., Kusaka, K., Hosoya, T., Kurihara, K., Tomoyori, K., Niimura, N., Tanaka, I., Suzuki, J., Nakatani, T., Otomo, T., Matsuoka, S., Tomita, K., Nishimaki, Y., Ajima, T., and Ryufuku, S. (2009). Development of data processing software for a new TOF single crystal neutron diffractometer at J-PARC. *Nuclear Instruments and Methods in Physics Research A*, 600:195–197. 28, 92, 110

[Oikawa et al., 2014] Oikawa, K., Kawasaki, T., Ohhara, T., Kiyanagi, R., Kaneko, K., Tamura, I., Nakamura, T., Harada, M., Nakao, A., Hanashima, T., Munakata, K., Kimura, H., Noda, Y., Takahashi, M., and Kiyotani, T. (2014). Instrument Design and Performance Evaluation of a New Single Crystal Neutron Diffractometer SENJU at J-PARC. *JPS Conference Proceedings*, 1(1):014013. 24, 25, 26, 27

[Okabe et al., 2009] Okabe, A., Boots, B., Sugihara, K., and Chiu, S. N. (2009). *Spatial tessellations: concepts and applications of Voronoi diagrams*, volume 501. John Wiley & Sons. 44, 110

[Peetermans et al., 2013] Peetermans, S., Grazzi, F., Salvemini, F., Lehmann, E. H., Caporali, S., and Pratesi, G. (2013). Energy-selective neutron imaging for morphological and phase analysis of iron–nickel meteorites. *Analyst*, 138(18):5303–5308. 104

[Peetermans et al., 2014] Peetermans, S., King, A., Ludwig, W., Reischig, P., and Lehmann, E. H. (2014). Cold neutron diffraction contrast tomography of polycrystalline material. *Analyst*, 139(22):5766–5772. 3, 31, 103, 107

[Peggs et al., 2013] Peggs, S., Kreier, R., Carlile, C., Miyamoto, R., Pahlsson, A., Trojer, M., and Weisend II, J. G. (2013). ESS technical design report. *ESS-doc-274*. 107, 108

[Peters et al., 2005] Peters, J., Muthuswamy, M., Wibowo, J., and Tordesillas, A. (2005). Characterization of force chains in granular material. *Physical Review E*, 72(4):041307. 104

[Poulsen, 2004] Poulsen, H. F. (2004). *Three-dimensional X-ray diffraction microscopy: mapping polycrystals and their dynamics*, volume 205. Springer Science & Business Media. 2

[Poulsen, 2012] Poulsen, H. F. (2012). An introduction to three-dimensional x-ray diffraction microscopy. *Journal of Applied Crystallography*, 45(6):1084–1097. 106

[Poulsen, 2016] Poulsen, H. F. (2016). Personal communication. 108

[Poulsen et al., 2001] Poulsen, H. F., Nielsen, S. F., Lauridsen, E. M., Schmidt, S., Suter, R. M., Lienert, U., Margulies, L., Lorentzen, T., and Juul Jensen, D. (2001). Three-dimensional maps of grain boundaries and the stress state of individual grains in polycrystals and powders. *Journal of Applied Crystallography*, 34(6):751–756. 3, 77, 92

[Poulsen et al., 2014] Poulsen, S. O., Poulsen, H. F., and Bentley, P. M. (2014). Refractive and diffractive neutron optics with reduced chromatic aberration. *Nuclear Instruments and Methods in Physics Research Section A: Accelerators, Spectrometers, Detectors and Associated Equipment*, 767:415–420. 108

[Pynn, 2009] Pynn, R. (2009). Neutron Scattering - A Non-destructive Microscope for Seeing Inside Matter. In Liang, L. and Schober, H. R. R., editors, *Neutron Applications in Earth, Energy and Environmental Sciences, Neutron Scattering Applications and Techniques*, page 15. Springer. 8, 10

[Randle and Engler, 2000] Randle, V. and Engler, O. (2000). *Introduction to texture analysis: macrotexture, microtexture and orientation mapping*. CRC press. 2, 15

[Reischig et al., 2013] Reischig, P., King, A., Nervo, L., Vigano, N., Guilhem, Y., Palenstijn, W. J., Batenburg, K. J., Preuss, M., and Ludwig, W. (2013). Advances in x-ray diffraction contrast tomography: flexibility in the setup geometry and application to multiphase materials. *Journal of Applied Crystallography*, 46(2):297–311. 103

[Rudin et al., 1992] Rudin, L. I., Osher, S., and Fatemi, E. (1992). Nonlinear total variation based noise removal algorithms. *Physica D: Nonlinear Phenomena*, 60(1):259–268. 101

[Rudin, 1964] Rudin, W. (1964). *Principles of mathematical analysis*, volume 3. McGraw-Hill New York. 95

[Rupp, 2009] Rupp, B. (2009). *Biomolecular crystallography: principles, practice, and application to structural biology*. Garland Science. 92

[Russ, 2015] Russ, J. C. (2015). *The image processing handbook*. CRC press. 59

[Rycroft, 2009] Rycroft, C. (2009). Voro++: A three-dimensional Voronoi cell library in C++. *Lawrence Berkeley National Laboratory*. 44, 110

[Sakurai et al., 2002] Sakurai, F., Horiguchi, Y., Kobayashi, S., and Takayanagi, M. (2002). Present status and future prospect of JRR-3 and JRR-4. *Physica B Condensed Matter*, 311:7–13. 17

[Salvatore,] Salvatore, J. A Brief Introduction to Voronoi and Delaunay Diagrams. http://www.dyinglovegrape.com/math/voronoi_diagram_1.php. 44

[Schmidt, 2014] Schmidt, S. (2014). GrainSpotter: a fast and robust polycrystalline indexing algorithm. *Journal of Applied Crystallography*, 47(1):276–284. 35, 76, 79, 88, 92, 106

[Schober et al., 2008] Schober, H., Farhi, E., Mezei, F., Allenspach, P., Andersen, K., Bentley, P. M., Christiansen, P., Cubitt, B., Heenan, R. K., Kulda, J., Langan, P., Lefmann, K., Lieutenant, K., Monkenbusch, M., Willendrup, P., Šaroun, J., Tindemans, P., and Zsigmond, G. (2008). Tailored instrumentation for long-pulse neutron spallation sources. *Nuclear Instruments and Methods in Physics Research A*, 589:34–46. 18

[Schwartz et al., 2009] Schwartz, A. J., Kumar, M., Adams, B. L., and Field, D. P. (2009). *Electron backscatter diffraction in materials science*, volume 2. Springer. 71

[Siegrist, 1997] Siegrist, T. (1997). Crystallographica-a software toolkit for crystallography. *Journal of Applied Crystallography*, 30(3):418–419. 110

[Simons et al., 2015] Simons, H., King, A., Ludwig, W., Detlefs, C., Pantleon, W., Schmidt, S., Stöhr, F., Snigireva, I., Snigirev, A., and Poulsen, H. F. (2015). Dark-field x-ray microscopy for multiscale structural characterization. *Nature communications*, 6. 108

[Sonka et al., 2014] Sonka, M., Hlavac, V., and Boyle, R. (2014). *Image processing, analysis, and machine vision*. Cengage Learning. 53, 59

[Spencer and Murty, 1962] Spencer, G. H. and Murty, M. V. R. K. (1962). General ray-tracing procedure. *JOSA*, 52(6):672–676. 39

[Sperling, 2009] Sperling, R. (2009). Particle Size Analyzer (PSA) macro for ImageJ. https://code.google.com/archive/p/psa-macro/. 57

[Strobl, 2016] Strobl, M. (2016). Personal communication. 19, 107

[Strobl et al., 2008] Strobl, M., Grünzweig, C., Hilger, A., Manke, I., Kardjilov, N., David, C., and Pfeiffer, F. (2008). Neutron dark-field tomography. *Physical review letters*, 101(12):123902. 5

[Strobl et al., 2009] Strobl, M., Manke, I., Kardjilov, N., Hilger, A., Dawson, M., and Banhart, J. (2009). Advances in neutron radiography and tomography. *Journal of Physics D: Applied Physics*, 42(24):243001. 5

[Suter et al., 2006] Suter, R. M., Hennessy, D., Xiao, C., and Lienert, U. (2006). Forward modeling method for microstructure reconstruction using x-ray diffraction microscopy: Single-crystal verification. *Review of Scientific Instruments*, 77(12):123905. 3

[Szeliski, 2010] Szeliski, R. (2010). *Computer vision: algorithms and applications*. Springer Science & Business Media. 54

[Tamura et al., 2012] Tamura, I., Oikawa, K., Kawasaki, T., Ohhara, T., Kaneko, K., Kiyanagi, R., Kimura, H., Takahashi, M., Kiyotani, T., Arai, M., Noda, Y., and Ohshima, K. (2012). Current status of a time-of-flight single crystal neutron diffractometer SENJU at J-PARC. *Journal of Physics Conference Series*, 340(1):012040. 24, 25, 28, 43, 109

[Tanaka et al., 2010] Tanaka, I., Kusaka, K., Hosoya, T., Niimura, N., Ohhara, T., Kurihara, K., Yamada, T., Ohnishi, Y., Tomoyori, K., and Yokoyama, T. (2010). Neutron structure analysis using the IBARAKI biological crystal diffractometer (iBIX) at J-PARC. *Acta Crystallographica Section D*, 66(11):1194–1197. 24, 28

[Tatsumoto et al., 2010] Tatsumoto, H., Aso, T., Ohtsu, K., Uehara, T., Sakurayama, H., Kawakami, Y., Kato, T., and Futakawa, M. (2010). Development of the Cryogenic Hydrogen System for a Spallation Neutrton Source in J-Parc. In *American Institute of Physics Conference Series*, volume 1218 of *American Institute of Physics Conference Series*, pages 297–304. 22

[Thomason, 2008] Thomason, J. W. G. (2008). Upgrades to ISIS for the New Second Target Station. In *Proc. Euro. Part. Accel. Conf.(EPAC), Genoa*, pages 2902–2906. 19

[Thomopoulos, 2012] Thomopoulos, N. T. (2012). *Essentials of Monte Carlo simulation: Statistical methods for building simulation models*. Springer Science & Business Media. 37

[Thompson Reuters,] Thompson Reuters. Web of Science website. http://wokinfo.com/. 54

[Tremsin, 2016] Tremsin, A. (2016). Personal communication. 106, 107

[Tremsin et al., 2005] Tremsin, A. S., Feller, W. B., and Downing, R. G. (2005). Efficiency optimization of microchannel plate (MCP) neutron imaging detectors. I. Square channels with ^{10}B doping. *Nuclear Instruments and Methods in Physics Research Section A: Accelerators, Spectrometers, Detectors and Associated Equipment*, 539(1):278–311. 29, 30

[Tremsin et al., 2012] Tremsin, A. S., McPhate, J. B., Steuwer, A., Kockelmann, W., Paradowska, A. M., Kelleher, J. F., Vallerga, J. V., Siegmund, O. H. W., and Feller,

W. B. (2012). High-Resolution Strain Mapping Through Time-of-Flight Neutron Transmission Diffraction with a Microchannel Plate Neutron Counting Detector. *Strain*, 48:296–305. 29

[Tremsin et al., 2014] Tremsin, A. S., Vallerga, J. V., McPhate, J. B., and Siegmund, O. H. W. (2014). Optimization of Timepix count rate capabilities for the applications with a periodic input signal. *Journal of Instrumentation*, 9(05):C05026. 49, 50, 52

[Tremsin et al., 2013] Tremsin, A. S., Vallerga, J. V., McPhate, J. B., Siegmund, O. H. W., and Raffanti, R. (2013). High Resolution Photon Counting With MCP-Timepix Quad Parallel Readout Operating at Frame Rates. *Nuclear Science, IEEE Transactions on*, 60(2):578–585. 29, 30, 50

[Turecek et al., 2011] Turecek, D., Holy, T., Jakubek, J., Pospisil, S., and Vykydal, Z. (2011). Pixelman: a multi-platform data acquisition and processing software package for Medipix2, Timepix and Medipix3 detectors. *Journal of Instrumentation*, 6(01):C01046. 107

[Uchida, 2012] Uchida, T. (2012). SiTCP Manual. http://research.kek.jp/people/uchida/technologies/SiTCP/doc/SiTCP_eng.pdf. 28

[Varón, 2016] Varón, M. (2016). Personal communication. 57

[Vickery et al., 2014] Vickery, A., Willendrup, P. K., and Knudsen, E. (2014). A note about McStas errorbars. 40, 41

[Voigt, 2012] Voigt, J. (2012). Neutron sources. In Brückel, T., Heger, G., Richter, D., Roth, G., and Zorn, R., editors, *Lectures of the JCNS Laboratory Course held at Forschungszentrum Jülich and the research reactor FRM II of TU Munich*. Forschungszentrum Jülich GmbH. 8, 17, 18, 20

[Vollmer et al., 2015] Vollmer, M., Krooß, P., Segel, C., Weidner, A., Paulsen, A., Frenzel, J., Schaper, M., Eggeler, G., Maier, H. J., and Niendorf, T. (2015). Damage evolution in pseudoelastic polycrystalline co–ni–ga high-temperature shape memory alloys. *Journal of Alloys and Compounds*, 633:288–295. 74

[Von Dreele, 1990] Von Dreele, R. B. (1990). X-ray and neutron crystallography. a powerful combination. *Los Alamos Science*, (19). 8

[Wagner et al., 2006] Wagner, W., Mesot, J., Allenspach, P., Kuehne, G., and Rønnow, H. M. (2006). The Swiss spallation neutron source SINQ - developments and upgrades for optimized user service. *Physica B Condensed Matter*, 385:968–971. 19

[Warhol, 1962] Warhol, A. (1962). Marilyn diptych. 12

[Wensrich et al., 2014] Wensrich, C. M., Kisi, E. H., Luzin, V., Garbe, U., Kirstein, O., Smith, A. L., and Zhang, J. F. (2014). Force chains in monodisperse spherical particle assemblies: Three-dimensional measurements using neutrons. *Physical Review E*, 90(4):042203. 105

[Wikipedia, 2016] Wikipedia (2016). Monte Carlo method. https://en.wikipedia.org/wiki/Monte_Carlo_method. [Accessed 09-February-2016]. 38

[Wilkinson and Britton, 2012] Wilkinson, A. J. and Britton, T. B. (2012). Strains, planes, and ebsd in materials science. *Materials Today*, 15(9):366–376. 95

[Willendrup et al., 2014a] Willendrup, P., Fahri, E., Knudsen, E., Filges, U., Lefmann, K., and Stein, J. (2014a). User and programmers guide to the neutron ray-tracing package mcstas, version 2.1. http://www.mcstas.org/documentation/manual/mcstas-2.2a-manual.pdf. 40, 41, 43, 45, 110

[Willendrup et al., 2014b] Willendrup, P., Farhi, E., Knudsen, E. B., Filges, U., and Lefmann, K. (2014b). Mcstas: Past, present and future. *Journal of Neutron Research*, 17(1):35–43. 37, 109

[Willis and Carlile, 2009] Willis, B. T. W. and Carlile, C. J. (2009). *Experimental Neutron Scattering*. Oxford University Press. 11, 20, 21

[Wilson, 1995] Wilson, C. C. (1995). A guided tour of ISIS - the UK spallation neutron source. *Neutron News*, 2:27–34. 18

[Woracek et al., 2015] Woracek, R., Penumadu, D., Kardjilov, N., Hilger, A., Boin, M., Banhart, J., and Manke, I. (2015). Neutron Bragg Edge Tomography for Phase Mapping. *Physics Procedia*, 69:227–236. 5, 104

[Zaefferer et al., 2008] Zaefferer, S., Wright, S. I., and Raabe, D. (2008). Three-dimensional orientation microscopy in a focused ion beam - scanning electron microscope: A new dimension of microstructure characterization. *Metallurgical and Materials Transactions A*, 39(2):374–389. 3

[Zhong et al., 2006] Zhong, L., Hu, J., Liang, H., Cao, A., Song, W., and Wan, L. (2006). Self-assembled 3d flowerlike iron oxide nanostructures and their application in water treatment. *Advanced Materials*, 18(18):2426–2431. 57